A NEURAL NETWORK BASED WAKE MODEL FOR SMALL WIND TURBINE SITING NEAR OBSTACLES

A Thesis

Presented to

The Faculty of Graduate Studies

of

The University of Guelph

by

ANDREW WILLIAM BRUNSKILL

In partial fulfilment of requirements

for the degree of

Master of Applied Science

March, 2010

© Andrew Brunskill, 2010



Library and Archives Canada

Published Heritage Branch

395 Wellington Street Ottawa ON K1A 0N4 Canada Bibliothèque et Archives Canada

Direction du Patrimoine de l'édition

395, rue Wellington Ottawa ON K1A 0N4 Canada

> Your file Votre référence ISBN: 978-0-494-67483-3 Our file Notre référence ISBN: 978-0-494-67483-3

NOTICE:

The author has granted a non-exclusive license allowing Library and Archives Canada to reproduce, publish, archive, preserve, conserve, communicate to the public by telecommunication or on the Internet, loan, distribute and sell theses worldwide, for commercial or non-commercial purposes, in microform, paper, electronic and/or any other formats.

The author retains copyright ownership and moral rights in this thesis. Neither the thesis nor substantial extracts from it may be printed or otherwise reproduced without the author's permission.

AVIS:

L'auteur a accordé une licence non exclusive permettant à la Bibliothèque et Archives Canada de reproduire, publier, archiver, sauvegarder, conserver, transmettre au public par télécommunication ou par l'Internet, prêter, distribuer et vendre des thèses partout dans le monde, à des fins commerciales ou autres, sur support microforme, papier, électronique et/ou autres formats.

L'auteur conserve la propriété du droit d'auteur et des droits moraux qui protège cette thèse. Ni la thèse ni des extraits substantiels de celle-ci ne doivent être imprimés ou autrement reproduits sans son autorisation.

In compliance with the Canadian Privacy Act some supporting forms may have been removed from this thesis.

While these forms may be included in the document page count, their removal does not represent any loss of content from the thesis.

Conformément à la loi canadienne sur la protection de la vie privée, quelques formulaires secondaires ont été enlevés de cette thèse.

Bien que ces formulaires aient inclus dans la pagination, il n'y aura aucun contenu manquant.



ABSTRACT

A NEURAL NETWORK-BASED WAKE MODEL FOR SMALL WIND TURBINE

SITING NEAR OBSTACLES

Andrew William Brunskill University of Guelph, 2010

Advisor: Dr. David Lubitz

Many potential small wind turbine locations are near obstacles such as buildings and shelterbelts, which can have a significant, detrimental effect on the local wind climate. This thesis describes the creation of a new model which can predict the wind speed, turbulence intensity, and wind power density at any point in an obstacle's region of influence, relative to unsheltered conditions. Artificial neural networks were used to learn the relationship between an obstacle's characteristics and its effects on the local wind. The neural network was trained using measurements collected in the wakes of scale models exposed to a simulated atmospheric boundary layer in a wind tunnel. A field experiment was conducted to validate the wind tunnel measurements. Model predictions are most accurate in the far wake region. The estimated mean uncertainties associated with model predictions of velocity deficit, power density deficit, and turbulence intensity excess are 5.0%, 15%, and 12.8%, respectively.

Acknowledgements

The author would like to thank Dr. David Lubitz for his guidance on this project, as well as Brett Ziter for his assistance with the field work. The Lubitz family is thanked for providing an excellent location at which to conduct the main field experiment.

The financial support received from the Ontario Centres of Excellence – Centre for Energy is gratefully acknowledged.

Weather INnovations Inc. and Wenvor Technologies also deserve thanks for providing the motivation for this project. As well, Weather INnovations is thanked for supplying equipment and the test site during initial field experimentation.

Table of Contents

List of	Tables	S	V
List of	Figure	es	v i
Nomer	nclatur	e	x i
Glossa	ry of T	Terms	xiii
1.0	Introd	luction	1
1.1	Sm	all Wind Turbines	1
1.2	Exi	isting Siting Methods	2
1.3	Res	search Objectives	5
1.4	The	esis Overview	6
2.0	Litera	ture Review	8
2.1	Wi	nd Characteristics Relevant to Small Wind Turbines	8
2.2	Wi	nd above Open Terrain	9
2.3	Eff	ect of an Obstacle on the Wind	11
2.4	Wa	ikes of Bluff Bodies	13
2	.4.1	Two Dimensional Fence	14
2	.4.2	Cube	15
2	.4.3	Prismatic Obstacles	15
2	.4.4	Reynolds Number Dependence	19
2	.4.5	Locations of Maximum Wake Effects	20
2.5	Wa	ikes of Multiple Obstacles	21
2.6	Exi	isting Wake Models	23
2.7	Otl	ner Wake Modeling Approaches Considered	29
2.8	Ne	ural Networks	31
2	Q 1	Operation	31

2.8.2 Applications of Neural Networks to Wind Engineering	32
3.0 Overview of wakeNET Model	35
3.1 Inputs	35
3.2 Outputs	38
3.3 Source of Training Data	40
3.4 Implementation	41
4.0 Wind Tunnel Experimentation	42
4.1 Equipment and Set Up	42
4.2 Simulation of the ABL	46
4.3 Testing Procedure	50
4.4 Summary of Tests Performed	53
4.5 Results	55
4.5.1 Reynolds Number Dependence	55
4.5.2 Comparison to Reference Results	56
4.5.3 Wakes of Very Wide Obstacles	59
4.5.4 Wake Symmetry	64
4.5.5 Far Wake Persistence	64
4.5.6 Comparison to General Guidelines	67
5.0 Field Experiment	72
5.1 Experimental Set Up	72
5.2 Data Analysis Procedure and Considerations	76
5.3 Convergence of Field Data	80
5.4 Wind Tunnel Simulation of the Field Experiment	88
5.5 Comparison of Results	90
5.6 Distribution of Wind Speed	100
6.0 wakeNET model	103

6.	1 Trai	ining Data	103
6.2	2 Cre	ation and Development	108
	6.2.1	Overview of NN Development	.108
	6.2.2	NN Description	.109
	6.2.3	Pre-processing	.111
	6.2.4	Post-Processing	.113
	6.2.5	Learning	.113
6	3 Eva	luation of Accuracy and Generality	.115
6.4	4 Val	idation	.121
	6.4.1	Comparison to Existing Models	.122
	6.4.2	Predictions for New Obstacles in the Wind Tunnel	.127
	6.4.3	Above Obstacle Performance	.129
	6.4.4	Predictions for a New Full Scale Obstacle	.132
6	5 Mu	ltiple Wake Interactions	.134
6.	6 Sou	rces of Error	. 136
6.	7 Mo	del Performance Summary	. 137
7.0	Concl	usions and Recommendations	. 140
Refe	rences		. 144
Appe	endices		.149
A.	Case Stu	ıdy	.149
B.	Calibrat	ion of Hot Film Probes	.161
C.	Develop	oment and Uniformity of Simulated Boundary Layer	. 164
D.	Flow Ur	nsteadiness in the Wind Tunnel	. 167
E.	Reynold	Is Number Dependence of Flow in the Wind Tunnel	. 172
F.	Uncerta	inty Analysis	. 177
G.	Multiple	Wake Interactions	.188

List of Tables

Table 2.1 – Effect of aspect ratio on the start of the development region, based on [19] unless	3
noted	18
Table 4.1 – Summary of obstacles used in the wind tunnel	44
Table 4.2 – Summary of the measurements made to characterize the flow for each obstacle	54
Table 4.3 –Main differences between the current and reference experiments	56
Table 5.1 – Summary of anemometers used in the field experiment	74
Table 5.2 – Summary of obstacle characteristics	76
Table 5.3 – Uncertainties in R_V and R_I by sensor location	80
Table 5.4 – MAD of the wind tunnel compared to field results, for each sensor location	94
Table 5.5 – MAD values for R_V and R_I for the large wall, small wall, and trailer	94
Table 6.1 – Example data points	103
Table 6.2 – Measurements made and NN training points used for each obstacle	104
Table 6.3 – MSE and MAE of the final R_V and R_I NNs	116
Table A.1 – Obstacle characteristics	151
Table A.2 – Case study final results	159
Table B.1 – Summary of hot film probes	161
Table F.1 – Summary of sources of uncertainty for each hot film reading	180
Table F.2 – Uncertainties of quantities used to calculate R_V	181
Table F.3 – Uncertainties of quantities used to calculate R_l	183
Table F.4 – Summary of uncertainties in R_V at each sensor location	186
Table F.5 – Summary of uncertainties in R_l at each sensor location	187
Table G.1 – Details of tests conducted using cluster 1 to generate the wake	192
Table G.2 – Details of tests conducted using cluster 2 to generate the wake	193
Table G.3. MAE and ME of each prediction method	194

List of Figures

Figure 2.1 – Mean streamline patterns about a building, adapted from [20]
Figure 2.2 – Vortex formation on the roof of a rectangular building. Adapted from [20]
Figure 2.3 – Schematic representation of flow regions around multiple structures, from [23]22
Figure 3.1 – Overview of proposed NN-based model
Figure 3.2 – Definition of building roof angle
Figure 4.1 – Diagram of the wind tunnel. Dimensions are in m
Figure 4.2 – Comparison of wind tunnel unsheltered profiles to reference profiles for a rural area.
a) Shows mean velocity profiles, including a power law fit derived from measurements
taken at the field site. b) Shows mean turbulence intensity profiles47
Figure 4.3 – Comparison of unsheltered turbulent power spectra in the wind tunnel to reference
curve [42]49
Figure 4.4 – Vertical R_V profiles in the wake of a two-dimensional wall, at $x = 10$
Figure 4.5 – Vertical R_l profiles in the wake of a two-dimensional wall, at $x = 10$
Figure 4.6 – Vertical R_V profiles in the wake of a cube at $x = 4.53$, $z = 0$, with $a = 0^{\circ}$
Figure 4.7 – Vertical R_V profiles in the wake of a cube at $x = 6.84$, $z = 0$, with $a = 45^{\circ}$ 60
Figure 4.8 – Lateral R_V profiles in the wake of the 9-1 block at $x = 7.17$, $y = 0.94$, $a = 0^{\circ}$ 61
Figure 4.9 – The wake of a very wide obstacle, divided into regions when the flow is dependent
on z, and where the flow is independent of z. y is constant62
Figure 4.10 – Lateral R_V profile in the wake of the 9-1 block, the 4-1 block, and the 5-1-36 block,
at $x = 7.17$, $y = 0.94$, $a = 0^{\circ}$
Figure $4.11 - R_V$ profiles in the far wakes of the 4-1 and 9-1 blocks, at $z = 0$, $a = 0^{\circ}$ 66
Figure 4.12 – Far wake R_V profiles of the 4-1 and 9-1 blocks, at $z = -4.95$ and -5.2,
magnestively, a = 450

Figure 4.13 – R_P profiles in the far wakes of the cube, at $x = 15.7$, $z = -3.29$; the 2-1 block, at $x = 15.7$, $z = -3.29$; the 2-1 block, at $x = 15.7$, $z = -3.29$; the 2-1 block, at $x = 15.7$, $z = -3.29$; the 2-1 block, at $x = 15.7$, $z = -3.29$; the 2-1 block, at $x = 15.7$, $z = -3.29$; the 2-1 block, at $x = 15.7$, $z = -3.29$; the 2-1 block, at $x = 15.7$, $z = -3.29$; the 2-1 block, at $x = 15.7$, $z = -3.29$; the 2-1 block, at $x = 15.7$, $z = -3.29$; the 2-1 block, at $x = 15.7$, $z = -3.29$; the 2-1 block, at $x = 15.7$, $z = -3.29$; the 2-1 block, at $x = 15.7$, $z = -3.29$; the 2-1 block, at $x = 15.7$, $z = -3.29$; the 2-1 block, at $x = 15.7$, $z = -3.29$; the 2-1 block, at $x = 15.7$, $z = -3.29$; the 2-1 block, at $z = 15.7$, $z = -3.29$; the $z = 15.7$, $z = 15$	
20 z = -2.73; the 4-1 block, at $x = 19$, $z = -4.95$; and the 9-1 block, at $x = 20$, $z = -5.2$. For	
all four obstacles, $a = 45^{\circ}$	59
Figure 4.14 – R_I profiles in the far wakes of the cube, at $x = 15.7$, $z = -3.29$; the 2-1 block, at $x = 15.7$	
20, $z = -2.73$; the 4-1 block, at $x = 19$, $z = -4.95$; and the 9-1 block, at $x = 20$, $z = -5.2$. For	
all four obstacles, $a = 45^{\circ}$.	70
Figure 5.1 – Layout of field experiment, with the trailer as the obstacle	72
Figure 5.2 – Photograph of the field site	73
Figure 5.3 – Distances to nearby obstacles at the field site (photo: Grand River Conservation	
Authority)	15
Figure 5.4 – Comparison of upwind turbulent power spectra in the field to the reference curve	
[42]	7
Figure 5.5 – Maximum precision limit of mean R_{ν} considering all sensors.	32
Figure 5.6 – Maximum precision limit of mean R_l considering all sensors	3
Figure 5.7 – Convergence of R_V as more data samples are included in the calculation, for sensor	4
Obstacle is the large wall, with the wind direction bin centered at 275°	}4
Figure 5.8 – Convergence for each wind sector, with the large wall obstacle	\$5
Figure 5.9 – Convergence for each wind sector, with the small wall obstacle	36
Figure 5.10 – Convergence for each wind sector, with the trailer obstacle	;7
Figure 5.11 – Variation of R_i and R_i at an emometer 2, in the wake of the large wall) [
Figure 5.12 – Variation of R_i and R_l at an emometer 3, in the wake of the large wall)2
Figure 5.13 – Variation of R_V and R_I at an emometer 2, in the wake of the small wall)5
Figure 5.14 – Variation of R_V and R_I at an emometer 4, in the wake of the small wall)5
Figure 5.15 – Variation of R_V and R_I at an emometer 2, in the wake of the trailer)6
Figure 5.16 – Variation of R_V and R_I at an emometer 3, in the wake of the trailer)6
Figure 5.17 – Variation of R. and R. at an emometer 4. in the wake of the trailer)7

Figure 5.18 – Variation of R_V and R_I at an emometer 6, in the wake of the trailer97
Figure 5.19 - PDFs and Weibull fits of unsheltered data, sheltered data, and predicted data101
Figure 6.1 – Use of symmetry to create training data
Figure 6.2 – Use of duplication to generate NN training points
Figure 6.3 – Example MSE of four data sets during a training session, and their variances 114
Figure 6.4 – Comparison of sample model predictions, training data, and validation data, with
varying x. Other parameters are held constant at $y = 3.2$, $z = 0$, $a = 0^{\circ}$, $AR = 9$, $PR = 1$, $RA = 0^{\circ}$
0117
Figure 6.5 - Comparison of sample model predictions, training data, and validation data, with
varying y. Other parameters are held constant at $x = 5$, $z = 1.42$, $a = -22.5^{\circ}$, $AR = 2$, $PR = 1$,
RA = 0.
Figure 6.6 - Comparison of sample model predictions, training data, and validation data, with
varying z. Other parameters are held constant at $x = 10$, $y = 2$, $a = 22.5^{\circ}$, $AR = 4$, $PR = 1$, RA
= 0
Figure 6.7 - Comparison of sample model predictions, training data, and validation data, with
varying a. Other parameters are held constant at $x = 10$, $y = 1.8$, $z = -1.94$, $AR = 2$, $PR = 1$,
RA = 0.
Figure 6.8 - Comparison of sample model predictions, training data, and validation data, with
varying AR. Other parameters are held constant at $x = 5$, $y = 1$, $z = 0$, $a = 0$, $PR = 1$, $RA = 0$.
119
Figure 6.9 - Comparison of sample model predictions, training data, and validation data, with
varying PR. Other parameters are held constant at $x = 10$, $y = 1.4$, $z = 0$, $a = 0$, $AR = 1$, $RA = 1$
0
Figure 6.10 - Comparison of sample model predictions, training data, and validation data, with
varying RA. Other parameters are held constant at $x = 15.75$, $y = 1.4$, $z = -2.20$, $a = 45$, AR
= 2 PR = 1 120

Figure 6.11 – Lateral R_V profiles in the wake of Hansen's block, at $x = 7.55$, $y = 0.94$, $a = 0^\circ$.	122
Figure 6.12 – Lateral R_I profiles in the wake of Hansen's block at $x = 7.55$, $y = 0.94$, $a = 0^{\circ}$.	123
Figure 6.13 – Lateral R_V profiles in the wake of Hansen's block at $x = 7.55$, $y = 0.94$, $a = 47^\circ$	125
Figure 6.14 – Lateral R_l profiles in the wake of Hansen's block at $x = 7.55$, $y = 0.94$, $a = 47^{\circ}$.	.125
Figure 6.15 – Variation of R_V with height at $x = 12$, $z = 3$, $a = -40$ in the wakes of three obstacles.	cles
used purely for validation	128
Figure 6.16 – Variation of R_i with height at $x = 12$, $z = 3$, $a = -40$ in the wakes of three obstacts	eles
used purely for validation	129
Figure 6.17 – wakeNET predictions of R_V compared to reference data	130
Figure 6.18 – wakeNET predictions of R _I compared to reference data	131
Figure $6.19 - R_V$ values from converged trailer field data, wakeNET predictions, and BLWT	
results	132
Figure $6.20 - R_l$ values from converged trailer field data, wakeNET predictions, and BLWT	
results	133
Figure A.1 – Location of turbine site, north of Goderich, Ontario (image courtesy of Google	
Earth)	150
Figure A.2 – Layout of site. Dimensions are in m	151
Figure A.3 – Definitions of x, z, and a, for any wind direction, for obstacle 1	152
Figure A.4 – Variation of R _V , R _I , and R _P with wind sector	154
Figure A.5 – Unsheltered velocity distribution, and sheltered for wind sector 19, where R_V =	0.86.
Also shown is the turbine power curve	155
Figure A.6 – Wind roses for the site, using 30° bins	157
Figure A.7 – Wind roses for the site, using 10° bins	158
Figure B.1 – Calibration curve for probe 70919021	162
Figure B.2 – Calibration curve for probe 70919026	162
Figure B 3 – Calibration curve for probe 70919027	163

Figure C.1 – Uniformity of the simulated ABL at $x = 0$ for a variety of tunnel configurations 165
Figure C.2 – Development of flow in the longitudinal direction
Figure D.1 – Mean wind speed over time, calculated using seven different averaging periods 167
Figure D.2 – Mean normalized wind speed over time, no obstacle
Figure D.3 – Variation of mean percent difference using 5 different averaging periods
Figure E.1 – Vertical R_V profiles at a $x = 5$, $z = 0$, a = 0°, for four values of Re
Figure E.2 – Vertical I profiles at a $x = 7.5$, $z = 0$, a = 0°, for four values of Re
Figure E.3 – Vertical R_V profiles a $x = 7.5$, $z = 0$, $a = 45^\circ$, for four values of Re
Figure E.4 – Vertical I profiles at a $x = 12.5$, $z = 0$, $a = 45^{\circ}$, for four values of Re
Figure G.1 – Layout of building cluster 1
Figure G.2 – Layout of building cluster 2
Figure G.3 – Predicted and measured D_V profiles for test 1, $S_Z = 0.6$, $S_X = 0$
Figure G.4 – Predicted and measured D_V profiles for test 2, $S_Z = 0.6$, $S_X = 0$
Figure G.5 – Predicted and measured D_V profiles for test 9, $S_Z = 1.0 \text{ h}197$
Figure G.6 – Predicted and measured D_V profiles for test 7, $S_Z = 2.0 \text{ h}$
Figure G 7 – Predicted and measured D_{ν} profiles for test 6, $a = 0^{\circ}$

Nomenclature

a = obstacle orientation, degrees

 $A = \text{rotor swept area, m}^2$

AR = aspect ratio of obstacle

 C_P = turbine power coefficient

d = obstacle depth, mm

 D_p = power density deficit

 $D_v = \text{velocity deficit}$

e = model prediction error

 E_I = turbulence intensity excess

h = obstacle height, mm

I = turbulence intensity

k = roughness element height, mm

L = integral length scale of turbulence, m

N = number of training data points

p = porosity

P = power, W

 $P_{\overline{RI}}$ = precision limit of $\overline{R_I}$

 $P_{\overline{RV}}$ = precision limit of $\overline{R_V}$

PR = plan ratio of obstacle

RA = roof angle of obstacle

 R_I = turbulence intensity ratio

 R_P = power density ratio

 R_V = velocity ratio

 R_{VI} = unsheltered velocity in test section, normalized by upwind velocity

 R_{V2} = sheltered velocity in test section, normalized by upwind velocity

Re = Reynolds number of the flow around the obstacle

S = Spacing between two obstacles, normalized by h

 S_{RV} = Precision index of R_V

 S_{RI} = Precision index of R_I

t = time, s

 \bar{u} = mean wind speed between two points, m/s

 \overline{V} = mean wind speed at a point, m/s

w = obstacle width, mm

W = obstacle group width, m

x =downwind position from obstacle, normalized by h

 \dot{y} = vertical position above surface, normalized by h

z = lateral position relative to obstacle centerline aligned with flow direction, normalized by h

 z_0 = surface roughness, m

 α = wind shear coefficient

 δ = boundary layer thickness, mm

 ε = eddy diffusivity, m²/s

 κ = von Kármán constant

 ρ = air density, kg/m³

Glossary of Terms

ABL Atmospheric Boundary Layer

AWEA American Wind Energy Association

BLWT Boundary Layer Wind Tunnel

BR Bayesian Regularization

CanWEA Canadian Wind Energy Association

CFD Computational Fluid Dynamics

DNS Direct Numerical Simulation

LES Large Eddy Simulation

MAD Mean Absolute Difference

MAE Mean Absolute Error

MSE Mean Square Error

MSW Mean Square Weight

NN Artificial Neural Network

PDF Probability Density Function

PF NN Performance Function

RANS Reynolds Averaged Navier-Stokes Equations

SIS Single Isolated Structure

wakeNET Name of new NN-based wake model

WAsP Wind Atlas Analysis and Application Program

1.0 Introduction

Many wind engineering studies carried out in the past several decades have investigated the wind climate around man-made structures and natural obstacles. Knowledge of the flow around bluff bodies in a turbulent boundary layer is relevant to a wide range of fields including structural engineering, airborne contaminant dispersion, and the development and implementation of wind energy conversion systems. This thesis describes the development of a model for predicting wind fields around obstacles that can assist in the micrositing of a small wind turbine. Micrositing is the process of determining the optimum location within a potential site at which a wind turbine should be installed. Small wind turbines are typically installed in convenient, accessible locations, on much shorter towers than megawatt scale turbines. As a result, small turbines will often be close to obstacles such as buildings and trees, while large turbines are almost always located high enough above obstacles to avoid any direct influence. Although the model was developed with small turbine siting in mind, it can be applied to any problem where the wind field around an obstacle is of interest. For example, this model can predict the magnitude of sheltering on an anemometer, which is potentially a serious issue when conducting a wind resource assessment [1].

1.1 Small Wind Turbines

The Canadian Wind Energy Association (CanWEA) defines small turbines as those having a rated power output of between 300 W and 300 kW [2]. Similarly, the American Wind Energy Association (AWEA) classifies small wind turbines as those having a rated power output of 100 kW or less [3]. Other comparable definitions exist. Although there is some variance between these classifications, there is a clear distinction between small turbines and large utility scale turbines, which have rated power outputs in the megawatt range. AWEA has released a global market study on small wind turbines [3]. In 2008, 19,000 small wind turbines were sold globally,

with 10,500 units sold in the U.S. This represents an increase in U.S. small wind turbine capacity of 17.3 MW, bringing the total installed U.S. small wind capacity to 80 MW. Of the 10,500 small turbines sold in the U.S. in 2008, roughly 200 (or 2%) were intended for urban/rooftop applications, with the remainder (98%) being tower mounted. Industry predicts a total U.S. small wind capacity of 1700 MW within five years. This expected tremendous growth is largely related to a U.S. federal investment tax credit introduced in 2008, which reduces consumer costs of buying a small turbine. Based on property size and wind climate, it is estimated that there are 13 million homes in the U.S. which are suitable for a small wind turbine installation [3].

The Ontario Power Authority has recently introduced the microFIT program [4], which provides an economic incentive for farmers to develop a small wind installation (≤10 kW). A feed-in-tariff of 13.5 cents per kWh is guaranteed for 20 years, with prices escalating annually based on increases in the consumer price index. This price was set such that a turbine owner can earn a reasonable rate of return on their investment over the term of the contract. Typical lead time is 1 to 6 months. Further information is available in [4]. For installations greater than 10 kW, the FIT program is available, which has a similar price structure.

1.2 Existing Siting Methods

Micrositing is the process of determining the specific location for a turbine at a site.

Choosing a suitable location is critical to a successful wind turbine installation. When micrositing, surrounding obstacles should be taken into account. Nearby obstacles can have a strong influence on wind conditions at a site, typically reducing mean wind speeds and increasing turbulence levels at downwind locations. This is described in detail in Chapter 2. These effects are important considerations when considering the viability of a turbine at a particular location. To avoid locations where significant wake effects are present, knowledge of the structure of a wake is required. Several potential ways of learning about the structure of an obstacle's wake are discussed below.

Computational fluid dynamics (CFD) software can potentially model the flow field at any site to a high degree of accuracy, taking any nearby obstacles into account. In wind engineering, CFD approaches commonly use Reynolds Averaged Navier Stokes (RANS) turbulence models or Large Eddy Simulation (LES) [5]. Flow around buildings has been successfully predicted by CFD; for example, studies have been carried out to evaluate pedestrian comfort levels [5]. Another example is [6], where a CFD model employing a $k-\varepsilon$ turbulence model is used to simulate the flow around an array of pitched roof houses, with the goal of identifying the optimal mounting point of a small wind turbine. However, CFD is not a feasible approach to micrositing for a typical prospective small turbine owner. To obtain a reliable result, a CFD approach requires experience, knowledge, and resources. It can be difficult and time consuming to obtain accurate results; the grid must be an accurate geometric representation of the terrain and correctly discretized, realistic boundary conditions must be used, and the solution to the flow field must adequately converge. Even when set up properly, RANS based models have met with limited success [7] when predicting bluff body aerodynamics. LES solutions are more accurate, but they are computationally expensive, taking much more time and resources than RANS based models [7]. Once a flow field at a specific site is obtained, it still needs to be validated against experimental data. For each unique site, a new simulation (and validation) would have to be carried out to obtain the flow field, since different arrangements of buildings will result in different wind patterns. These factors further increase the complexity of a CFD-based approach.

Alternatively, the wind at a potential turbine location can be simulated in a boundary layer wind tunnel (BLWT) [8] to determine the effects of nearby obstacles on the wind at any point of interest at the site. While this approach has been used successfully in the past to predict flow fields, it has several of the same general drawbacks as the CFD-based approach. It is not thought feasible for a prospective small turbine owner to carry out a BLWT simulation of their specific site. A unique simulation would be required for each unique site, and the results will only be applicable to that case. Accurate scale models must be physically built, and an appropriate ABL

must be simulated. Also, it can be very time consuming to measure the flow field at a high resolution.

It should be mentioned here that of course, a potential turbine owner could hire persons with appropriate experience to perform a CFD or BLWT simulation of their site; however, it is expected that the cost of such a job is not justified for a small turbine application.

The Wind Atlas Analysis and Application Program (WAsP), a commercial wind resource assessment tool [9], takes a less intensive numerical approach than RANS or LES. In WAsP, the equations of motion are linearized to predict how wind flows over terrain [9]. The software includes a wake model to predict the effects of nearby obstacles on local wind speed. The wake model, discussed in more detail in Chapter 2, is based on a self-similar profile of the velocity deficit in the far wake of a two dimensional fence.

Wind conditions can also be directly measured, instead of simulated or modeled. If done properly, measurement is more accurate. Long term wind monitoring at a potential site prior to small turbine installation is not usually a viable option, since many landowners and prospective small wind turbine buyers do not have the financial resources, time or ability to install a meteorological tower to measure the hub height wind characteristics at their site. Equipment required includes a tower, sensors, a datalogger, and a power source, all of which can be expensive. Furthermore, if a tower is erected, the wind characteristics at the site are only measured at a few points, corresponding to the specific sensor locations. Since obstacles cause large variations in wind characteristics over short distances, wind at nearby locations cannot be accurately predicted based on the few known points. The meteorological tower approach is much better suited for large wind farms, at locations where direct sheltering is not a concern, and fiscal resources are greater.

To summarize, CFD, wind tunnel, and meteorological tower based approaches are almost always too labour or resource intensive to be practical in most cases involving small turbines.

Even if one of these approaches is taken, correct or useful results are not guaranteed. From a

financial perspective, it is not reasonable to spend a great deal of time and money to determine the optimal point at which to install a small turbine. In practice, the most common method of micrositing a small turbine is to use one of several general guidelines. One common siting rule [10] is to install a wind turbine on a tower such that it is at least 9 m (30 ft) above any obstacles within 91 m (300 ft). Another common guideline is that a small turbine should be at least 20 obstacle heights downwind, at a height greater than twice that of the obstacle [11]. Several comparable recommendations are described in [12].

Although useful, general guidelines are oversimplified, and often inadequate. They are generally based on experience, but since each site is unique, what is suitable at one site may not be at another. Potentially, the use of guidelines may result in the exclusion of many sites which are well suited for a small wind turbine, or the inclusion of sites where the turbine would still experience significant detrimental wake effects. For example, experimental evidence from a wind tunnel study by Lemberg [13] indicates that the turbulence intensity excess caused by a cube decays slowly, and can be seen at downwind distances as great as 50 cube heights. If a small turbine were to be placed 25 heights downwind of a cubic building, which is acceptable according to the "20 heights downwind, 2 high" rule cited above, it may still experience noticeable wake effects, which could be detrimental to the turbine's power output and lifespan.

1.3 Research Objectives

The primary objective of this research is to develop a new method of siting small turbines that maintains the low cost and ease of use of simple guidelines while providing increased prediction accuracy. Simple is a vague criterion, but essentially, it is meant to exclude potential solutions that are deemed to require significant resources, time, or knowledge to apply. As described above, examples of solutions that are 'not simple' include CFD, on-site wind measurement, and site specific wind tunnel simulations. It is recognized that there may not be a 'simple' way of solving this problem that always results in accurate wind predictions. That being

said, this project takes the approach of attempting to determine and develop the 'best' simple solution, which in all likelihood will not always make accurate predictions. However, this is acceptable, since it is expected that any simple model will inherently have limitations and shortcomings.

With this in mind, this thesis describes the development of a new wake model, referred to as wake NET, which predicts the mean velocity deficit and turbulence intensity excess at any point high above or in the wake of an obstacle. These predictions can then be used to assess the suitability of a point for a small wind turbine. Of main interest to small wind turbines is far field flow, since the near field is generally unsuitable, and also more difficult to predict. This thesis focuses on the far field, and to a lesser extent, the region above an obstacle. Artificial neural networks (NN) have been used to learn a relationship between the characteristics of an obstacle and its effects on the wind. This relationship forms the basis of all model predictions. Data used to develop and train the NN was obtained from the University of Guelph BLWT. Validation of the wind tunnel simulation, and by association the new model, is conducted through a comparison against the results of a full scale field experiment. An investigation into how full scale measurements made in a bluff body wake compare to corresponding measurements made in the wind tunnel is a secondary objective of this research, and clearly very related to the primary objective.

1.4 Thesis Overview

The complexities of bluff body flow and inherent difficulties associated with the creation of a theoretically-based model that is both simple and accurate are discussed in Chapter 2. It is shown that existing simple wake models do not achieve desired accuracy, and in fact, are unable to predict several significant flow features in the wake. This leads to the supposition that a model based on empirical results is preferable to a model based in theory, which in turn leads to the selection of the NN-based approach.

The remainder of the thesis describes the planning, experiments and analysis performed during model development. Chapter 3 describes the basis of the NN-based model, including the selection of model inputs and outputs. For the NN to learn the correct relationship between the inputs and outputs, it is necessary to build a large database of measurements made in the wakes of many obstacles. Chapter 4 of this thesis describes a series of wind tunnel experiments, conducted for two main purposes, both of which are tied to the development of wakeNET: i) to learn how an obstacle's characteristics affect the structure of its wake, and ii) to obtain training data, from which the NN can learn the relationship between obstacle characteristics and wake properties. Chapter 5 describes the field experiment, from which a validation data set was obtained for the wind tunnel simulations and the new model. Chapter 6 describes the creation, development, and validation of wakeNET. Finally, in Chapter 7, conclusions are drawn regarding the structure of obstacle wakes, the validity of the current wind tunnel simulation, and the suitability of using wakeNET to predict wind characteristics in the wake. Recommendations are made regarding how to improve model accuracy, generality, reliability, and scope.

2.0 Literature Review

This section reviews relevant literature on bluff bodies wakes, how wakes are currently modeled, and NNs. Mainly of interest are studies which focus on the near and far wakes of one or more bluff bodies in a turbulent boundary layer. The motivation behind many of the existing studies was to learn more about how buildings affect the wind in the ABL (or vice versa). Also discussed are existing models which predict flow properties in obstacle wakes, with varying levels of success.

2.1 Wind Characteristics Relevant to Small Wind Turbines

Certain wind characteristics are more relevant than others when considering their effect on a small wind turbine. Equation 2.1 is a general expression of a turbine's power output.

$$P = C_{p}P_{wind}A \tag{2.1}$$

$$P_{wind} = \frac{1}{2} \rho V^3 \tag{2.2}$$

 P_{wind} is the power density of the wind, given by Equation 2.2. This is the power that is available in the wind per unit swept area. C_p is the power coefficient, which is non-dimensional, and characterizes rotor performance by representing the fraction of the power in the wind that is converted to electricity. It can be thought of as the efficiency of the turbine, and varies with wind speed [14]. A is the area swept by the rotor.

As seen in Equation 2.2, the power available in the wind for a turbine to capture is proportional to the wind speed to the third power. This is the wind speed parallel to the ground; vertical flow is generally undesirable. Clearly, wind velocity at a point is an extremely important consideration when determining that point's suitability for a small turbine. Turbulence also has an effect on the power output of a wind turbine, although this is much more difficult to quantify than the effects of changes in wind speed [15]. Different wind turbines respond to turbulence in

different ways. For a typical horizontal axis turbine, higher turbulence intensity will increase power output at lower wind speeds, and decrease power output at greater wind speeds [15]. The effect of turbulence on a turbine will also depend on the turbulent lengthscales present in the flow. In the ABL, turbulence can vary greatly in scale. The integral length scale, which is characteristic of larger eddies, is typically between 10 and 500 m, while the Kolmogorov microscale, which characterizes the smallest turbulence motions, is on the order of 1 mm [16]. It has been shown that even at an unsheltered site, neglecting turbulent effects could result in overestimation of turbine power output by at least 10% [17]. Aside from decreasing power output, increased turbulence, vorticity, and wind shear can also increase the loads and fatigue on a turbine [14], potentially reducing its operating lifetime and economic viability.

2.2 Wind above Open Terrain

Knowledge of relevant wind characteristics at a potential site is crucial when determining whether or not a turbine should be installed. In an open area, with no obstacles, the variation of mean wind speed \overline{V} with height z can be described by the power law, a simple form of which is shown in Equation 2.3 [18].

$$\frac{\overline{V}(z)}{\overline{V}_{ref}} = \left(\frac{z}{z_{ref}}\right)^{\alpha} \tag{2.3}$$

 $\overline{V_{ref}}$ is the mean wind speed at the reference height z_{ref} . The shear coefficient α is unique to a site and depends on many factors including the surrounding terrain and atmospheric stability [14]. The power law can be used to predict the wind speed at any vertical height within the atmospheric boundary layer (ABL) based on a single known wind speed and the local shear coefficient. In an open, fully developed boundary layer flow, such as the wind blowing over uniform flat terrain, predictions made using the power law tend to be fairly accurate [14]. In a shear flow, such as in or near an obstacle's wake, power law predictions will not be accurate

because the magnitude of the shear will vary significantly with height. The presence of the obstacle abruptly changes the surface roughness z_0 .

Another method commonly used to predict the wind speed at any height in an open area is the log law. The log law is a theoretically based self-similar solution for the mean wind speed parallel to the ground [14]. A common form of the log law used in wind engineering is given in Equation 2.4.

$$\frac{\overline{V}(z)}{V_T} = \frac{1}{\kappa} \ln \left(\frac{z}{z_0} \right) \tag{2.4}$$

Again, the velocity \overline{V} is predicted as a function of height z. The friction velocity V_T is a constant related to the shear stress in the flow. κ is the von Kármán constant, and z_{θ} is the surrounding surface roughness.

The Reynolds decomposition expresses the velocity at time t in terms of its mean and fluctuating components, \overline{V} and V as shown in Equation 2.5.

$$V(t) = \overline{V} + V'(t) \tag{2.5}$$

 V_{rms} is the root mean square (rms) value of the fluctuating component [18], as shown in Equation 2.6.

$$V_{rms} = \sqrt{\overline{V^{12}}} \tag{2.6}$$

Longitudinal turbulence intensity is defined in Equation 2.7, where V_{rms} and \overline{V} are both a function of height.

$$I(z) = \frac{V_{rms}(z)}{\overline{V}(z)} \tag{2.7}$$

The longitudinal turbulence intensity profile in an open flow is described by Equation 2.8, where constants c and d are defined by ASCE [18] for different types of terrain, and are analogous to the shear coefficient α . For "open country" terrain, c and d have values of 0.20 and 0.15, respectively [18].

$$I(z) = c \left(\frac{z}{10}\right)^{-d} \tag{2.8}$$

For Equation 2.8 to be valid, rms fluctuations cannot vary significantly with height. This is akin to assuming constant shear stress (friction velocity) in the log law [18]. The assumption of constant V_{rms} is generally true in the surface layer of the ABL, up to between 50 and 100 m. Above the surface layer, in the Ekman spiral layer, this assumption is no longer valid.

2.3 Effect of an Obstacle on the Wind

Predicting how a nearby obstacle will affect the wind speed and turbulence at a point of interest requires an understanding of the flow around a building, which can be very complex. To illustrate the problem, a brief qualitative description is given here of the flow around a simple building, fully submerged in the ABL. Peterka et al. [19] explained the main features of the flow field near an isolated simple building. Figure 2.1 shows the mean streamlines of the flow.

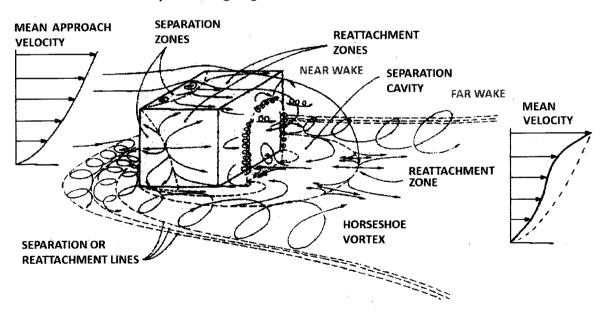


Figure 2.1 – Mean streamline patterns about a building, adapted from [20]

The incoming flow is assumed to be a fully developed boundary layer in an open area, with mean velocity and turbulence intensity profiles as described in the previous section. The dominant wind direction is perpendicular to the front of the building. Upwind of the building, the

flow separates at a distance dependent on several factors including building width, building height, and upstream surface roughness. This separation induces a downward flow on the lower front part of the building and generates large primary and smaller secondary vortices. This separated flow wraps around the building in a horseshoe shape (this is known as a horseshoe vortex). On the upper part of the front of the building, a stagnation region forms. At or near the front and side edges, the flow separates; depending on the depth of the building, it may or may not reattach to the top and sides. In either case, the rear face of the building is covered by a separation cavity. Figure 2.1 illustrates that streamlines coming from a separation point on the top of the building wrap around and enter the recirculation region inside this cavity. Further downwind, the flow will reattach to the ground. The mean streamline that reattaches to the ground originates upwind of the building and not at the separation point on the top. The total length of the cavity will depend on building geometry; it typically varies from two to six building heights. The region extending from the building to the reattachment zone is part of the near wake, as in seen in Figure 2.1; associated characteristics include high turbulence, vorticity, and reverse mean flow.

After reattachment, downwind of the building, the wind recovers and becomes similar in form to the approaching boundary layer. This region is defined as the far wake, as seen in Figure 2.1. Here, some effects caused by the building are still evident. Compared to the upwind flow, mean wind velocities are lower, turbulence intensities are higher, and scales of turbulence are smaller. The drag on the obstacle in the wind has effectively created a momentum deficit in the flow. There may also be remnants of standing vortices from the building, with rotation axes parallel to the wind direction. Moving downwind, these effects gradually disappear (unless the wind is redisturbed by another obstacle), and the wind will reattain its undisturbed characteristics. Decreased velocity and increased turbulence levels associated with both the near and far wake would greatly affect the power output of a small wind turbine located in either of these regions [14].

2.4 Wakes of Bluff Bodies

Although groups of obstacles are more common than single isolated structures (SIS), flow around the latter is much simpler, making it an excellent starting point for an investigation into the flow around obstacles in general. A large amount of literature is available on the wake of a single bluff body. These studies range from experimental, carried out in a BLWT [13] or in the field [21], to numerical, using turbulence modeling, LES, or Direct Numerical Simulation (DNS) [6] [22].

A bluff body is defined here as a body with a broad, flattened front. In bluff body flows, pressure drag dominates over friction drag. For example, a cube is a bluff body, but an airfoil is not. Most buildings are considered to be bluff bodies, as are all obstacles investigated in this thesis.

For prismatic bluff bodies, the aspect ratio AR is defined in Equation 2.9 as the ratio of the obstacle width w to height h. Specifically, w is the obstacle's dimension in the direction normal to the wind, when the wind direction is normal to the obstacle's front face. The plan ratio PR is defined as the ratio of the obstacle depth d to h, as expressed in Equation 2.10. Specifically, d is the obstacle's dimension in the direction parallel to the wind, when the wind direction is normal to the obstacle's front face. w and d are constant for each obstacle, and independent of model orientation a, since they are defined for the case where wind is normal to the front face of the obstacle.

$$AR = \frac{w}{h} \tag{2.9}$$

$$PR = \frac{d}{h} \tag{2.10}$$

In this thesis, x is defined as the distance downwind from the centre of the obstacle, y is defined as the vertical height from the ground, and z is defined as the lateral distance from the

obstacle centerline, which is parallel to the wind direction. x, y, and z are all normalized by the obstacle height h, unless otherwise explicitly stated.

One of the most common bodies (or obstacles) used is a long $(AR \to \infty)$, thin $(PR \to 0)$, solid wall, referred to here as a two-dimensional wall. Another common bluff body is the cube, with the front face normal to or at an angle to the wind direction. Other bluff body studies focus on rectangular obstacles [23][24][25] of various AR and PR. Several existing studies also examine the effect of a on the obstacle's wake [13][24].

Although the specific degree of upwind turbulence will have an effect on the magnitude and extent of an obstacle's wake, this effect is expected to be small for the range of turbulence levels commonly seen in a rural ABL. In studies such as those described here, the boundary layer is often described as 'fully turbulent'. It is thought that even greater turbulence levels would decrease the size of the wake due to the increased mixing associated with turbulence [19].

2.4.1 Two Dimensional Fence

A solid two-dimensional fence is an example of a geometrically simple bluff body, since its shape is fully defined by a single geometric parameter, the height of the fence. Examples of real obstacles in the environment that are similar to a two-dimensional fence include fences or hedgerows with low porosity, and long, solid tree lines, all of which are common features in rural areas. Counihan et al. [26] deduced an analytical theory which describes the mean velocity deficit behind a two-dimensional fence. They compared this theory to wind tunnel measurements and full scale field measurements of the wind behind windbreaks. They found that the maximum velocity deficit behind a solid two-dimensional fence decays with x^{-l} , where x is the downwind distance normalized by h, the height of the fence. The recirculation zone extends to roughly 6 h downstream. The flow becomes self-similar between 25 and 30 h downwind, with typical wake effects such as decreased wind speeds and increased turbulence intensity still evident beyond this point.

2.4.2 Cube

Although the vast majority of buildings are not strictly cubical, there are many studies of boundary-layer immersed cubes. While a relatively simple shape, flow fields around cubes will share many features with the flow around other sharp edged bluff bodies. Lemberg [13] presents a theoretical and wind tunnel investigation of the wakes behind obstacles with square and circular plan sections (plan section refers to the obstacle's footprint). Mean velocity deficit and turbulence intensity profiles and contours were measured inside the wakes. Lemberg found that the maximum velocity deficit on the centre plane in the wake of a cube decays as $x^{-1.58}$, when the cube is oriented normal to the wind direction. The mean velocity wake did not measurably extend beyond 15 h downstream when the cube was oriented normal to the flow, or when the cube was oriented at 45° to the wind direction. The turbulence intensity wake downstream of the normal cube was found to extend much further, decaying as $x^{-0.24}$ and returning to its undisturbed boundary layer value at 50 h downstream. Other studies have also examined the flow around a cube. For example, Counihan's cube results, as reported by Lemberg [13], are used for comparison purposes in Chapter 4.

2.4.3 Prismatic Obstacles

Hansen et al. [24] measured the longitudinal mean velocity and turbulence intensity in the wake of a rectangular model building exposed to a simulated atmospheric boundary layer in a wind tunnel. Three models were used, of different sizes but identical proportions; all had an AR of 2.44, and a PR of 0.75. The wake was studied for two model orientations: when the flow is normal to the longer face of the building ($a = 0^{\circ}$), and when the flow is at an angle of 47° to the building ($a = 47^{\circ}$), which was found to produce the best defined pair of vortices from the front corner of the block. For the normal flow case, the wake formed symmetrically about a vertical plane through the centreline of the model. A horseshoe vortex system was observed around the base of model, however, no other strong, standing vortex patterns were observed. The horseshoe

vortices did not persist to form standing vortices in the far wake. It was found that the velocity decreased everywhere in the flow field except for near the building, where the flow must accelerate to go around the model. The mean velocity and turbulence wakes were evident until 18 h downstream. As downwind distance increased, so did the maximum width of both the velocity and turbulence wakes, until the width reached roughly five building widths at 12.8 h. The wake narrows at greater heights above the ground. The mean velocity wake decayed roughly as $x^{-1.55}$ for two larger size models, and $x^{-1.85}$ for a smaller model.

In the case with $a = 47^{\circ}$, the wake structure observed by Hansen et al. [24] was much different. The turbulence intensity exhibited similar behaviour to the normal flow case, decaying relatively quickly to within 15% of its free stream value by approximately x = 18, after which it decayed very slowly to its free stream value. The velocity wake was still evident at downstream locations as far as 80 h. The authors explained the much greater wake persistence seen at this orientation by considering the standing longitudinal vortices, which form at the model's prominent points, as seen in Figure 2.2.

The only mechanism through which the angular momentum of these vortices is dissipated is viscous or turbulent stress acting about the axis of the vortex. Thus it was thought that the formation of these vortices greatly increases the extent of the velocity wake, and will significantly affect the structure of the far wake. These vortices are extremely persistent and cause a definite swirling character in the wake.

Hansen et al. [24] also measured an increase in longitudinal wind speed at some lateral positions in the wake, which persisted downwind along with the standing vortices. They propose that the velocity increases because the two standing vortices both rotate such that air is swept downwards to the ground, and out of the wake in the lateral direction. This causes greater entrainment of higher speed wind from above.

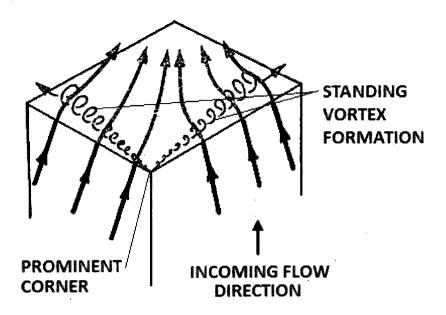


Figure 2.2 - Vortex formation on the roof of a rectangular building. Adapted from [20]

Martinuzzi and Tropea [25] studied the flow around multiple surface mounted prismatic obstacles, of varying AR, in fully developed channel flow. Channel flow is bound by walls to the sides and by a barrier (such as a ceiling) above. While there are differences between channel flow and turbulent boundary layer flow, results from their study can still give insight into the effect of AR on the wake of an obstacle. This investigation was conducted using flow visualization experiments, so the results are mainly qualitative. It was found that the reattachment length of a three-dimensional obstacle was much less than that of a two-dimensional obstacle and, in general, three-dimensional obstacles had shorter recovery regions. The flow was always three-dimensional in nature, even in the case of a two-dimensional fence. Vortices generated in the shear layer influenced the downstream recovery region. The separation bubble formed around an obstacle was not closed; fluid was convected in and out of the separation cavity. Downstream of an obstacle, the width of the wake decreased to the reattachment point, and then increased after. The wake expanded rapidly after reattachment. Further downstream, wake growth was slower and was mainly due to entrainment of fluid from the surrounding flow. Flow acceleration over an obstacle depended on its AR. Significant mean cross stream velocity components were seen behind the

cube at up to x = 20. Reattachment length increased linearly with obstacle AR, up to about a value of 4, after which it approached roughly 7.2. Flow aft of an obstacle with a small AR was dominated by the interaction of the horseshoe vortex, the recirculation vortices, and the reattaching shear layer. For larger AR, the effect from the horseshoe vortex was observed mostly along the edges of the wake. The inner portion of the wake could be considered the same as the two-dimensional case for AR greater than about 6.

The downstream location at which the flow reattaches is of great interest, since it can be thought of as the boundary between the near wake and the far wake (alternatively, the start of the far wake could be defined as the point at which the flow becomes self-similar). Table 2.1 shows how obstacle AR affects the location of the start of the development region, which is defined here as the point at which the wake begins to decay at a constant rate. Values for the start location were calculated from plotted velocity deficits found in [19]. Also shown in the table is the rate of decay of the maximum mean velocity deficit for each obstacle, as reported by Peterka et al. [19]. Table 2.1 applies to the case where the front face of the obstacle is normal to the dominant flow direction.

Table 2.1 – Effect of aspect ratio on the start of the development region, based on [19] unless noted.

AR	Start of the development region (x)	Decay rate
∞	6 - 7.5 [26]	~-1 [27]
4	5	-1.48
3	4.2	-1.37
1	1.9	-1.18
0.33	0.65	-1.06
0.25	0.37	-0.97

Frost et al. [21] conducted a field test measuring the wind around a full scale simulated building, which was a rectangular obstruction with an AR of 8.4 and a PR of 0.75. Measurements were taken at ten towers, spanning a range from 8.7 h upstream to 42.4 h downstream. A wind tunnel study was conducted on a scaled building, and results from the two studies were compared. The field data possessed all characteristic features from wind tunnel studies of building flows. The mean velocity wake was found to decay as $x^{-1.55}$, which agreed well with the wind tunnel results of Hansen et al. [24]. However, in order to obtain this decay rate, effects of nearby trees had to be subtracted. Comparisons to the results of Frost et al. are not made in this thesis, since they are in a form that is not directly comparable to current measurements.

2.4.4 Reynolds Number Dependence

In wind tunnel experiments, it is widely assumed that the flow around a bluff body is independent of Reynolds number Re above a critical Re value of 2 to $3 \cdot 10^4$ [28]. In bluff body studies, Re is defined based on the height of the obstacle and the mean upwind flow speed at obstacle height. v is the kinematic viscosity.

$$Re = \frac{h \, \overline{V(h)}}{V} \tag{2.11}$$

Re independence is a very useful assumption, since it implies that the flow is independent of scale, as well as the incoming flow velocity. A BLWT simulation of a full scale flow relies on the validity of assuming Re independence.

A recent study carried out by Lim et al. [29] questioned the validity of this assumption for the mean and fluctuating flow quantities in close proximity to a full scale bluff body fully submerged in an ABL. It was found that flow dependence on *Re* depends on the specific quantities that are desired and the orientation of the bluff body. When the flow was normal to the front face of the cube, such that no strong concentrated vortex motions were present, the mean normalized velocity and pressure profiles in proximity to the bluff body were found to be *Re*

independent above $Re = 3.0 \cdot 10^4$, which is consistent with conventional wisdom. The maximum Re investigated was on the order $4.4 \cdot 10^5$ in the wind tunnel, and $2 \cdot 10^6$ in the field. Since there is no theoretical justification for a Re trend over a higher range when a trend does not exist in the lower range, any Re independence found was assumed to extend to Re greater than those investigated. Findings regarding fluctuating quantities were different than those for mean quantities. The fluctuating velocity and pressure profiles may show a dependence on Re.

In the case where the incoming flow was at an angle of 45°, clear *Re* effects were found to exist in the mean flow field. Fluctuating quantities also showed *Re* dependency. These effects are most evident in regions close to the cores of vortices. At locations further from concentrated vortices, *Re* effects are weaker.

In general, the validity of *Re* independence depends on the kind of flow as well as the particular quantities of interest. Recall that the above findings apply to the measurements taken in close proximity to the cube; they may not apply to measurements taken in the wake region. In the current study, dependence of the flow on *Re* was examined for the wake region, and is discussed in Chapter 4.

2.4.5 Locations of Maximum Wake Effects

Two key features of interest in a wake, at a given x position, are the y and z coordinates of the maximum velocity deficit and the maximum turbulence intensity excess. Lemberg [13] found that as downstream distance increased, so did the vertical position of the maximum velocity deficit. The turbulence intensity of a three dimensional wake was found to be at a maximum near obstacle height. When the cube is orientated normal to the flow, the maximum velocity deficit occurred along the cube's centre plane. Hansen et al. [24] found that when the front face of their obstacle was normal to the flow, the maximum velocity deficit in the wake occurred on the centre plane, which agrees with the findings of Lemberg. However, when their block was turned to an azimuth angle of 47° , the maximum velocity deficit and turbulence intensity ratios occurred at

lateral positions well off the centre plane. The wake of the block was clearly asymmetrical. The lateral position of the maximum velocity deficit increased with downwind position. At x = 18.5, the velocity deficit was at a maximum at z = 2, with a value of 5%. At the opposite lateral position, the velocity deficit had nearly recovered.

2.5 Wakes of Multiple Obstacles

Musselman [23] carried out an investigation into how the wakes of multiple structures combine in a turbulent boundary layer, with the purpose of predicting contaminant dispersion near buildings. The main group of buildings studied consisted of three identical cubes, of separation distance S, which was constant between the cubes. Tests were performed using S values ranging from closely spaced (S = 0.3 h) to nearly isolated (S = 3.0 h). Also tested were double rows of cubes, with three in the first row and two in the second row.

For the single row of cubes, Musselman found that if the bodies are close enough together $(S \le 1.5 h)$, then the wakes of the cubes will experience significant interaction. In the near wake, the mean velocity deficit is tri-modal, with a peak centered behind each cube. As seen in Figure 2.3, regions of large velocity deficit occurred downwind of the gaps between structures.

Musselman explained that jets formed in between the cubes (at 'B'), after which streamlines were drawn back into the low pressure cavity region behind each obstacle ('A'). This is similar to the flow through a diverging nozzle; as the streamlines diverged downwind of the gaps, the wind became slower. The lateral velocity deficit profiles through 'C' in Figure 2.3 are bimodal in shape. The same mechanism that caused the velocity deficit at 'C' caused a speed reduction at 'D', along the centerline of the obstacle group. At this point, the mean velocity wake had coalesced into a single, uni-modal wake, to which SIS theory could be successfully applied. The wake was uni-modal in the sense that the lateral velocity deficit profile contains a single large peak, which was the result of the combined wakes of the three cubes. However, this uni-modal velocity deficit only became evident at large downwind distances. The length of each

region depended on the obstacle AR, the spacing S, and the number of obstacles. A smaller spacing decreased the length of the uni-modal and bi-modal regions. At a spacing of 0.3 h, these regions nearly disappeared. Musselman observed that for this spacing, the wake was very similar in structure to that of a SIS.

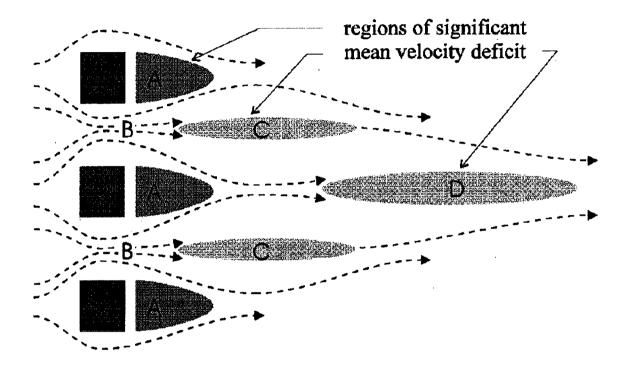


Figure 2.3 – Schematic representation of flow regions around multiple structures, from [23]

The above theory is strongly supported by experimental evidence from Musselman's BLWT tests. Expanding this theory to other groupings, Musselman proposed that a group of obstacles with *n* structures will form an '*nth*' modal wake, with each velocity deficit peak corresponding to an obstacle. The reduction by one of deficit peaks continues in the far wake until a single uni-modal deficit region exists. When a second row of two obstacles was added, Musselman found that in general, uni-modal behaviour was evident at smaller downwind distances. Again, this depended on the spacing between the obstacles; with a large spacing, the flow through the group was significant, causing the shape of the wake to become fairly complex and dissimilar to that of a SIS. When the spacing was small, a large percentage of the flow was

diverted around the group, resulting in a wider, more uniform contour of mean velocity deficit in the wake.

From experimental results, Musselman developed an empirical model which can predict the velocity deficit along the centerline of the wake as a function of spacing, number of obstacles, and obstacle AR. While useful, this model is limited in scope. All obstacles must be in a single row, and normal to the wind direction. As well, it was developed assuming constant S and AR, and only predicts the velocity deficit at obstacle height. Obstacles present in another row are not taken into account; the significance of this simplification depends on the spacing.

Taylor and Salmon [30] make a set of recommendations regarding how to combine wake effects from multiple obstacles. Their model uses linear superposition to determine the effects of multiple obstacles on the velocity deficit at a point; the velocity perturbation induced by each obstacle is calculated separately and combined linearly to get the total sheltering effect. Taylor and Salmon state that if two or more obstacles are in line upwind of the sheltered site, then superposition will overestimate sheltering effects, and the resulting velocity deficit should be adjusted appropriately (or the smaller obstacle should be ignored).

The sheltering model of WAsP, which is based on Perera's empirical model [1], uses an approach similar to that of Taylor and Salmon. Sheltering effects of multiple obstacles are combined linearly to predict the degree of sheltering in the wake of an obstacle group. Within WAsP, it is also possible to take obstacles into account by manually inputting wind speed correction factors for each wind direction.

2.6 Existing Wake Models

This section describes existing models that can predict flow characteristics in obstacle wakes. Two main approaches to creating a wake model have been identified. The first is to start with the governing flow equations and make simplifications and assumptions such that they can be solved analytically (for example, constant eddy viscosity), with some empirical values and

constants required. For constant property Newtonian fluids, the governing equations are the Navier-Stokes equations [31], given in general form in Equation 2.12, and the continuity equation, given in Equation 2.13. Air in the surface layer of the ABL is assumed to be a constant property fluid, which allows these equations to be applied to the wind.

$$\rho \frac{DU_{j}}{Dt} = \mu \frac{\partial^{2} U_{j}}{\partial x_{i} \partial x_{j}} - \frac{\partial P}{\partial x_{j}} - \rho \frac{\partial \psi}{\partial x_{j}}$$
(2.12)

$$\frac{\partial U_i}{\partial x_i} = 0 \tag{2.13}$$

Indices j and i represent the direction of velocity U and distance x (i is the repeating index; j is the non-repeating index). ρ is density of air and P is pressure. ψ is the gravitational potential.

One of the earlier attempts at modeling a wake was carried out four decades ago by Mons and Sforza, as reported by Lemberg [13], who formulated a theory for the wake behind a leading edge obstacle in purely laminar flow. To simplify the governing flow equations, it was assumed that there was a relatively small difference between the local mean velocity and the free stream velocity. This assumption allowed higher order terms in the governing equations to be neglected. A constant eddy viscosity was used in each direction to relate the normal and transverse shear stresses to the mean velocity gradients. It was assumed that the two eddy viscosities were proportional to the corresponding obstacle dimensions. As boundary conditions, a constant velocity deficit was assumed in a rectangular region close to the obstacle, and it was assumed that there was no velocity deficit far from the obstacle. This model had poor agreement with measurements made in the wake of a three dimensional obstacle.

Hunt and Smith [32] developed a momentum-wake theory to provide quantitative predictions of the velocity deficit in the wake of a three-dimensional obstacle. Again, to simplify the governing equations, they assumed that the velocity deficit was small, which means that the theory is only valid for the far wake region. Two constant eddy viscosities were used, for the lateral and vertical directions. These were expressed as a fraction of the eddy viscosity of the

incoming flow; thus, eddy viscosities were calculated from properties of the incident boundary layer. Hunt and Smith related the moment of the mean velocity deficit in the wake to the overturning moment exerted by the flow on the obstacles, which is analogous to saying that the momentum deficit is equal to the drag force. Predictions made by the model developed using this theory agreed reasonably well with Counihan's data [13] for the wake behind a cube. However, it was necessary to specify values of two parameters in order to obtain the best fit.

Based on the theories of Hunt and Smith [32] and Mons and Sforza (reported by Lemberg) [13], Lemberg [13] created a more general model which incorporates an expression for eddy viscosity as a power law function of height above the ground. As well, eddy viscosity is proportional to the height and frontal width of the obstacle. Experimentally determined power law constants were used to predict how eddy viscosity varies throughout the flow; however, in practice, values of these coefficients are difficult to determine [30]. As in the theory of Hunt and Smith [32], the forms of the velocity profiles in the vertical and lateral directions must be assumed.

Based on the work described above, as well as the work of Perera [27], discussed below, Taylor and Salmon [30] developed a model to correct anemometer measurements for sheltering by upwind obstacles. Their model can be used to estimate the velocity deficit that would be observed by an anemometer at a specified location in an obstacle's wake. Model inputs are the length, width, and height of the obstacle, its base (overturning) moment coefficient when exposed to the wind, its position upstream of an anemometer site, and the local surface roughness.

In the development of Lemberg's model, which influenced Taylor and Salmon's model, it was necessary to make a series of simplifications and assumptions to reduce the governing equations to a solvable form [13][30]. Perhaps the most important of these is the commonly used turbulent viscosity hypothesis, in which the Reynolds stresses are assumed to be proportional to the strain rate in the flow [31]. While very useful, the accuracy of this hypothesis is known to be poor for many classes of flows [31], especially those which are complex. Algebraic models of

eddy viscosity, such as the zero equation model used by Lemberg to express eddy viscosity in terms of position above the ground, generally perform poorly in shear flows [7].

By assuming that the velocity deficit is small, the model predictions are limited to the far wake region, described by Lemberg [13] as starting approximately 5 h downwind of the obstacle. Other authors use different definitions of the start of the far wake (for example, Perera [19] uses a rough value of 7.5 h downwind of a wall). In fact, the start of the far wake will be dependent on the specific obstacle. Another necessary assumption is the functional form of the velocity deficit in the vertical and lateral directions. The vertical self-similar profile is based on the work of Perera [27]. The lateral velocity deficit is assumed to be symmetrical, with a Gaussian form. This may be a reasonable approximation for flow fields around simple geometries, such as the flow around a cube oriented normal to the wind. For more complicated flows, such as around a cube with an azimuth of 47°, experimental evidence clearly shows that the velocity deficit distribution is not Gaussian or symmetric (for example, see Figure 6.13). Taylor and Salmon [30] do not consider the 'vortex wake', and state that when present, vortices could lead to velocity deficits significantly different than those predicted by their model. As discussed by Hansen et al. [24], and shown in Figure 2.2, vortices are formed in the wake when the obstacle is presenting salient edges to the wind direction. This implies that although Taylor and Salmon's [30] model is suitable for simple cases, such as a cube with its front face normal to the flow, predictions may be poor for more complicated flow fields, such as when an obstacle's front face is not normal to the flow. Another important issue is that Taylor and Salmon's [30] model predicts only mean wind speeds, and does not provide guidance regarding turbulence levels in obstacle wakes, which is a crucial consideration when siting a small wind turbine. Comparisons of experimental data to Taylor and Salmon's [30] model are shown in Chapters 4 and 6.

A theoretical approach along the lines of Hunt and Smith [32] and Lemberg [13] was considered for the wake model to be developed in this thesis. There are several ways in which their existing models could be refined. More accurate expressions for eddy viscosity could be

developed for a range of obstacles. Better similarity profiles in the vertical and lateral directions could be obtained based on wind tunnel data. More accurate overturning moment coefficients of common obstacles could be measured. The theoretical model could be validated based on wind tunnel data. While this approach does show promise for simpler bluff body flows, it is thought that its accuracy is inherently limited because of the assumptions made in its development, mainly the turbulent viscosity hypothesis and the negligence of higher order terms in the governing equations. It is speculated that there may be potential in an approach similar to this, in which an empirical expression for eddy viscosity is developed based on wind tunnel data. Higher order terms would not be neglected; instead, a solution to the governing equations would be found using numerical methods. With an appropriate simple algebraic expression for eddy viscosity (essentially making it a zero equation model [31]), a numerical solution would be easier to implement; convergence would be quicker and more reliable, and potentially, a flow field could be obtained in a reasonable amount of time. This approach was not considered for this project due to the criterion that the solution be simple.

The second main approach to wake modeling is more empirical; it is assumed that in the far wake, the flow becomes self-similar, and predictions are made based on similarity profiles measured in wind tunnel experiments. Perera [27] developed a set of empirical relations which estimate the velocity deficit and Reynolds stresses at any point downstream of a two-dimensional fence. These correlations are based on measurements made during wind tunnel tests, similar to those carried out by Counihan [26]. Perera's [27] correlations are expressed in terms of self-preserving, non-dimensionalized variables. The porosity of the fence is taken into account as well. A model has been created that predicts mean wind speed in the wake of an obstacle, based on the similarity profile of the velocity deficit in the far wake of a two-dimensional fence.

Perera's model [27] is the basis for the sheltering model used by WAsP [1]. WAsP considers all obstacles to be boxes with a rectangular cross section, and footprint. Within WAsP, each obstacle is defined by i) its height, ii) its porosity, iii) the distance from the point of interest

(where the sheltering effect is to be predicted) to the two extreme side corners of the 'box', and iv) the angle subtended from the point of interest to the two extreme corners [1]. Troen and Petersen provide additional details about how the sheltering model works, as reported by Taylor and Salmon [30]. The magnitude of any sheltering effect at a point depends on wind direction. The WAsP model uses 30° bins, which means that the predicted degree of sheltering is identical for any wind direction within each 30° sector. The sector that contains the particular wind direction of interest is further subdivided into 8 segments. If an obstacle is at all present in a segment, then the sheltering experienced for wind from that segment is assumed to be the same as the sheltering that would be experienced if a two-dimensional wall were present in that location. If an obstacle is not present in a segment, then the sheltering is zero. The presence of an obstacle in each of the eight segments is examined. The predicted sheltering effect from that sector is the average of the sheltering values of the eight segments.

Perera [27] also developed self-similar solutions for the shear and normal stress excesses in the wake of a two-dimensional wall, which are of similar form to the relation for velocity deficit. In this thesis, for comparison purposes only, the relation for excess normal stress is adapted into a simple model that predicts turbulence intensity in the wake of a three-dimensional obstacle. It should be emphasized that using Perera's normal stress relationship in this way was not seen anywhere in the literature; however, it logically follows the use of Perera's relationship for velocity deficit, which was present in the literature [1] [30]. Perera's turbulence intensity model is structured identically to the velocity deficit model, but uses a relationship which predicts normal stress excess instead of a relationship for velocity deficit. Turbulence intensity predictions for a two-dimensional fence are adapted to a three-dimensional obstacle in the same manner as velocity deficit predictions for a two-dimensional fence.

The method described above is a very simple way to adapt a two-dimensional relation to a three-dimensional obstacle, but as Taylor and Salmon noted [30], it tends to greatly over predict the sheltering caused by three dimensional obstacles. However, it appears to make accurate

predictions for two-dimensional obstacles such as fences or tree lines [1], when the flow is normal to the obstacle. It is thought that the process of treating a three-dimensional obstacle as two-dimensional has inherent difficulties, since three-dimensional obstacles cause fundamental differences in flow characteristics compared to those originated by a two-dimensional obstacle [19]. Also, Perera's [27] self-similar correlations are only valid in the far wake zone (roughly 7.5 obstacle heights downstream), which greatly limits the applicability of the model for small wind turbine siting. In this thesis, comparisons are made to 'Perera's model'. It should be kept in mind that while Perera [27] developed the self-similar profiles, the process of utilizing them to make predictions for three-dimensional obstacles was developed by others [33].

2.7 Other Wake Modeling Approaches Considered

As mentioned previously, wakeNET was developed using a NN-based approach. This section discusses several other general methods that were also considered as possible ways of predicting the effect of a building on the wind, which leads to an explanation of why the NN based method was chosen. Each approach was evaluated based on its estimated likely accuracy, simplicity, ease of implementation, and generality, which is defined as the ability of a model to make accurate predictions for cases that were not used to develop the model. In all cases, the model would either be based on or validated with experimental data, consisting of wind tunnel measurements made of the flow in obstacle wakes.

Perhaps the simplest 'modeling' approach that was considered was to tabulate wind data for a wide range of obstacles at a high spatial resolution inside the region of influence. Wake properties for any obstacle could then be 'predicted' by looking at the tables for that obstacle, interpolating between known points, if necessary, and scaling to the obstacle's size. This is an attractive option because it is very simple, easily implemented, and accurate for known points. The main drawback to this option is that poor generality is expected; a linear interpolation between different *AR*, *PR*, roof angles, and the coordinates of the position of interest could easily

result in inaccurate predictions. Poor generality could be solved by increasing the resolution of measurements for all inputs; measurements could be made at a greater number of points in the wake, model orientations, aspect ratios, plan ratios, and roof angles. However, this approach was deemed impractical due to the almost infinite amount of wind tunnel time that would be required to build the database to a sufficient resolution.

Another approach considered was to make predictions based on known wake decay rates. As discussed previously, some empirical evidence suggests that in the far wake of an obstacle, the maximum velocity deficit will decay at a roughly constant rate. However, as reported by Peterka et al. [19] and shown in Table 2.1, the value of the decay rate appears to depend on the geometry of the obstacle. In the current study, the velocity deficit across the entire wake (at all heights and lateral positions) is of interest, not just the maximum. A decay rate would need to be defined at all vertical and lateral positions, to predict how velocity deficit changes in the *x* direction. The magnitude of velocity deficit at the start of the far wake would also need to be known. Equation 2.14 shows the form the wake decay model would take, as found in figures from Hansen et al. [24], Lemberg [13], and Frost [21].

$$D_{y} = C(z, y) \cdot (x)^{m(z, y)}$$
 (2.14)

 D_v is the velocity deficit at a point in the wake. The initial magnitude of the wake disturbance, C, is defined at each vertical y and lateral z position. Similarly, the wake decay rate m is a function of vertical and lateral position. The choice of geometric scaling parameter (here h) does not affect the wake decay rate m. Modeling based on wake decay quickly becomes complicated when it is considered that C, m, and the start of the universal decay region would all need to be defined for each unique obstacle, at each obstacle orientation. This approach also requires the assumption that at all points, the velocity deficit always decays, and that no wake spreading occurs; both of these assumptions can easily be shown as invalid by looking at the results of wind tunnel tests [24][13]. While this may be a suitable method of modeling the

maximum velocity deficit in a wake, it is not suitable for making predictions of more general flow characteristics throughout the wake.

2.8 Neural Networks

As discussed previously, there are significant inherent difficulties associated with developing an accurate and simple theoretical model. It was decided that an empirical approach to wake modeling was preferable, and that the NN-based approach showed the most promise.

Creating a model based on a relationship learned using NNs is a form of non-linear regression.

This approach has the potential for high accuracy and easy implementation. As well, some types of NNs have the potential for high generality [34]. The NN approach was chosen over other non-linear regression methods mainly because a NN has the ability to adapt when presented with new information. In this way, a NN model has the potential to continually become better at solving a problem over time.

2.8.1 Operation

A NN-based model is empirical because it is based entirely on velocity measurements made in the wind tunnel. Although theory was essential in developing the model (for example, when choosing NN inputs and outputs, and deciding what training data is required), this theory was not used to learn the relationship between the model's inputs and outputs. A brief explanation of NNs follows. For more information, there are numerous resources available (e.g. [34], [35]).

A NN consists of an interconnected group of artificial neurons. An artificial neuron is essentially a mathematical function designed to be a crude model of a biological neuron. Typically, each neuron will have multiple inputs and outputs. Outputs are a function of the inputs. Each input to the neuron is weighted based on its source (for example, all inputs to neuron #2 that come from neuron #1 will be weighted identically). The weighted inputs are added together, along with the bias value, which is unique and constant for each neuron. This sum is put through a transfer function to determine the neuron's output, which is then 'sent' to the next neuron(s),

where it is received, weighted, and added to a sum. The output of the last neuron(s) in the process is the final NN output. The specific values of the weights and biases for each neuron are determined using a training algorithm with a set of known correct inputs and outputs (referred to as the training data). In this way, the NN is trained using a large number of known data points, which act as examples of how the model should make predictions. Each data point consists of an input vector, containing a value for each model input variable, and a target vector, containing the correct value for each output variable, corresponding to the inputs. Training with a large enough number of data points allows the NN to effectively learn how the outputs are related to the inputs. Once trained, NNs can potentially make accurate predictions when presented with a set of inputs that were not used in the training data. As with any empirical relationship, care must be taken that the data is not overfit (or over trained). Methods used to avoid over training are described in Chapter 6.

2.8.2 Applications of Neural Networks to Wind Engineering

There are many examples where NNs are used to empirically model complex relationships between two or more variables, three of which are described here. Bitsuamlak et al [36] used a NN approach to predict wind speed-up over terrain features, specifically, isolated hills, double hills, and triple hills. Five model inputs were used: i) the windward slope of the hill, ii) the roughness length of the ground, iii) the hill type (single or multiple), iv) the distance between the hills (when multiple are present), and v) the height of interest above the hill. NN output is the fractional speed-up ratio, which is the ratio of the wind speed over the hill to the wind speed at the same height above the ground, if the hill were not present. Training was conducted using CFD generated data which used a k- ε turbulence model. The intention was to make the NN model available to the end user, who can then make predictions of speed-up without dealing with complex numerical simulations. This is very similar to the objective here, as discussed in Chapter 1. Bitsuamlak et al. [36] found that NN predictions of speed up over hills compared well with an

independent set of experimental data, including predictions made for new cases. This study is similar to the current project; both studies attempt to predict the effect of a nearby feature on the wind speed. The success of Bitsuamlak et al. [36] increases confidence in the NN-based approach.

Kariniotakis et al. [37] developed a recurrent NN model to forecast the near future power output of two wind parks. The wind parks are part of a wind-diesel power system on an isolated island. The installed diesel capacity is 13.25 MW, and the total wind capacity is 1.14 MW. The NN model was used for an on-line application, to predict the power output of the wind parks based on recent wind speed and power output. Accurate near term wind power output forecasts enable better performance of the wind/diesel system. The model was implemented for on-line use in the control system of the wind/diesel power system for a 5 day period. This resulted in a decrease of 30% in the number of starts/stops of the diesel units, a decrease in the loss of load events, an increase in fuel savings of 1-2% for this limited period, and higher utilization of the available wind energy. While this application of NNs is obviously different than that pursued in the current study, it illustrates how NNs can identify complex relationships between variables which can then be incorporated into a practical model.

Zhang et al. [38] developed a NN-based model which can predict how the wind loads on a building are influenced by the presence of a second building nearby. The two buildings are assumed to have identical footprints. Four model inputs were used: the space between the two buildings in the x and z directions, the ratio of building heights, and the local surface roughness. The output of the NN is the interference factor, which is defined as the ratio of the load on the objective building when the second building is present to the load when no other buildings are present. A total of 106 data points were available, taken from a variety of experimental sources. 80% of the data was used as training data, while the remaining 20% was used for validation. It was found that the NN was able to predict the interference factor with good accuracy. This study is similar to the current study in that the effect of a building on the wind is estimated. In the study

of Zhang et al. [38], the effect is predicted indirectly, through a prediction of the increase or decrease in load on a building caused by the wind. In the current study, the effect on the wind is directly predicted, which could be used to predict how the presence of an upwind building affects the load on a downwind structure.

3.0 Overview of wakeNET Model

Figure 3.1 is an overview of the proposed NN-based wake model. There are two types of model inputs: those describing the obstacle, and those defining the point of interest, at which the wind is to be predicted by the model.

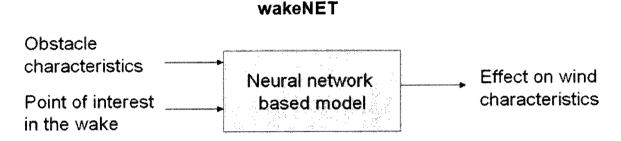


Figure 3.1 - Overview of proposed NN-based model

3.1 Inputs

Several factors which affect the extents and magnitude of a wake can be identified from the review of bluff body studies in Chapter 2. This information will be used to determine model inputs. The desired simplicity of the model must also be kept in mind; all model inputs should be easily measured or otherwise obtainable by a potential small turbine owner.

Model inputs should be non-dimensionalized. In almost all past wake studies examined, geometric values are non-dimensionalized by the height of the obstacle, h. This approach is followed here. One implication of this is that wake predictions are independent of scale and Re, which is an essential assumption when applying wind tunnel results to a full scale case. For practical purposes, the assumption is valid, as long as the Re of the flow exceeds the critical value as discussed in Section 2.4.4.

From the studies by Hansen et al. [24] and Martinuzzi and Tropea [25], it is apparent that the AR of the obstacle has a major influence on its wake. As described in Equation 2.9, the AR of an obstacle is its width normalized by height. Obstacle AR is a very important model input.

The effect of an obstacle's PR on the wake region is much less studied than the effect of AR. Compared to AR, it is thought that PR has a smaller but still significant effect on the wake of an obstacle in the ABL. For example, it is known that obstacle depth will determine whether or not the flow reattaches to the top of the obstacle, or to the ground further downwind [19]. PR was selected as a model input. Many buildings do not have a rectangular footprint. In these cases, it is recommended that the AR and PR are chosen based on the extreme limits of the footprint, such that the entire building is inside the rectangular area.

Hansen et al. [24] show that the orientation angle of the model a with respect to wind direction is very important as well. At each unique a value, a different geometry is presented to the wind. Model orientation is another major factor that will affect the wake, and is an important input to the new model.

One way in which Hunt and Smith [32] were able to improve upon previous models was by taking into consideration the overturning moment of the wind on the obstacle. This is related to the drag force of the obstacle in the wind; greater drag will increase the momentum deficit in the flow, which causes stronger and more widespread wake effects. Taylor and Salmon [30] used base moment coefficient as an input for their model. This was considered as a potential input for the new wakeNET model. Although it would be very difficult for the average homeowner to measure the moment, it could be estimated based on the shape of the building. Alternatively, features which define the shape of the building could be used as model inputs. Examples of these include roof angle (*RA*), the difference between peak and non peak height, or sizes of other features present on the roof such as chimneys. In this way, the wake moment can be taken into account, albeit indirectly.

Because RA can easily be estimated, and because most buildings have roofs of comparable shape, it was decided that it should be used as an input. The definition of RA is shown in Figure 3.2. Although the use of overturning moment is promising, it is felt that RA is better suited as an input, mainly because it is easier to determine. Potentially, for buildings with roof shapes other

than that seen in Figure 3.2, the roof angle input value could be replaced by a 'peak' angle value, based on the peak height and the lowest roof height. However, model prediction accuracy would be expected to decrease because of this substitution. Although not considered in this thesis, further inputs related to the shape of the roof and the overturning moment could be used to expand the scope of the model.

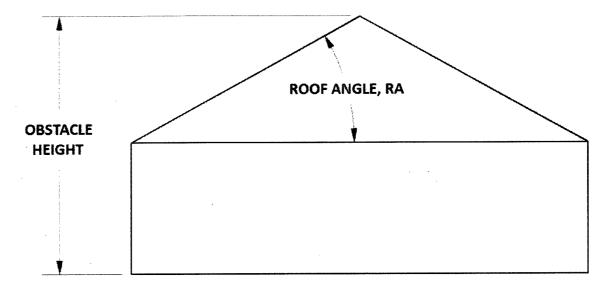


Figure 3.2 – Definition of building roof angle

It should be mentioned that a change in a will also change the projected AR, PR, and RA presented to the flow. For each obstacle, these three model inputs are constant, defined by their values at a specific model orientation: when the front face of the model is oriented normal to the flow direction ($a = 0^{\circ}$). Furthermore, the front face of the obstacle is always defined as the face that is parallel to the peak of the roof. When RA is 0° , any obstacle face can be defined as the front.

It is known that flow around a bluff body is dependent on upwind flow characteristics [29]. Characteristics such as shear coefficient and surface roughness could be incorporated as model inputs; the inclusion of these inputs may improve the accuracy of model predictions. However, this model does not incorporate any inputs related to the upwind flow, for several reasons. Characteristics of the incoming wind at a site are not constant; they will change with time of day,

season, and weather. As with base moment coefficient, it would be very difficult and perhaps expensive for a potential turbine owner to accurately estimate the mean upwind flow characteristics at their site. It was decided that the upwind flow would be fixed as a fully turbulent atmospheric boundary layer typical of a semi-rural region, as per [28]. As mentioned, Lim et al. [29] state that upwind flow characteristics affect the flow *around* a bluff body, but it is assumed here that the effect on flow in the wake region will be small. This is investigated in Chapter 4.

Similarly, Peterka et al. [19] and Lemberg [13] discussed the importance of the ratio of building height to boundary layer thickness, h/δ . As proposed by Counihan [26], it is thought that as long as this ratio is kept small, any changes will be negligible.

3.2 Outputs

The majority of uncertainty in small turbine micrositing is related to knowledge of the local wind field [14]. As discussed previously, the power output of a wind turbine is highly dependent on the speed of the wind. wakeNET was developed to predict how the actual wind speed in the wake relates to the hypothetical wind speed at the same point, over the same time, if the obstacle was not present. These two quantities are referred to as the sheltered and unsheltered speeds, respectively. Equation 3.1 defines the velocity ratio R_{ν} as the ratio of the mean sheltered wind speed V_s to the mean unsheltered wind speed V_u .

$$R_V = \frac{V_s}{V_u} \tag{3.1}$$

Based on R_V values at two points, the degree of wind shear in the wake can also be estimated. Another useful term related to the velocity ratio is the velocity deficit, which is defined in Equation 3.2 as the fractional decrease in wind speed at a sheltered position in the wake.

$$D_{V} = 1 - \frac{V_{s}}{V_{c}} = 1 - R_{V} \tag{3.2}$$

Equation 3.3 defines the power density ratio R_p as the ratio of wind power density at a point in the wake to the hypothetical unsheltered wind power density at the same point, over the same time. Equation 3.3 is based on Equation 2.2, which shows that the power density of the wind is proportional to the wind speed to the third power.

$$R_{P} = \frac{P_{s}}{P_{v}} = \frac{V_{s}^{3}}{V_{v}^{3}} = R_{V}^{3} \tag{3.3}$$

Similar to the velocity deficit, the power density deficit D_p is defined in Equation 3.4 as the fractional decrease in power density at a sheltered position in the wake.

$$D_{P} = 1 - \frac{P_{s}}{P_{u}} = 1 - R_{P} \tag{3.4}$$

The effects of turbulence on a wind turbine were briefly discussed in Chapter 1. Quantitative predictions of turbulence effects on the power output of a turbine are beyond the scope of this thesis. However, the new model will predict how turbulence intensity levels in the wake relate to unsheltered turbulence intensity levels. Equation 3.5 defines the turbulence intensity ratio R_I as the ratio of sheltered turbulence intensity I_S to the hypothetical unsheltered turbulence intensity I_U at the same point, over the same time period.

$$R_I = \frac{I_s}{I_u} \tag{3.5}$$

The turbulence intensity excess is defined in Equation 3.6 as the fractional increase in turbulence intensity at a sheltered position in the wake.

$$E_{I} = \frac{E_{s}}{E_{u}} - 1 = R_{I} - 1 \tag{3.6}$$

wakeNET will predict values of R_V and R_I at any point in the obstacle's region of influence. From these two values, all other quantities defined in this section can be calculated.

3.3 Source of Training Data

A NN will learn the relationship between inputs and outputs from the training data, as described in Chapter 2. All wakeNET training data was obtained in the University of Guelph BLWT; reference results were not used as training data. The use of wind tunnel data is essential here for practical reasons. To characterize a wake, it is necessary to measure the flow at a large number of points. This can be done using thermal anemometry in a wind tunnel much more easily than in a field test using meteorological instruments. In the wind tunnel, hot film probes can be moved around easily using the traversing system, allowing measurements at hundreds of points in a wake. In the field, wind properties will only be known at a few points in the wake (corresponding to anemometer locations, which are fixed). To measure a full wake in the field, a very larger number of sensors and towers would be needed. As well, due to the intermittency and non-stationarity of wind, it is necessary to take measurements in the field for at least several weeks before reasonably certain relative mean wind speeds can be calculated between measured points. In the wind tunnel, the flow is much more consistent and controlled, so the spatial variation of the flow field can be measured in a much shorter amount of time. The obvious downside to using wind tunnel measurements to train the NNs is that the wind tunnel is only a simulation of real-world conditions. Wind tunnel results need to be validated; this was the purpose of the field experiment, described in Chapter 5.

Ideally, all NN training data would be based on the measured power output of an actual turbine in the wake of an obstacle; however, this would limit wakeNET to that specific model of turbine. As well, it would be very difficult to obtain enough training data of this form to create an accurate model. Instead, a procedure has been developed in which the power output of a turbine can be estimated based on a predicted R_V value. This is described in the next section.

3.4 Implementation

This section briefly explains how wakeNET can be used to predict the mean power output of a sheltered wind turbine. A case study which shows an example of this calculation is included as Appendix A. Required information includes i) local wind conditions, taken from a nearby meteorological tower, or a wind map such as the Ontario Wind Atlas [39] ii) the turbine's power curve, which predicts turbine power output at a given wind speed, and iii) the size, shape, and relative location of all nearby obstacles.

The procedure described below assumes the point of interest is specified and fixed. However, the calculation can be repeated for any number of points, if the goal is obtain a map of local sheltering effects. A well-developed atmospheric boundary layer (ABL) is required for the models to be valid, which means that they are only applicable in open, rural areas, as opposed to urban regions with dense buildings.

Since the degree of sheltering will depend greatly on wind direction, wakeNET is used to predict R_V and R_I at the potential turbine location for a range of wind directions, for each obstacle. For each wind direction, the sheltered distribution of wind speed can be predicted from R_V and the unsheltered distribution at the site. The mean power output of the turbine can then be estimated as the mean of the turbine's power curve, weighted by the frequency of each wind speed. An estimate of R_P for each wind direction is obtained by calculating the mean power output using both the sheltered and unsheltered wind speed distributions.

The wind rose describes the distribution of wind direction at the site. The overall mean power output of the turbine is the mean of the output for each wind direction, weighted by the frequency of wind from that direction, as found in the wind rose. Overall estimates of R_V , R_I , and R_P can be obtained in the same way.

4.0 Wind Tunnel Experimentation

This project involved extensive wind tunnel testing, the main purpose of which was to collect training and validation data for the model. From this data, a great deal can be learned about the effect of obstacle characteristics on wake structure. The flow was measured around many model obstacles in a simulated ABL, in the University of Guelph BLWT. Results for common obstacles were compared to reference data. Select figures are included in this section to illustrate wake features of interest. Additional wind tunnel results are included in Chapters 5 and 6, where comparisons are made to field measurements and model predictions, respectively.

4.1 Equipment and Set Up

The University of Guelph Engineering BLWT is an open circuit wind tunnel, 9.7 m (32.0 ft) long, with a square cross section measuring 1.2 m x 1.2 m (4.0 ft by 4.0 ft). A diagram of the wind tunnel is shown in Figure 5.1. All velocity measurements were taken using one dimensional TSI-1210 hot film anemometers, sampling at 1000 Hz. The sensing length of the hot film probe is 0.51 mm [40] (1% of obstacle height). Prior to the experiment, each hot film probe was calibrated using a TSI automatic calibrator. Calibration curves for each probe are included in Appendix B. In this thesis, the term 'wind tunnel measurements' is often used. It refers to wind speeds which are calculated from voltage measurements taken by the data acquisition system. The voltage measurements are converted into wind speed values using the calibration curves. An uncertainty analysis was conducted following the methods of Coleman and Steele [41], and is included in detail in Appendix F. Using 95% confidence intervals, the uncertainties of \bar{V} , V_{rms} , and I are estimated to be 0.5%, 1.7%, and 1.8%, respectively. This is not considering effects associated with unsteadiness in the flow. Such effects are not technically errors, but they will significantly affect the uncertainty of R_{V} and R_{I} values. Estimates of the uncertainties of these ratios are given in Section 4.3.

The BLWT is equipped with a ceiling-mounted custom-built traversing system which enables controlled probe positioning in three dimensions. The hot film probe is mounted on the probe arm. Its position is adjusted in the x, y, and z directions using three manually controlled electric motors. Probe position is tracked in the x and z directions based on grid points on the wind tunnel floor. A ruler is used to measure probe height y. Assuming that one half the least division is a reasonable estimate for a 95% confidence interval, positioning accuracy in each direction is estimated to be \pm 0.5 mm.

Measurements were taken in two distinct downwind sections of the wind tunnel. The reason for this is described in Section 4.3. The first probe was located in the test section, on the traverser. Its purpose was to measure the flow at the point of interest, which could be sheltered or unsheltered. The second probe (the reference) was situated at a fixed location 3.79 m from the back of the tunnel, such that it would always measure undisturbed flow. This set up is illustrated in Figure 4.1.

The obstacle models were constructed from pine wood in the shop, using either wood glue or screws to fasten model segments together. All models had sharp edges and rough surfaces. Model dimensions are generally accurate to within 0.5 mm. Table 4.1 summarizes the unique obstacles used for tests in this study. Obstacle name refers to the shorthand used to describe the obstacle. Category refers to the main use of measurements made in the obstacle's wake. There are three categories of obstacles. The first category, 'training', is for those obstacles used to generate training data. The second category, 'comparison', is for those obstacles that were built for wind tunnel simulations of the field experiments, discussed in Chapter 5. Also in this second category are obstacles mainly used to obtain results for comparison against results from the literature; these results were used as training data as well. The third category, 'validation', is for the three obstacles that were built for the sole purpose of obtaining validation data; no measurements made in the wakes of these obstacles were used as training data. The three validation obstacles were

created solely to evaluate the model's accuracy for previously unseen obstacles; this is discussed in detail in Chapter 6.

Table 4.1 - Summary of obstacles used in the wind tunnel

Obstacle Name	Obstacle number	Category	AR	PR	RA	h (mm)
0.5-1 block	1	Training	0.5	1	0°	50
Cube	2	Training,	1	1	0°	100
		Comparison				1
2-1 block	3	Training	2	1	0°	50
2-1-15 block	4	Training	2	1	15°	50
2-1-30 block	5	Training	2	1	30°	50
2-1-45 block	6	Training	2	1	45°	50
3-1 block	7	Validation	3	1	0°	50
3-2-15 block	8	Validation	3	2	15°	50
4-1 block	9	Training	4	1	0°	53
4-2 block	10	Training	4	2.74	0°	50
5-1-36 block	11	Validation	4.81	0.85	36°	52
6-1 block	12	Training	6	1	0°	50
9-1 block	13	Training	9	1	0°	50
Two-dimensional	14	Training,	24	0.04	0°	50
wall		Comparison				
Large Wall	15	Comparison	2.07	0.04	0°	100
Small Wall	16	Comparison	1.03	0.04	0°	100
Trailer block	17	Comparison	4.73	0.83	0°	50
Hansen block	18	Comparison	2.44	0.75	0	50

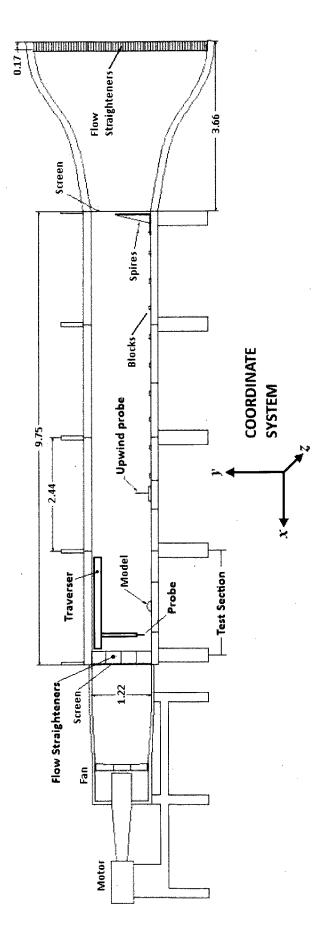


Figure 4.1 - Diagram of the wind tunnel. Dimensions are in m.

Models were secured in place in the wind tunnel using a dowel joint. Each model (except for the thin wall) had a hole drilled into the bottom, at the center of the model, to a depth of roughly 35 mm (such that the hole did not go all the way through the model). A steel dowel pin was used to centre the model above a corresponding hole inside the wind tunnel. A model could be rotated about this dowel pin to obtain variation in orientation angle while the center of the obstacle stayed fixed. This was important because the centre of the obstacle is the origin of the coordinate system used to define position in the wake.

4.2 Simulation of the ABL

It is necessary to simulate the ABL as accurately as possible in the wind tunnel, since the incoming (or 'upstream') flow seen by the model should be similar to the incoming flow seen by an actual obstacle in the wind. Snyder [28] provides guidelines regarding the main features of the steady state adiabatic neutrally stable boundary layer. Ideally, the simulated boundary layer would perfectly match the actual ABL when considering many flow characteristics, including relative velocity profiles, turbulence intensity profiles, turbulent energy spectra, turbulent length scales, and ratio of obstacle height to boundary layer thickness, among others. In reality, it is extremely difficult to achieve similarity of all these flow characteristics, and there are always compromises made between the various competing criteria [29]. Here, attempts are focused on matching the velocity profile, turbulence intensity profile, and the turbulent energy spectrum of the simulated ABL layer to those of a reference ABL. The reference boundary layer characteristics depend on the upwind surface roughness and conceivably, this could be used as a model input. However, as discussed in Chapter 3, it would be difficult for the eventual users of this model to accurately define the surface roughness in the area where the small wind turbine is to be installed. As well it is thought that upwind surface roughness will not have a significant effect on wake properties, over the surface roughness range of interest, which is mainly rural open to semi-open terrain.

A thick turbulent boundary layer was created using techniques commonly employed in BLWT studies (for example, see [13][26][23][28]). A mesh screen is located at the front of the wind tunnel, covering the entire cross section. Immediately behind the screen are three triangular spires that extend to approximately 2/3 of the tunnel height. Rows of four evenly distributed small wooden blocks (14 cm long by 8 cm wide by 2 cm high), spaced at 30 cm (1 ft) intervals, were arrayed on the floor of the tunnel to simulate the surface roughness of a rural area. The rows of wooden blocks extend from the tunnel inlet to roughly 4 m in front of the model location. From this point onwards, the BLWT floor is covered with rough plastic paneling, originally intended for diffusing light in fluorescent fixtures, with a roughness element height of 2 mm.

Measurements were taken for a wide variety of configurations of blocks and spires. The configuration described above was found to most closely simulate the atmospheric ABL seen in a rural area, as described by [18] [28][42]. This configuration was used for all tests. Figure 4.2 shows measurements made in the undisturbed boundary layer in the wind tunnel compared to reference values. Undisturbed field measurements are also shown, scaled to the wind tunnel; field experimentation is described in detail in Chapter 5.

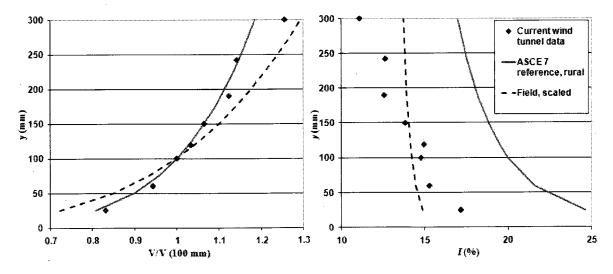


Figure 4.2 – Comparison of wind tunnel unsheltered profiles to reference profiles for a rural area. a) Shows mean velocity profiles, including a power law fit derived from measurements taken at the field site. b) Shows mean turbulence intensity profiles.

The undisturbed velocity profile in the wind tunnel agrees fairly well with the ASCE 7 reference velocity curve [18]. The undisturbed turbulence intensity profile does not match well with the ASCE 7 reference profile; however, the two curves show similar trends, and both curves show large turbulence intensity values. It was found that turbulence intensity could be increased by adding an additional spire, but when this was done, the boundary layer was highly non-uniform in the lateral direction, at the test section. It was decided that the three spire configuration was preferable, and satisfactory. A report by Ziter [43] describes how different configurations of roughness generating elements affect velocity and turbulence intensity profiles in the test section of the Guelph wind tunnel. The current configuration was determined based on this report, as well as a study (included as Appendix C) into the extent to which the flow in the test section is fully developed, and uniform in the lateral direction.

Figure 4.3 shows the unsheltered power spectrum in the wind tunnel compared to the reference, which is the von Kármán spectrum, as reported by Burton et al. [42]. n is the frequency, z is the height at which the velocity was measured, and U is the mean wind speed at that height. For details regarding normalization of the spectra, see [42]. The maximum frequency shown is 500 Hz, which is half the sampling frequency of the hot film probe. At higher frequencies, the measured curve has a lower magnitude than the reference curve, while the opposite is true at lower frequencies. Both curves follow the same trend, peaking near the same frequency. The measured wind tunnel spectrum is an acceptable representation of the reference wind tunnel spectrum.

Questions have been raised as to the necessity of simulating the ratio of obstacle height h to boundary layer thickness δ in the wind tunnel. In the range of h/δ explored by Lemberg [13], this ratio did not have an effect on the rate of decay of maximum velocity deficit in the wake. Hansen et al. [24] found that although the wake decay rate is independent of h/δ , the magnitude of the initial disturbance did appear to depend on this ratio. However, this effect is only evident for the largest obstacle, in which the wake was impinging on the walls of the wind tunnel. They suggest

that when h/δ is small, it is not a significant factor. This concurs with the criteria proposed by Counihan et al. [26], who state that in BLWT experiments, the boundary layer thickness should be much greater than the obstacle height. In this thesis, it is assumed that as long as the ratio of obstacle height to boundary layer thickness is kept small, changes in its value will not significantly affect the wake; order of magnitude increases would be required to see any effects. The wind tunnel simulation criteria specified by Counihan et al.[26] are followed, which state that $k \ll h \ll \delta$, where k is the height of roughness elements (recall that k is the obstacle height and δ is the boundary layer thickness). Here, k, k, and δ have values of 3 mm, 50 mm, and roughly 400 mm, respectively, in the downwind half of the tunnel.

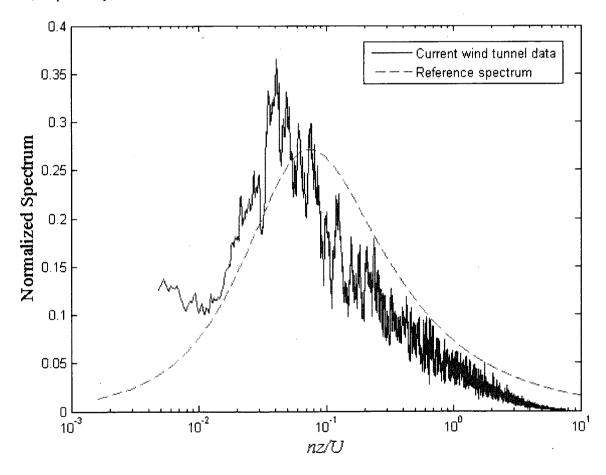


Figure 4.3 – Comparison of unsheltered turbulent power spectra in the wind tunnel to the reference curve [42]

In Musselman's BLWT experiments [23], lateral turbulence scales in the wind tunnel were not large enough to model the low frequency meandering found in the natural environment. Since in this experiment, all wind tunnel measurements were made with a one-dimensional hot film probe, lateral turbulent scales were not measured here. Based on similarities between the set ups of the two experiments, it is assumed that the low frequency meandering described by Musselman was not simulated here either. However, this should not have a significant effect on the validity of the wind tunnel simulation, since turbulence at the scale of the characteristic building dimension will be dominant in the wake [23].

4.3 Testing Procedure

Before testing, the optimal sampling period was determined. Three 40 minute samples were taken in the wind tunnel, and moving averages were calculated using a range of sampling times (from 8 seconds to 256 seconds). The optimal sampling time was determined to be 32.768 seconds (see Appendix D for the detailed calculation). This takes into account the additional time in the facility that would be required to complete the tests if a longer sampling time was used, and the increased variability (scatter) in the data that was present when shorter sampling times were used, due to natural variation of wind speed in the tunnel. 32.768 seconds was arrived at by specifying that 32 kilopoints (32 x 2¹⁰ points) should be measured, at a frequency of 1000 Hz. Even with an averaging period of 256 seconds, the average values returned were up to 2% different from the 40 minute average. It is thought that this was due to small variations in the output of the motor powering the wind tunnel's fan, causing the freestream wind speed to vary (it was generally around 9.3 m/s). The second, upwind hot film probe was used to compensate for these small but important variations in test section free stream velocity and turbulence intensity. All mean velocity and turbulence intensity measurements made in the test section were normalized by the reference measurements, as recorded by the upwind probe. Measurements were only made away from the side walls, in the centre half of the tunnel. Obstacles were also only

located in the centre half, to reduce or eliminate wall effects (the one exception to this was the two-dimensional wall, which spanned the tunnel). The boundary layer thickness along the walls and roof was estimated at roughly 20 cm, based on the measured boundary layer thickness above the floor when no roughness elements or spires were in place.

A careful testing procedure was followed when obtaining wind tunnel measurements. The following explanation describes the general process of obtaining R_V and R_I . Using the traversing system, the hot film probe was moved to the location of interest. The flow in the wind tunnel at both probe locations was measured for the sampling period. From this data sample, the mean flow speed and turbulence intensity were calculated for both sensor locations. R_{VI} was calculated as the ratio of the mean unsheltered wind speed at the point of interest, \overline{V}_I , to the mean wind speed at the reference location over the same time period, \overline{V}_{0I} , as shown in Equation 4.1. Equation 4.2 is analogous to Equation 4.1, and defines R_{II} as the ratio of the unsheltered turbulence intensity at the point of interest to the turbulence intensity at the reference point, over the same time period.

$$R_{V1} = \frac{\overline{V_1}}{\overline{V_{01}}} \tag{4.1}$$

$$R_{I1} = \frac{I_1}{I_{21}} \tag{4.2}$$

Once these two quantities were obtained, the obstacle was put in place using the dowel pin. The sheltered flow was then measured for the same sampling time, at the same point, and the sheltered mean wind speed $\overline{V_2}$ and turbulence intensity I_2 were calculated. $\overline{V_{02}}$, and I_{02} , the reference mean wind speed and turbulence intensity, were calculated for the second time period. R_{V2} and R_{I2} could then be found, as defined by Equations 4.3 and 4.4, respectively.

$$R_{V2} = \frac{\overline{V_2}}{\overline{V}_{02}} \tag{4.3}$$

$$R_{I2} = \frac{I_2}{I_{02}} \tag{4.4}$$

The desired output ratios at that point, R_V and R_h could then be calculated, as seen in Equations 4.5 and 4.6.

$$R_{V} = \frac{R_{V2}}{R_{V1}} \tag{4.5}$$

$$R_{I} = \frac{R_{I2}}{R_{I1}} \tag{4.6}$$

 R_V is essentially the velocity normalized twice, since it is normalized by measurements made at the reference point over each sample time, and then the sheltered measurement is normalized by the unsheltered measurement. R_I can be thought of as the thrice normalized rms velocity, since turbulence intensity is itself a normalized quantity. Appendix F describes how the uncertainty in \overline{V} and V_{rms} propagates through the calculation of R_V and R_I . The uncertainties of R_V and R_I are estimated to be 2.9% and 9.3%, using 95% confidence intervals. A large part of these uncertainties is related to the unsteadiness of the wind speed in the tunnel. When R_V and R_I are found without normalizing by the upwind probe, their uncertainties are estimated to be 4.7% and 10.3%. Again, the main uncertainty component is due to unsteadiness in the tunnel, which is significantly reduced when the upwind probe is used as a reference.

In practice, each sheltered measurement was not directly preceded by an unsheltered measurement. Rather, a full unsheltered vertical profile was measured first, followed by a full sheltered profile. This was done in the interest of time, and to eliminate the need to constantly open and close the wind tunnel door to put the model in place. Although the undisturbed boundary layer showed a high degree of uniformity in the lateral direction, it was not uniform enough to eliminate the need to take an unsheltered profile at each lateral location. The magnitude of lateral non-uniformity was generally around 1%, although at some points it was greater. Uniformity of the flow in the test section is described in Appendix C. Similarly, the flow in the test section was nearly but not quite fully developed, meaning that it was necessary to measure unique unsheltered profiles at each x location. Often, an unsheltered profile would be measured at

the (x, z) location of interest, followed by multiple sheltered profiles at the same location, each with a unique obstacle or model orientation. Since unsheltered measurements were not affected by the obstacle, by definition, the same unsheltered measurement could be used many times, as long as the corresponding sheltered measurement was taken at the same (x, y, z) location. This was essential in reducing the total number of measurements required to characterize a wake, since it greatly reduced the number of unsheltered measurements needed. To maintain consistency, sheltered and unsheltered profiles were taken without changing the wind tunnel speed. To avoid potential anemometer drift, the length of time between measuring a sheltered and unsheltered profile did not exceed roughly two hours, and was typically much less.

4.4 Summary of Tests Performed

The numbers of measurements made to characterize the flow for each obstacle are shown in Table 4.2. The indicated number of measurements covered a wide range of downwind distances, lateral positions, vertical positions, and model orientations. Some models were used more than others depending on their purpose, as described in Table 4.1. In total, 4473 unique R_V and R_I values were obtained. Also shown in Table 4.2 are the numbers of profiles measured for each obstacle. Most of these measurements were taken in the form of vertical profiles, of which 517 were measured in total. Typically, each vertical profile consisted of 8 points, although this varied depending on the obstacle. For example, because the wake of the 9-1 block extended to a greater height than the wakes of most other obstacles, several of the vertical profiles in its wake consisted of 10 points instead of 8. A small number of horizontal profiles were also taken. Recall that three of the models (the large wall, small wall, and trailer block) were only used to simulate the field experiment in the wind tunnel. Measurements were not taken in the form of vertical profiles for these obstacles; only sensor locations were measured.

Table 4.2 – Summary of the measurements made to characterize the flow for each obstacle

Obstacle	Number of measured points	Number of Profiles	
0.5-1 block	328.	41	
Cube	632	79.	
2-1 block	584	73	
2-1-15 block	330	41	
2-1-30 block	330	41	
2-1-45 block	330	41	
3-1 block	106	. 12	
3-2-15 block	56	. 7.	
4-1 block	669	83	
4-2 block	306	38	
5-1-36 block	149	15	
6-1 block	70	7	
9-1 block	268	28	
Two-dimensional wall	56	7	
Large Wall	60	NA	
Small Wall	60	NA	
Trailer block	95	NA	
Hansen block	44	4	
Total	4473	517	

4.5 Results

Results presented in this section were selected to show how the current wind tunnel simulation compares to references, and to illustrate several main points. More wind tunnel results are included in Chapters 5 and 6.

4.5.1 Reynolds Number Dependence

A common and useful definition of Re is based on the height of the model and the upwind flow speed at model height, as defined in Equation 2.11. Several different model heights were used here. Based on a height of 50 mm (the most common height, as well as the shortest), and the mean incoming wind speed at 50 mm, the Re of the flow was $2.5 \cdot 10^4$. This is inside the critical range of 2 to $3 \cdot 10^4$ [28] specified by Snyder [28].

A series of tests was carried out to measure the flow in the wake of the cube (h = 100 mm) at a range of wind speeds, to determine the effect of Re. Select results are included as Appendix E. It was found that unsheltered, normalized mean velocity and turbulence intensity profiles were very consistent when the mean wind speed was 4.0 m/s or greater at a height of 100 mm. In the wake of the cube, sheltered mean velocity and turbulence intensity profiles showed little Re dependence above a Re of roughly $1.8 \cdot 10^4$. In general, turbulence intensity measurements showed more scatter, although this was true for all wind tunnel tests and may not be a Re effect. Similar results were obtained when the front cube face was normal to the flow and at an azimuth of 45° to the flow.

Based on these results, and comments in the literature, it is assumed that wind tunnel measurements are independent of Re above a value of roughly $2 \cdot 10^4$. Any Re dependence is expected to be most obvious at lower Re ranges [29]; since none was evident over the upper end of the range studied, it is assumed that the effect of further increases to Re would also not be significant. Additional investigation into any possible dependency on Re was conducted by comparing wind tunnel results to field experiment data (see Chapter 5).

4.5.2 Comparison to Reference Results

In this section, wind tunnel results from the current study are compared to those of Lemberg [13], Counihan (as reported by Lemberg [13]), and Perera [27]. Predictions made by Taylor and Salmon's shelter model [30] and Perera's model [27] are also shown. Both of these models are described in Chapter 2. Further comparisons of current wind tunnel results, predictions from existing models, wakeNET predictions, and reference results (specifically, those of Hansen et al. [24]) are included in Section 6.4, as part of the validation of wakeNET. It should be noted that the reference results were all obtained from similar but not identical experiments. Table 4.3 summarizes the main differences between the tests performed here and the reference tests. None of the parameters described in Table 4.3 are used as inputs to the new model, as explained in Chapter 3. Re is defined in Equation 2.11. $U\infty$ is the freestream wind speed, which is the speed of air in the wind tunnel above the boundary layer. It was assumed that variations in the values of the five parameters in Table 4.3 would not significantly affect the wake over the ranges of interest. However, as a result of these differences, as well as the experimental uncertainties described previously in this chapter, perfect agreement between current and reference results is not expected.

Table 4.3 -Main differences between the current and reference experiments

Parameter	Current	Perera [27]	Lemberg [13]	Hansen et al. [24]
Re	2.5·10 ⁴	2.1·10 ⁴	10 ⁵	4.2·10 ⁴
h	50 mm	40 mm	102 mm	65 mm
h/δ	0.125	0.16	0.167	0.11
$U\infty$	9.3 m/s	9.1 m/s	15.3 m/s	16.2 m/s
α	0.14	0.15	0.15	0.25
I(h)	15%	20%	10%	20%

Figure 4.4 shows how R_v varies with y in the wake of a two-dimensional wall, at x = 10. Recall that all coordinates are normalized by h, unless otherwise specified. Wind tunnel measurements from the current study are compared to Perera's wind tunnel data, Perera's model predictions, and Taylor and Salmon's model predictions. Perera's measured data compares fairly well with measurements made here. Taylor and Salmon's model agrees very strongly with Perera's, which can be explained by considering that the vertical similarity profile specified by Taylor and Salmon is based on Perera's empirical formula for two-dimensional obstacles. Current wind tunnel measurements showed slight velocity excesses at the three highest points, which may be related to blockage effects. The two-dimensional wall was the largest obstacle by far, in terms of blockage in the wind tunnel. 4.2% of the cross sectional area was obstructed by the two-dimensional wall, which is acceptable according to the criteria specified by Snyder [28] (< 5%), but may still cause a small undesirable speed up effect.

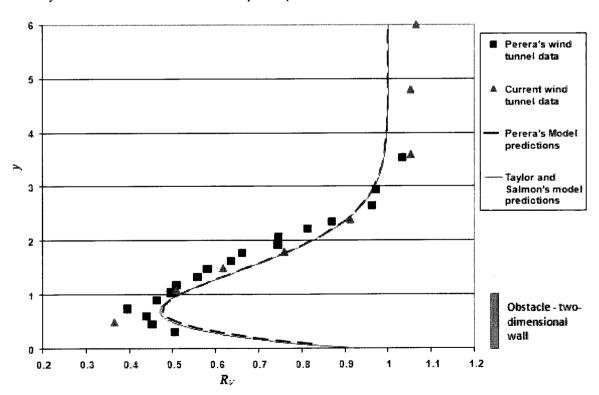


Figure 4.4 – Vertical R_V profiles in the wake of a two-dimensional wall, at x = 10

Figure 4.5 shows how R_l varies with y in the wake of a two-dimensional wall. Data from the current study follows a trend similar to Perera's data and model, although the two data sets appear to diverge greatly at y positions of less than 1.5. Perera's relation does not make accurate predictions when y < 1.25.

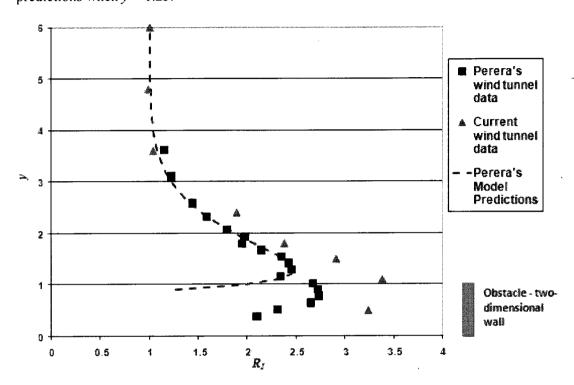


Figure 4.5 – Vertical R_I profiles in the wake of a two-dimensional wall, at x = 10

Figure 4.6 contains R_V profiles in the wake of a cube at x = 4.53, z = 0, with $a = 0^\circ$. Current wind tunnel results agreed very well with those of Counihan, and fairly well with those of Lemberg, with the greatest differences occurring at the lowest three heights. Predictions made by Taylor and Salmon's model agree well with the data. Perera's model greatly over predicts the velocity deficit in the wake of the cube, which was expected, based on the description by Taylor and Salmon [30] and the WAsP technical manual [1].

Figure 4.7 shows results for the vertical R_V profile at x = 6.84, z = 0, with $a = 45^\circ$. Results from the current study are somewhat different from those of Lemberg. This may be due to the greater upwind turbulence intensity that was used here; Lemberg's unsheltered turbulence intensity values were roughly half of those measured in this study. It is thought that greater levels

of turbulence increase the mixing of momentum, reducing the extent of the velocity wake. Again, Perera's model predicts much greater wake effects than were measured. Taylor and Salmon's model significantly over predicts the velocity deficit in the wake, compared to current wind tunnel results and those of Lemberg. In Taylor and Salmon's model, the obstacle is essentially replaced by its frontal area projected towards the wind. Since a cube at 45° degrees is effectively wider than a cube normal to the flow, the frontal area is bigger. All else being equal, Taylor and Salmon's model will predict greater velocity deficits in the wake of a cube with $a = 45^{\circ}$ than in the wake of a cube with $a = 0^{\circ}$. However, wind tunnel results show that the specific geometry of the obstacle is important, such as the angles at which the front faces meet the flow.

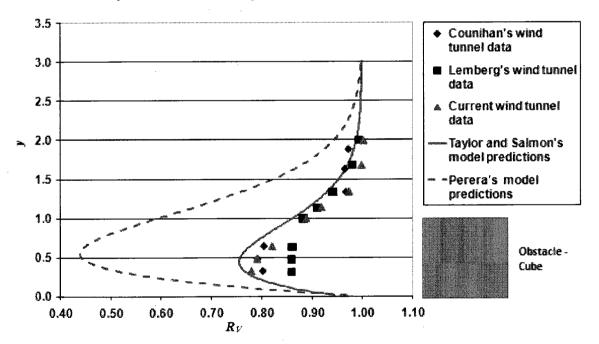


Figure 4.6 – Vertical R_V profiles in the wake of a cube at x = 4.53, z = 0, with $a = 0^\circ$.

4.5.3 Wakes of Very Wide Obstacles

As discussed in Chapter 2, Martinuzzi and Tropea [25] investigated the flow around blocks of varying AR in channel flow. They found that for blocks with AR greater than 6, the centre region of the wake was essentially the same as the wake of a two-dimensional fence. This is an important result when predicting wind characteristics in the wakes of obstacles with large AR.

Figure 4.8 shows the measured lateral R_{ν} profile in the wake of the 9-1 block at x = 7.17, y = 0.94. Also shown are predictions made by Taylor and Salmon's model [30] and Perera's model [27]. From the wind tunnel data, it is evident that the velocity ratio in the wake continually decreases as the lateral distance from the edge of the obstacle increases. Even near the centre plane, 4.5 h from the lateral edge of the obstacle, the flow varies with z. Taylor and Salmon's model predicts that significant edge effects will be present up to roughly four heights from the edge of the obstacle, after which the velocity deficit is constant. This results in poor model predictions for the centre region of the wake. Based on Figure 4.8, it appears that Martinuzzi and Tropea's results for channel flow cannot be applied to an obstacle in a turbulent boundary layer due to the different characteristics of the two flows.

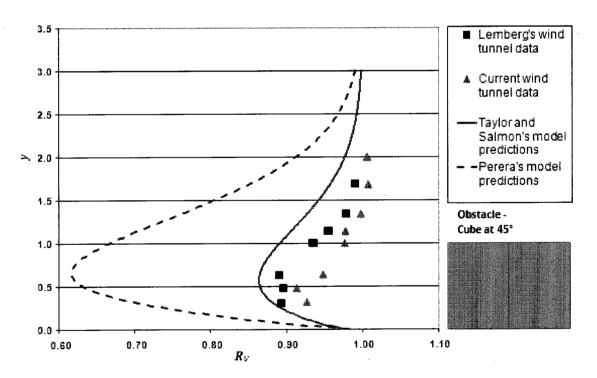


Figure 4.7 – Vertical R_V profiles in the wake of a cube at x = 6.84, z = 0, with $a = 45^{\circ}$.

In the case of the two-dimensional wall, the mean flow properties are independent of z. Although this was not seen in Figure 4.8, it is expected that for obstacles of very large AR, similar behavior would be observed. Mean flow quantities are likely independent of z in the centre region of the obstacle, furthest from the lateral edges. Of key interest is the lateral distance from the edge of the obstacle to the point at which the flow is the same as the two-dimensional case, defined here as z_{2D} . This can be thought of as the distance inside the wake from the lateral edge of the obstacle at which edge effects are no longer present. The derivation below shows that at a constant height, this distance will increase with downwind position. Figure 4.9 illustrates two regions in the wake. Near the obstacle, where edge effects are not present, the mean flow is independent of z. Further away from the obstacle, significant wake effects are present, but these do vary with z. (It should be emphasized that the flow will always be three-dimensional in nature, even in the region closest to the obstacle.) In Figure 4.9, at a downwind distance of x, edge effects are transported inside the wake up to the z_{2D} position indicated. Between z_{2D} and the obstacle centerline, mean flow properties in the wake are similar to the two-dimensional case.

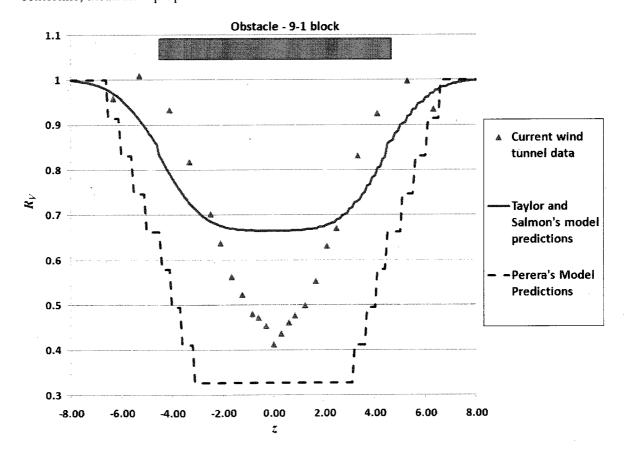


Figure 4.8 – Lateral R_V profiles in the wake of the 9-1 block at x = 7.17, y = 0.94, $a = 0^\circ$.

It has been assumed that z_{2D} is a function of x. This can be explained by considering the transport of momentum from the edge of the wake into the centre region. The mean wind speed \bar{u} between the obstacle and any downwind position in the wake can be expressed in terms of the time t that an air parcel takes to travel the downwind distance x, as shown in Equation 4.7.

$$\overline{u} = \frac{x}{t} \tag{4.7}$$

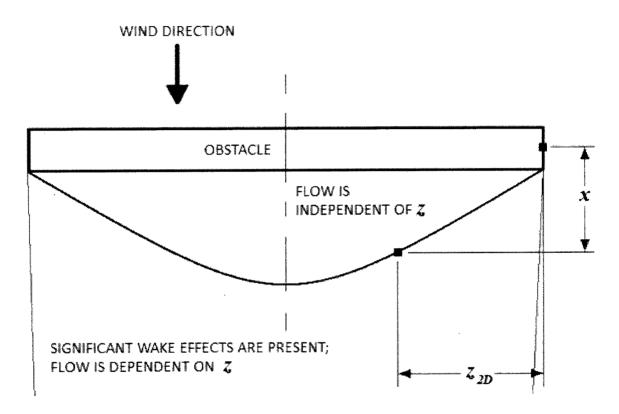


Figure 4.9 – The wake of a very wide obstacle, divided into regions when the flow is dependent on z, and where the flow is independent of z. y is constant.

Momentum is transported into the wake from the outer region. z_d is defined as the lateral distance into the wake that the momentum diffuses, from the edge of the obstacle. Turbulent motions will diffuse momentum into the wake at a range of scales, each of which would have its own z_d value. According to the gradient-diffusion hypothesis, the flux of momentum into the wake will depend on the eddy diffusivity ε_z and the mean momentum gradient [31]. Eddy

diffusivity is the sum of the molecular and turbulent diffusivities, and is mathematically analogous to the diffusion coefficient in Fick's Law [31]. Eddy diffusivity can be thought of here as the mean square displacement of momentum in the lateral direction, from the edge of the wake, over a time of t. This is the same t as in Equation 4.7, since the time that the air parcel takes to travel the distance x is the same as the amount of time that momentum from outside the wake has been in 'contact' with the wake region, and can be transported inside. In terms of z_d , mean refers to the average distance momentum has diffused, considering turbulent motions of all scales.

$$\varepsilon_z \sim \frac{\overline{z_d^2}}{t} \tag{4.8}$$

Combining the above two expressions, it can be seen that

$$\frac{\overline{z_d^2} \cdot \overline{u}}{\varepsilon} \sim x \tag{4.9}$$

It is assumed that eddy diffusivity will vary directly with the integral lengthscale of turbulence L, and the rms velocity u_{rms} .

$$\varepsilon_z \sim L \cdot u_{rms}$$
 (4.10)

From this assumption

$$\frac{\overline{z_d^2} \cdot \overline{u}}{L \cdot u_{max}} \sim x \tag{4.11}$$

L is assumed to be on the order of z_d , and the rms velocity is assumed to vary with mean wind speed. The expression then simplifies to

$$z_{\perp} \sim x \tag{4.12}$$

The expression above is essentially saying that the lateral distance z_d to which edge effects are transported into the wake will vary with downwind distance x. At greater downwind distances,

edge effects have had more time to diffuse and be convected into the wake. At a distance slightly greater than z_d , mean edge effects will be not present; this is the definition of z_{2D} .

$$z_{2D} \sim x \tag{4.13}$$

There may also be a dependence of z_{2D} on the obstacle's PR and RA. This is not directly investigated here; however, through appropriate training, wakeNET should be able to predict this dependence. It is recognized that the above derivation contained several assumptions that may not be valid at all regions in the wake. For example, the integral lengthscale L may be smaller than the lateral distance to the edge z_d at large downwind distances, since z_d could be much greater than the height of the obstacle. It is expected that these assumptions prevent the creation of an accurate wake model using a similar approach; however, it is thought that the main conclusion above is still valid, since the assumptions are reasonable for an order of magnitude analysis.

Based on Figure 4.8, in the wake of the 9-1 block, z_{2D} is greater than 4.5 h at a downwind position of 7.17 h, because R_V always shows a dependence on z. To see a region in a wake where R_V is independent of z, the obstacle's AR would have to be increased, or an R_V profile could be measured closer to the obstacle.

4.5.4 Wake Symmetry

Figure 4.10 shows the lateral velocity profiles in the wakes of three blocks, at x = 7.17, y = 0.94. In this case, all three blocks are oriented normal to the mean flow direction. A strong degree of symmetry can be seen, which agrees with the findings of Hansen et al. [24] for the flow around a bluff body with the front face oriented normal to the wind direction. It is also noted that symmetry is present even when the obstacle has an angled roof.

4.5.5 Far Wake Persistence

The distance downwind of an obstacle at which wake effects are still evident is of great interest. As discussed in Chapters 2 and 3, the magnitudes of wake effects depend strongly on the

orientation of the obstacle relative to the wind direction. Figure 4.11 and Figure 4.12 contain R_V profiles in the far wake, at x positions of up to almost 40 h downwind. The profiles in Figure 4.11 were measured on the centre line, z = 0, when the object was oriented at 0° . Profiles in Figure 4.12 were measured when the object was oriented at 45° , and at lateral positions off the centre of the plane. Actual z positions used in Figure 4.12 were chosen based on estimates of where the maximum velocity deficit occurs.

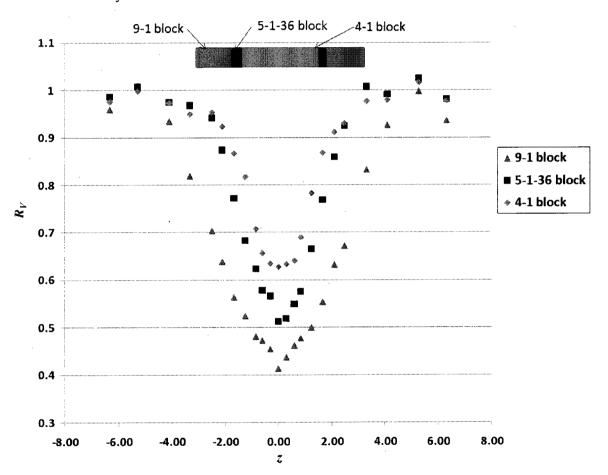


Figure 4.10 – Lateral R_V profile in the wake of the 9-1 block, the 4-1 block, and the 5-1-36 block, at x = 7.17, y = 0.94, $a = 0^{\circ}$.

As downwind distance increases, R_{ν} will recover, eventually attaining a value of 1.00. In Figure 4.11, recovery is slow but clearly evident for the 9-1 block. Recovery is less evident for the 4-1 block. Although R_{ν} is within 4% of its unsheltered value by x = 28.6, it does not appear to

change significantly between this point and x = 37.6. This suggests that low magnitude wake effects will be evident even at large distances downwind of obstacles with large AR.

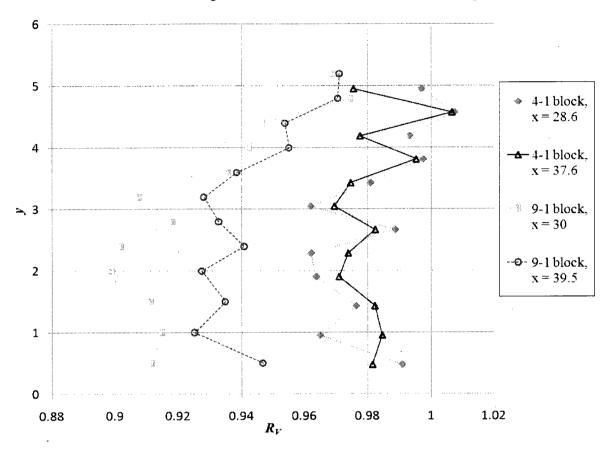


Figure 4.11 – R_V profiles in the far wakes of the 4-1 and 9-1 blocks, at z=0, $a=0^\circ$.

It is observed in Figure 4.12 that R_v profiles at the two x locations appear to be similar at some heights, for the 4-1 block. For example, there is a strong similarity at y = 2.4, 2.8, and 3.2. This apparent consistency (regardless of x position) may indicate the presence of standing vortices acting at these heights, which would generally be detrimental to the performance of a small wind turbine. The presence of vortices could be confirmed by flow visualization.

In general, the strongest wake effects and greatest wake persistence are seen when the model is oriented at about 45° to the wind. This can be seen by comparing Figure 4.11 and Figure 4.12. At $a = 47^{\circ}$, Hansen et al. [24] found that the mean velocity wake was still apparent at x = 80, which was drastically different from wake behavior when $a = 0^{\circ}$. Recall that Hansen's block had an AR of 2.44. Flow visualization from Hansen et al. [24] shows that a pair of longitudinal

vortices was generated at the leading corner of the roof (as seen in Figure 2.2). The only mechanisms to dissipate the angular momentum of these vortices are the viscous and turbulent stresses acting about the axis of each vortex; the vortices will dissipate slowly. Large turbulence intensity excesses are also evident far downwind of the obstacle at 47°. It is speculated here that these standing vortices may be similar in nature to the wingtip vortices created by an aircraft, which can also persist over a large distance. The extent to which these flow features can be confirmed by the field experiment is discussed in Chapter 5.

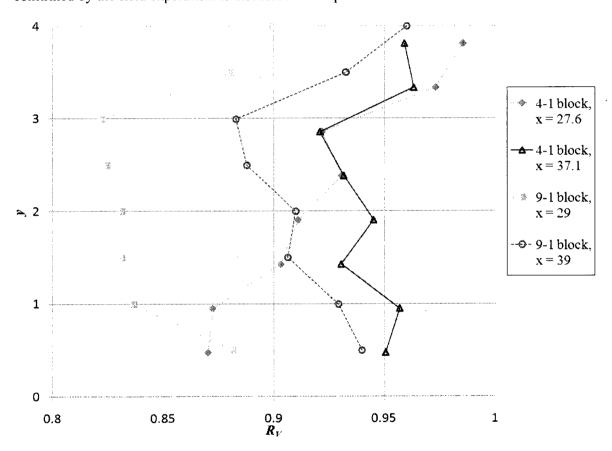


Figure 4.12 – Far wake R_V profiles of the 4-1 and 9-1 blocks, at z= -4.95 and -5.2, respectively. $a=45^{\circ}$.

4.5.6 Comparison to General Guidelines

Small wind turbines are often sited using general guidelines, as described in Chapter 1. In this section, wind tunnel results are used to evaluate the suitability of using two particular

guidelines to site a turbine near four buildings. The four obstacles are of a different AR. The guidelines do not incorporate any factor related to the width of the obstacle, so it is assumed that their suitability will depend greatly on the AR of the obstacle (as well as on the PR and RA, albeit to a lesser extent).

Guideline A states that a wind turbine should be at least 20 h downwind, at a height greater than twice that of the obstacle [11]. Guideline B recommends that a turbine should be installed on a tower such that it is at least 9 m above any obstacles within 91 m [10]. To compare measurements to Guideline B, it is necessary to specify a scale for the wind tunnel tests. A scale of 1:160 is chosen. The building height is then 8 m, which is a typical height for a low rise building. The second guideline implies that a turbine should be at least 11.4 h away from an obstacle, and 1.13 h above it.

The general guidelines do not explicitly say that there will be no obstacle effects evident at their recommended locations. For the purposes of this comparison, it is assumed that if obstacle effects have mostly disappeared by the recommended location, then the guideline is valid. Specifically, wake effects will be said to have 'mostly disappeared' if $R_V \ge 0.98$ and $R_I \le 1.05$. Otherwise, the guideline is inadequate, and its use may result in a turbine being located at a sheltered site. If the obstacle effects disappear well before the recommended location, then the guideline is still valid but not ideal, since in this case it would be precluding sites that are in fact acceptable.

As discussed in the previous section, the greatest wake effects are typically seen when the object is oriented at roughly $a = 45^{\circ}$. For this reason, guidelines will be compared to wake effects of obstacles at this angle. Figure 4.13 and Figure 4.14 contain profiles of R_P and R_I , respectively, in the wakes of four obstacles. The obstacles are the cube, the 2-1 block, the 4-1 block, and the 9-1 block, at downwind distances of 15.7 h, 20 h, 19 h, and 20 h, respectively. Recall that R_P was defined in Equation 3.3 as the ratio of sheltered to unsheltered power density in the wind. The lateral position z of each profile was always off centre, where measured wake effects were

strongest. This does not mean that the profiles shown in Figure 4.13 and Figure 4.14 represent the *greatest* velocity deficits that are present at this x location; to find the absolute maximum deficits, profiles would have to be taken at a high resolution of z and a. The profiles shown simply represent the greatest wake effects that were actually measured.

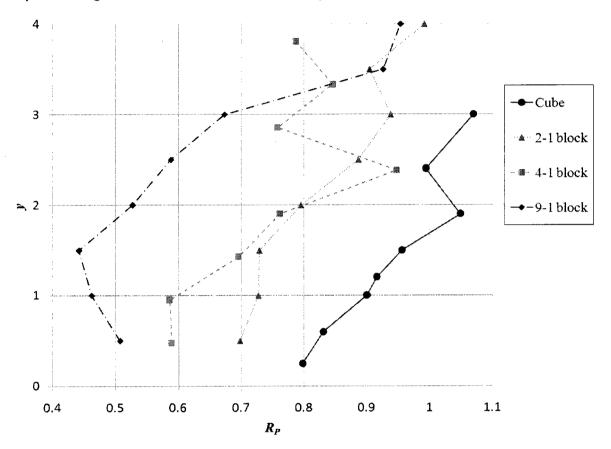


Figure 4.13 – R_P profiles in the far wakes of the cube, at x = 15.7, z = -3.29; the 2-1 block, at x = 20 z = -2.73; the 4-1 block, at x = 19, z = -4.95; and the 9-1 block, at x = 20, z = -5.2. For all four obstacles, $a = 45^\circ$.

Based on wind tunnel measurements, wake effects for the cube at y = 2 have disappeared by x = 15.75. Guideline A is suitable for cube shaped obstacles. At x = 10.7, y = 1.8 (not shown), $R_V = 0.99$ and $R_I = 1.02$, meaning that if a turbine was placed at that location, its power output would be only slightly reduced for that wind direction. In this case, Guideline B is also adequate.

For the remaining three obstacles, both guidelines are unsuitable for wind from this direction. At x = 20, there are still significant wake effects on R_P and R_I at heights above y = 2. As

AR increases, so does R_l , while R_p decreases. Examination of wind tunnel results for the 2-1 block indicate that for $|a| < 22.5^{\circ}$ and $|a| > 67.5^{\circ}$, the wake has largely dissipated by x = 20, meaning that the first guideline is suitable for these wind angles. However, for the 4-1 and 9-1 blocks, strong wake effects are visible for the majority of obstacle orientations. This is especially true for the 9-1 block. Looking at Figure 4.11 and Figure 4.12, it can be seen that significant wake effects are still present well beyond 20 h downwind, at and above 2 h from the ground. Neither of the guidelines cited here should be used to site a turbine near obstacles of large AR.

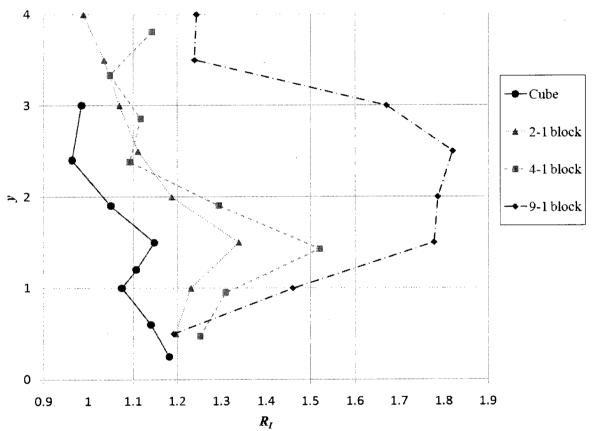


Figure 4.14 – R_I profiles in the far wakes of the cube, at x = 15.7, z = -3.29; the 2-1 block, at x = 20, z = -2.73; the 4-1 block, at x = 19, z = -4.95; and the 9-1 block, at x = 20, z = -5.2. For all four obstacles, $a = 45^{\circ}$.

The analysis above is fairly simple. It was intended only to show that for many buildings, large wake effects are evident at downwind distances and heights greater than those specified by general guidelines. To calculate the $mean R_P$ value at a site, a wind rose is also required. For

example, if a turbine is located very close to an obstacle, its mean power output may *not* be significantly affected by that obstacle, if strong winds only rarely come from the obstacle's direction. Of most importance are obstacles that affect wind from the prevailing wind direction.

Additional wind tunnel results are shown in Chapters 5 and 6. In Chapter 5, results from a field experiment are compared to results from the wind tunnel. In Chapter 6, the performance of the NN model is evaluated based on wind tunnel and field data.

5.0 Field Experiment

A field experiment was conducted to obtain flow measurements in the wakes of full scale obstacles exposed to the actual ABL, for the purpose of obtaining validation data for wind tunnel simulations and wakeNET predictions. Velocity and turbulence intensity ratio values were obtained for a range of locations, wind directions, aspect ratios, and plan ratios. This experiment was set up during August 2009. Useful measurements were made from September 2009 to December 2009, after which time the field experiment was discontinued due to winter weather.

5.1 Experimental Set Up

The site (43°18'N, 80°33'W) is located in a large, flat open field in a rural area southwest of Kitchener, Ontario, Canada. Prevailing winds are from west-southwest. The experimental layout is shown in Figure 5.1. Figure 5.2 is a photograph of the site in which all towers, sensors, and an obstacle (here, a large trailer) are visible.

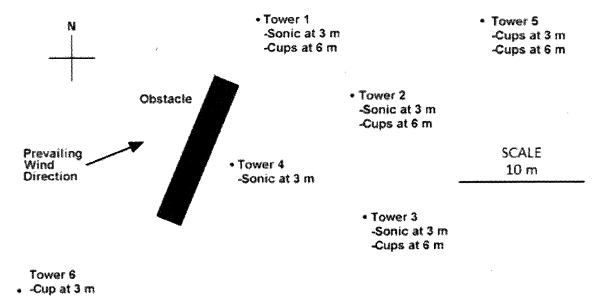


Figure 5.1 - Layout of field experiment, with the trailer as the obstacle

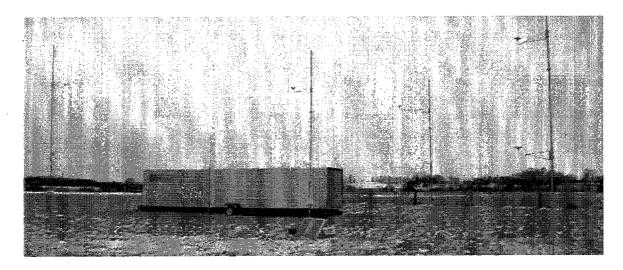


Figure 5.2 – Photograph of the field site

Six 7 m towers were equipped with anemometers and erected on the site. The distance from each tower to the obstacle is included in Table 5.1. Towers 1, 2, and 3 were placed at angles of 7°, 50°, and 90° to the obstacle minor axis, respectively, as seen in Figure 5.1. This arrangement allowed measurement of the obstacle wake for a wider range of wind directions and model orientations. Tower 4 was located closest to the obstacle, in line with tower 3. Tower 5 was located in line with tower 2. Tower 6 was located upwind and is only used as a reference tower. There were a total of ten anemometers in the field, as summarized in Table 5.1. Three models of anemometer were used; three Campbell Scientific CSAT3 three-dimensional sonic anemometers, one RM Young 81000 three-dimensional sonic anemometer, and six NRG #40c cup anemometers. A Campbell CR-1000 datalogger was used for data collection. The sonic anemometers were sampled at 20 Hz, while the cup anemometers were sampled at 2 Hz. It was not essential to store sonic data at 20 Hz, since the datalogger could be used to calculate averages over the desired sampling period. However, it was felt that higher resolution wind data may prove useful in future studies. All raw data was stored, requiring the use of a 2 GB CompactFlash card. Two 50 W photovoltaic solar panels were used to charge two lead acid batteries, which in turn provided constant power to the datalogger and the sonic anemometers.

Table 5.1 - Summary of anemometers used in the field experiment

					Tower Distance
Anemometer	Anemometer		Height	Centre plane	from Centre of
number	type	Tower	(m)	angle (°)	Obstacle (m)
1	Campbell Sonic	1	2.97	83	11.8
2	Campbell Sonic	2	2.75	40	13.45
3	Campbell Sonic	3	3.02	0	14.9
4	RMY Sonic	4	2.94	0	3.25
5	NRG cup	5	6	40	25.45
6	NRG cup	5	3	40	25.45
7	NRG cup	1	6	83	11.8
8	NRG cup	2	6	40	13.45
9	NRG cup	3	6	0	14.9
10	NRG cup	6	3	150	20

Once the towers and anemometers were set up, one month of baseline data was collected without an obstacle in place. This was to determine and quantify any variation in velocity or turbulence intensity ratios between the anemometers due to minor terrain, tower or instrument effects, before an obstacle was present. Of main interest here are wind directions that would cause the anemometers on towers 1 to 5 to be sheltered by the obstacle. This range depends on the obstacle in place but is generally somewhere between 180° and 360°. The unsheltered data was used to create two sixth order polynomials for each anemometer, to predict the baseline velocity ratio and the turbulence intensity ratio as a function of wind direction. These baseline predictions were then taken into account when calculating sheltered ratios with an obstacle present.

The open fetch upwind of the obstacle location in several wind directions is shown in Figure 5.3. It was thought that the upwind fetch was great enough in all wind directions of interest that interference effects from the wakes of other obstacles far upwind would be minimal, or at the very least, typical of a site where a small turbine might be installed.

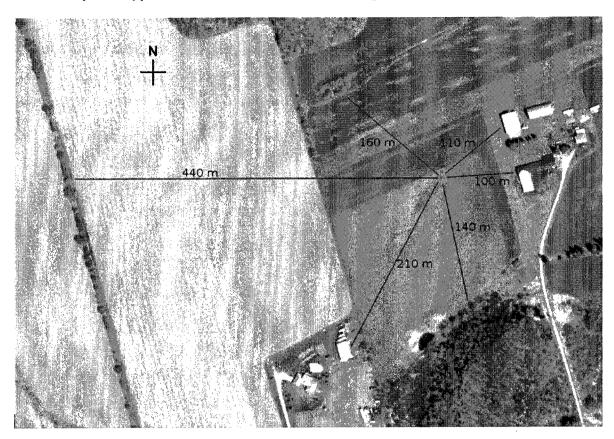


Figure 5.3 – Distances to nearby obstacles at the field site (photo: Grand River Conservation Authority).

Three obstacles were tested. These are described in Table 5.2. The first obstacle set up was the large wall, which was placed in the obstacle location specified in Figure 5.1. Data was collected for 18 days, and the obstacle was then replaced by the smaller wall. Data was then collected for 31 days. The smaller wall was removed, and a large trailer was put in place. During the first 8 days with the trailer, the bottom was open. Data was collected but not used; it may prove valuable to future studies on the effect of obstacle porosity on a wake. The bottom of the trailer was filled in with railroad ties, such that the obstacle was now essentially a very large

block. Data was collected for the next 77 days. However, during the last 55 days, problems arose related to the weather. The solar panels were intermittently covered with snow and ice, preventing the batteries from being charged. This created many large gaps (spanning days) in the raw data; since the datalogger had no power, no measurements were recorded. Often, enough power was available for only one or two sonic anemometers to take measurements. Another weather related issue is icing, which was evident at some anemometers. Table 5.2 summarizes the characteristics of each obstacle, and the total time each was in place.

Table 5.2 – Summary of obstacle characteristics

Large Wall	Small Wall	Trailer
2.48 m	2.48 m	2.6 m
5.14 m	2.57 m	12. 3 m
0.4 m at base	0.4 m at base	2.16 m
0.1 m at top	0.1 m at top	
18 days	31 days	22 days
	2.48 m 5.14 m 0.4 m at base 0.1 m at top	2.48 m 2.48 m 5.14 m 2.57 m 0.4 m at base 0.4 m at base 0.1 m at top 0.1 m at top

5.2 Data Analysis Procedure and Considerations

Raw data was analyzed using MATLAB script. Recorded data was quality controlled and averaged over 30 second periods. It is pointed out that this is not a standard averaging time; 10 minutes or 1 hour would be more common [18]. In this particular field experiment, the sampling time is reduced because having a consistent wind direction over the sampling time is crucial. For example, if the wind at a sensor of interest is coming from an unsheltered direction for 25% of the sampling time, and the sheltered direction for 75% of the sampling time, then the measured velocity deficit at that sensor will be 25% lower than its 'true' value. It is thought that shorter sampling times will help to prevent this problem, since the wind is much more likely to be coming from a very consistent direction for 30 seconds than for 10 minutes or longer. The main downside to using a 30 second sampling time is that 30 second turbulence intensity values may

not capture all relevant velocity fluctuations. Any turbulent fluctuations acting at timescales of greater than 15 seconds (corresponding to 0.07 Hz) may not be taken into consideration. Large timescale eddies will also be those with greater length scales, and as seen in Figure 5.4, a typical unsheltered power spectrum measured in the field, the larger scales do contain large amounts of energy. The effects of these large turbulent scales on a turbine are unknown and beyond the scope of this thesis.

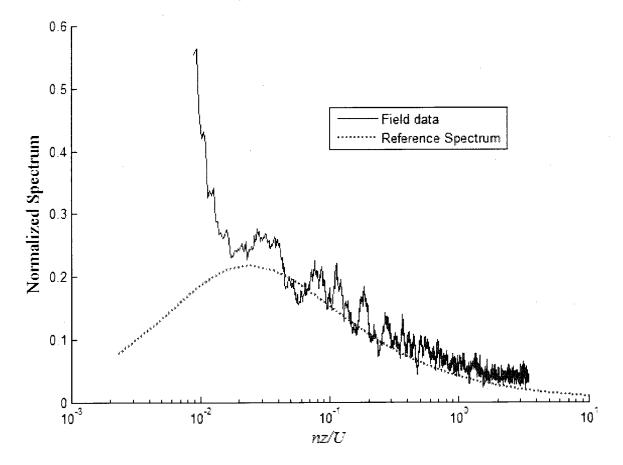


Figure 5.4 – Comparison of upwind turbulent power spectra in the field to the reference curve [42]

The spectrum shown in Figure 5.4 was measured using a CSAT3 sonic anemometer operating at 20 Hz. n is the frequency, z is the height at which the velocity was measured, and U is the mean wind speed at that height. The reference shown is the Kaimal spectrum, as reported by Burton et al. [42]. For details regarding normalization of the spectra, see [42]. In the measured

curve, an interesting peak is evident at the lowest end of the frequency range. The peak corresponds to a period of roughly 70 seconds, which is still a fraction of the 1800 second time period from which the spectrum was generated. The cause of this spike could not be determined. It is consistently present in the spectra of all field data samples. Because the field experiment is exposed to actual wind, there is no known method of 'adjusting', or need to 'adjust' the incoming flow. Sheltered spectra are not examined in this thesis; however, future investigation into how the power spectrum changes with position in the wake might provide a more useful description of turbulence levels in the wake than the simple turbulence intensity value used here.

Data was filtered to eliminate points with a low mean wind speed (less than 4 m/s), or high standard deviation of wind direction (greater than 12°). This ensured that all wake measurements were based on strong, consistent winds. The specific cut-off values used were determined by trial and error; the optimal values were those that resulted in little change in mean R_V and R_I values when made more stringent. R_V and R_I were calculated using Equations 3.1 and 3.5, as described in Chapter 3. Each desired output ratio requires an unsheltered value, defined as the value in the upwind flow at the same height. Because the test site was in the middle of a large field, it was assumed that without the influence of the obstacle, the wind at each tower location would be closely correlated, and in fact would be the virtually the same as the upwind flow. This assumption was shown to be valid during baseline data collection. This means that any sensor that is not sheltered could be used as the 'upwind' or reference sensor. It was necessary to determine which sensor was unsheltered for each observation. If the wind was coming from between 140 and 245 degrees, tower three was considered to be unsheltered, so readings from anemometers three and nine would be used as the reference 3 m and 6 m wind speeds. If the wind was coming from any other direction, then tower one was considered to be unsheltered, and readings from sensors one and seven would be used as the reference wind speeds. (The specific wind direction values used to define which sensor was unsheltered were validated before the final data analysis). Once the unsheltered wind speed and turbulence intensity at each time step was determined, the

corresponding ratios of these quantities were calculated. The time series ratios were then sorted by wind direction into bins. A bin size of 10° was used. Increasing the bin size would result in more data points per bin, and higher confidence in the mean R_V and R_I values, which is desirable. The downside of increasing the bin size is that the angular resolution of wind direction would be smaller. It was found that the use of 10° bins provided a large enough number of data samples in each bin, in general, while also providing sufficient resolution for this experiment.

Using the methods of Coleman and Steele [41], the uncertainties associated with \overline{V} values measured by the CSAT3, RM Young, and NRG anemometers have been determined to be 1.0%, 1.3%, and 2.5%, respectively. Uncertainties associated with V_{rms} for the three models are 3.4%, 5.7%, and 18.1%. These values are based on uncertainties given in the sensor manuals [44] [45] [46], and are assumed to be valid for 95% confidence intervals. Since R_V and R_I are based on \overline{V} and V_{rms} , the uncertainties in the two ratios are dependent on the sensors used to obtain their values. Table 5.3 summarizes the uncertainties at each sensor location. The calculation of these values is described in Appendix F. It is emphasized that the values in Table 5.3 represent the uncertainty associated with a single R_V and R_I value; by collecting a large number of samples, uncertainty can be reduced.

An important source of error that has not yet been considered is that the sheltered and unsheltered \overline{V} and I values were not measured at exactly the same point. Even if the obstacle was not present, the wind at the sheltered tower would not be exactly the same as the wind at the unsheltered tower. The magnitude of this uncertainty is very difficult to quantify and depends on factors such as wind direction, atmospheric stability, and weather. It is not accounted for in Table 5.3, meaning that these estimates are likely too low; it is expected to be a major source of uncertainty. Recall that at the start of the experiment, the wind was measured for a month without an obstacle in place in order to establish baseline relationships between the sensors. This procedure was designed to minimize the uncertainty associated with the distance between the

sheltered and unsheltered towers. It was hoped that by incorporating the mean baseline relationship, bias uncertainty would be reduced. Still, for any given R_V or R_I value, the effect associated with distance between the towers could vary greatly from the baseline value. This means that even when the baseline relationship is considered, and the bias error is reduced, there will still be some (precision) uncertainty associated with the separation distance of the two towers. However, this uncertainty can be minimized as more samples are collected.

Table 5.3 – Uncertainties in R_V and R_I by sensor location

Location	Uncertainty in R_V	Uncertainty in R_I
1	1.4%	4.8%
2	1.4%	4.8%
3	1.4%	4.8%
4	1.6%	6.6%
5	3.5%	25.6%
6	2.7%	18.4%
7	3.5%	25.6%
8	3.5%	25.6%
9	3.5%	25.6%
10	2.7%	18.4%
1	1	

5.3 Convergence of Field Data

Flow in the field experiment is much more complex and difficult to predict than flow in the wind tunnel. The wind cannot be controlled; it is inherently non-stationary [29], which means that its mean properties can change over time. The wind direction will drift, even during the short averaging time used in the field experiments. Upwind flow characteristics such as wind shear, turbulence intensity, and scales of turbulent motion will vary over time. Because of this

inconsistency in the incoming wind, many measurements must be averaged in order to obtain reasonably accurate mean velocity and turbulence intensity ratio values.

The length of time that each obstacle was in place is given in Table 5.2. During these time periods, the wind was measured constantly at all anemometer locations, from which a large number of data samples were collected, as described above. Each data sample is made up of a single value for R_V and a single value for R_I . For many wind sectors (or bins), hundreds (or thousands) of observations were collected. For others, only a few were collected. In some cases, no observations met the filtering criteria (however, these were generally not wind directions of interest). Final $\overline{R_V}$ and $\overline{R_I}$ values were calculated for each wind sector by taking the means of all the sample values from that sector that met the filtering criteria.

It was necessary to estimate whether or $\overline{R_V}$ and $\overline{R_I}$ were good representations of the 'true' mean values. It is recognized that there may not actually be a 'true' value, or that the 'true' value will change over time; upwind conditions such as surface roughness and atmospheric stability are always changing, which will have some (small) effect on the structure of the wake. However, the concept of a true value is useful in this analysis, and is justified by assuming that changes in the 'true' mean over time are small.

Based on the number of samples available for each wind direction, N, the range in which the true value of $\overline{R_V}$ is expected to fall can be determined by calculating the 95% confidence interval [41]. This range is specified by the precision limit $P_{\overline{RV}}$. Equation 5.1 expresses $P_{\overline{RV}}$ in terms of N and the precision index S_{RV} of all N samples.

$$P_{\overline{RV}} = t \, \frac{S_{RV}}{\sqrt{N}} \tag{5.1}$$

For example, after filtering, 199 R_V samples were available for wind from sector 28 (centered at 275°) for the time period when the large wall was in place. At sensor 4, $\overline{R_V}$ is found to be 0.499, and the precision index S_{RV} is 0.082. Since N = 199, the value of t is taken as 2, from

the *t* distribution [41] using a 95% confidence interval. The precision limit $P_{\overline{RV}}$ is 0.012. This means that $\overline{R_V} = 0.499 \pm 0.012$, 19 times out of 20.

Using this technique, the precision limits of R_V and R_I were found for each sensor, for each wind direction, for each obstacle. Since all sensors have the same number of samples for each wind direction, and use the same t value, the variation of precision limit with wind sector will be due entirely to variation in the precision indices of R_V and R_I . Figure 5.5 summarizes the maximum precision limit of R_V for each wind direction, for each obstacle. Only wind sectors 18 to 36 are shown, which covers the range of interest. The maximum precision limit is typically associated with sensor 4, which observes the greatest turbulence intensities due to its proximity to the obstacle.

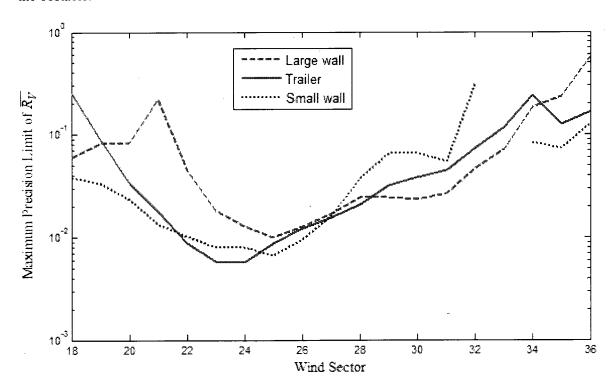


Figure 5.5 – Maximum precision limit of mean R_V considering all sensors.

Figure 5.6 shows the maximum precision limit of R_l , out of all ten sensors, for each wind sector. A logarithmic scale is used because the precision limit quickly increases for sectors where the number of samples is smaller, such as sectors 32 to 36. Again, it should be emphasized that these are the greatest precision limits for each wind direction. Typically, the precision limit at

sensor 4 was greater than that at the other sensors. In Figure 5.5 and Figure 5.6, there is a gap for sector 33 for the small wall curve; the precision index could not be calculated, because only one sample for that wind sector met the filtering criteria. The precision limit of \overline{R}_I is generally greater than that of \overline{R}_V . This is related to the greater uncertainty in R_I measurements, which caused S_{RI} to be greater than S_{RV} . The curves for each obstacle follow very similar trends.

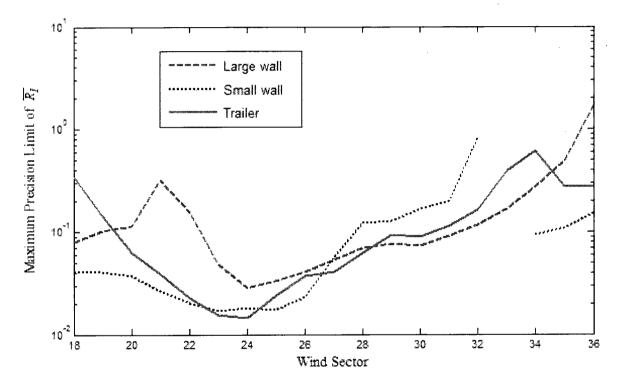


Figure 5.6 – Maximum precision limit of mean R_I considering all sensors.

An additional approach was used to estimate how well $\overline{R_V}$ and $\overline{R_I}$ converged to their true values. Figure 5.7 illustrates how the point of convergence was determined using this second approach. The mean R_V value was calculated using an increasing number of data samples. The point of convergence is defined as the number of R_V samples needed such that the calculated mean R_V value is within 2% of its final value. As well, immediately prior to the point of convergence must be the last time the calculated mean value is outside this 2% window. 2% was chosen because it was felt that if field experiment results were within 2% of their 'true' value, this would be satisfactory.

Figure 5.7 shows how the average wind speed typically converged. This plot is for a single wind direction, for a single sensor, for a single obstacle. Here, it is seen that the value converged after 118 samples. 199 were available in total, meaning that 81 samples after convergence confirmed this result. This is taken as strong evidence that for this wind direction and obstacle, the final R_V value will be fairly close to the 'true' value. On the other hand, if there were only a few samples after convergence, it means that convergence was achieved later and the final R_V value may not be accurate.

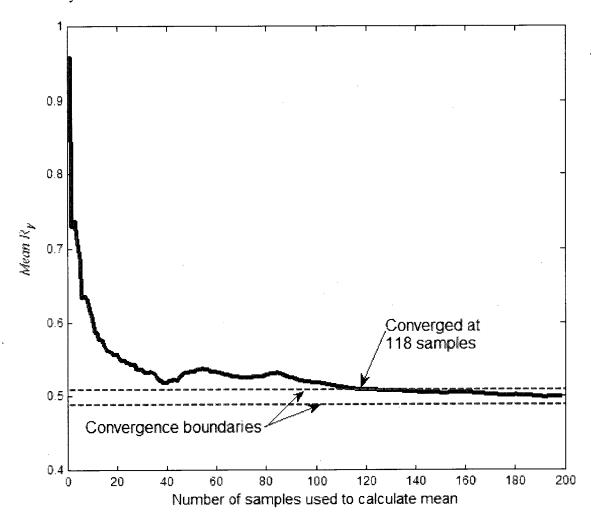


Figure 5.7 – Convergence of R_{ν} as more data samples are included in the calculation, for sensor 4. Obstacle is the large wall, with the wind direction bin centered at 275°.

The convergence point was calculated for all wind sectors, for all sensors, for each of the three obstacles. Some sensors converged faster than others. Figure 5.8 shows the total number of

useful samples collected during the time period that the large wall was in place. Also shown are how many samples were needed until convergence was achieved for all sensors, and how many samples were obtained after convergence confirmed $\overline{R_V}$ at all sensors. The solid and dashed lines can both be considered as 'worst case', since some sensors would converge earlier than others (although typically, for a given wind direction and time period, the sensors would converge after a similar number of values).

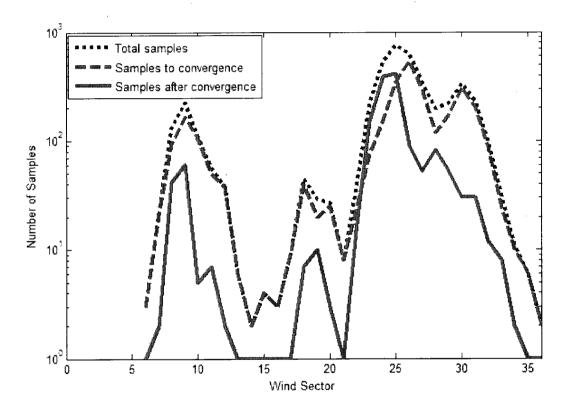


Figure 5.8 - Convergence for each wind sector, with the large wall obstacle

The main purpose of Figure 5.8 is to illustrate the degree of confidence in R_V (and by association, R_I) values for each wind direction. This is captured by the solid line. For example, since there were many samples after convergence for wind sector 25, R_V values for this sector are thought to be fairly accurate. Conversely, R_V for sector 21 did not converge until all values were taken into account, meaning that the final value may not be a great representation of the 'true'

value. Sectors 1 to 5 did not have any data samples, and therefore no mean R_V or R_I value was obtained for these wind directions.

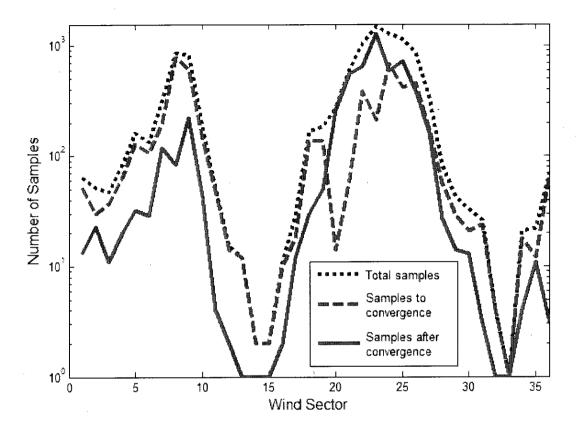


Figure 5.9 - Convergence for each wind sector, with the small wall obstacle

Figure 5.9 is similar to Figure 5.8, but was made for the small wall. Since each obstacle was in place for a different time period, it was necessary to estimate convergence for each obstacle separately. Figure 5.10 shows the total samples collected, samples to convergence, and samples after convergence of data collected while the trailer was in place. Along with Figure 5.6 and Figure 5.7, these three figures can be consulted to estimate the confidence in the field data for a particular sector of interest, which will be very useful in the remainder of this thesis. When the number of samples after convergence is greater than the number of samples to convergence, more samples confirmed the mean R_{ν} value than were needed to obtain it. An example of this is at wind sector 20 in Figure 5.9.

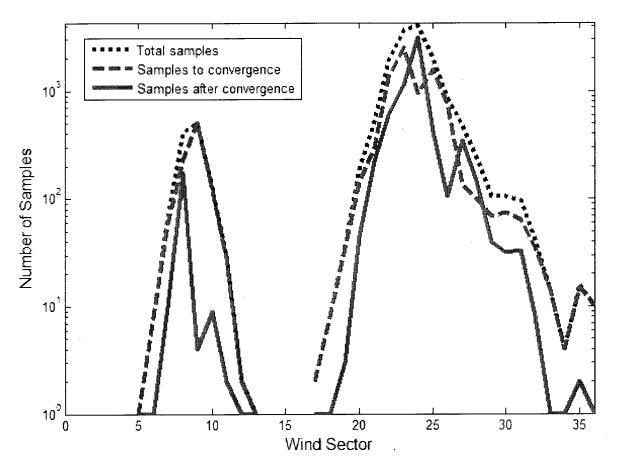


Figure 5.10 - Convergence for each wind sector, with the trailer obstacle

The same conclusions can be arrived at using the two approaches described in this section. For example, in the trailer wake, wind from sector 24 had a large number of samples after convergence (~3000, as indicated in Figure 5.10) as well as a very low $P_{\overline{RV}}$ value (~0.006, as indicated in Figure 5.5). Similarly, at sector 30, only ~30 samples confirmed $\overline{R_V}$, and $P_{\overline{RV}}$ was correspondingly higher, at 0.04.

To use the first approach, where precision limits were estimated, it was necessary to assume that R_{ν} has a Gaussian distribution [41]. The advantage of the second approach is that no such assumption is necessary; the convergence of each $\overline{R_{\nu}}$ value could be observed directly. The disadvantage of the second method is that it can be difficult to interpret the results. For example, in Figure 5.7, 81 values confirmed the value of $\overline{R_{\nu}}$. However, on its own, it is not clear whether or

not this indicates that the value is converged. The ambiguity is even greater when fewer values confirm $\overline{R_V}$.

In the remainder of the thesis, field values of R_V and R_I are actually referring to $\overline{R_V}$ and $\overline{R_I}$. Confidence intervals and convergence figures are referred to where needed.

5.4 Wind Tunnel Simulation of the Field Experiment

Since all modeling is based on measurements made in the BLWT, the validity of the model outputs is directly dependent on the validity of the wind tunnel results. By comparing current wind tunnel measurements to field results, any biases present in the model can be estimated and taken into consideration.

It is pointed out that the wind tunnel and field experiments are not measuring exactly the same quantities. In the field experiment, the four sonic anemometers measured three velocity components, from which the north, east, and vertical components could be calculated. Mean wind speeds (and therefore velocity ratios) are calculated based only on the horizontal components (those along the north and east axes) since horizontal components are of main interest to wind turbines. As well, using only the horizontal components allows direct comparison to the cup anemometer readings. The wind direction is defined on the horizontal plane, also based on the north and east components. This means that if *u* is defined as the wind velocity component in the downwind direction, as it is in the wind tunnel, there can be no lateral component. The cup anemometers measured the resultant of any velocity components on a horizontal plane. No vertical component could be measured, which results in the same quantity as the sonic anemometers. In the wind tunnel, the measured wind speed will be the magnitude of the resultant of the horizontal and lateral velocity components (which are in the *x* and *y* directions, respectively). These are the velocity components on a vertical, longitudinal plane, normal to the film at the end of the probe.

To summarize, wind tunnel readings will include any vertical component, while field readings do not. Wind tunnel readings will not measure the lateral component, which is not present in the field measurements, by definition of wind direction. Since in most cases, vertical and lateral components are expected to be negligible, these differences should not affect the validity of directly comparing results from sonic anemometers to wind tunnel results. Field measurements indicate that the mean vertical component of wind speed is generally less than 0.1 m/s for sensors 1, 2, and 3, and less than 0.2 m/s for sensor 4. Recall that sensor 4 was located on tower 4, in the near wake region of the trailer, which induced a vertical component into the flow. In some cases, the wind at sensor 4 was moving at greater than 1 m/s downward; even then, it was very rare for the vertical velocity component at sensor 4 to exceed 10% of the wind speed on the horizontal plane. At the other sonic anemometers, the peak value of vertical wind speed was only about 5% of horizontal.

Wooden models were created for the wind tunnel tests (included in Table 4.1), at scales of 1:25 and 1:52 for the walls and the trailer block, respectively. Models were geometrically similar to the full scale obstacles. In the wind tunnel, measurements were made at locations in the wake corresponding to anemometer locations in the field. The locations of the measurement points of interest in the wind tunnel are fixed relative to the model, as in the field, but will change with the wind direction. In the field, everything is fixed in place, and the wind changes direction; in the wind tunnel, the flow direction is fixed, and everything must rotate to simulate different wind directions. To determine the 'correct' locations at which to measure in the wake, it is first necessary to choose a wind direction of interest. The wind rose was divided into 10° bins, making 36 bins in total. The orientation of the model for wind directions corresponding to the centre of each bin was calculated. From the model orientation, the coordinates of each field anemometer in the wake were calculated. Based on these coordinates, the corresponding measurement position in the wind tunnel was determined for each anemometer. Velocity and turbulence ratios measured at

these locations are compared to those measured in the field, calculated using the 10° bins defined earlier.

5.5 Comparison of Results

Field results were compared to wind tunnel results for each sensor location. Figures included in this section were specifically selected to illustrate the main findings of the field study. Discussion follows presentation of these results.

The variations of R_V and R_I in the wake of the larger wall are shown in Figure 5.11 and Figure 5.12, at anemometers 2 and 3, respectively, as defined in Table 5.1. Similar figures were examined at each sensor, for each obstacle; only a few examples are shown here. All plots in this chapter are shown as a function of incoming wind angle; it is important to keep in mind that as wind angle changes, so does the effective (x, z) position, and a. The plots are not showing the shape of any one obstacle wake; rather, they are simply showing a collection of R_V and R_I values that correspond to a constant sensor location relative to the obstacle.

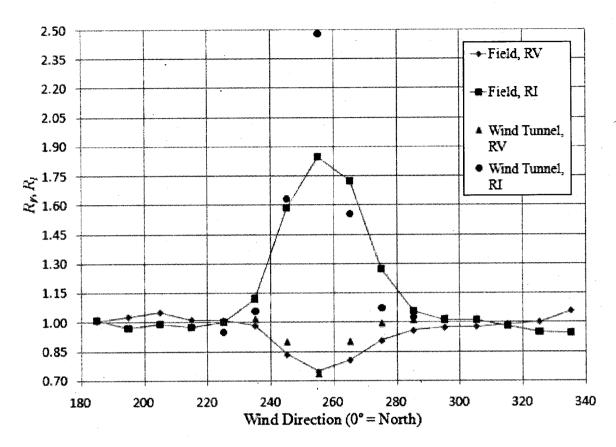


Figure 5.11 – Variation of R_V and R_I at an emometer 2, in the wake of the large wall

Figure 5.13 and Figure 5.14 show how and R_v and R_l vary with wind direction, at sensors 2 and 4, in the wake of the small wall. The variation in R_l and R_l in the wake of the trailer is shown in Figure 5.15 through Figure 5.18, at an emometers 2, 3, 4, and 6, respectively.

Recall that the main objective of the field experiments was to evaluate the validity of the BLWT simulations. As discussed previously, the field measurements are inherently not true values. Also, the wind tunnel and field experiments are not measuring exactly the same quantities. However, field results are treated as being true in this analysis; the wind tunnel results are evaluated based on the extent to which they replicate the field results. Of main interest is the difference between a field measurement and the corresponding wind tunnel measurement, in terms of its absolute value. Table 5.4 gives the mean absolute difference (MAD), in percentage, of both R_V and R_I at each sensor, for each obstacle. Table 5.5 summarizes the MAD of each obstacle, for both quantities of interest.

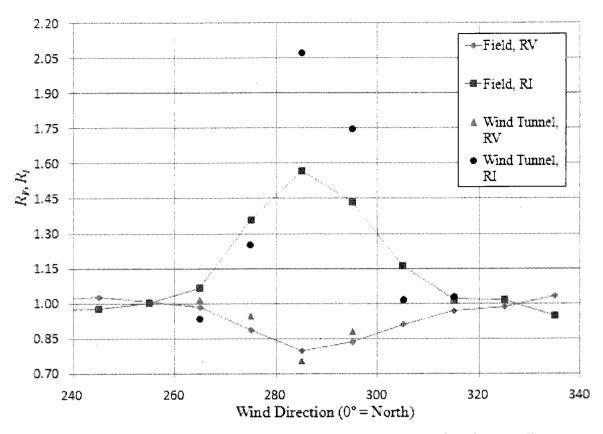


Figure 5.12 – Variation of R_V and R_I at an emometer 3, in the wake of the large wall

 R_V values measured in the wind tunnel generally compared well with those measured in the field, with an overall average variation of about 4.4% between the two data sets. Figure 5.14 and Figure 5.17 show especially strong agreement between the two sets of tests; R_V values from the field and wind tunnel in these figures are very close at these locations. Wind tunnel measurements often tended to slightly under predict the velocity deficit measured in the field, as seen in Figure 5.11 and Figure 5.12. In some cases, wind tunnel measurements greatly under predicted the velocity deficit. Examples of this include at 305° and 315° in Figure 5.16, and 245° in Figure 5.13. Examination of the convergence and precision limits indicates that the uncertainty in the field values in Figure 5.16 is relatively high, which may explain the discrepancy between wind tunnel and field results. Examination of the precision limits also indicates that the uncertainty in the value in Figure 5.13 is very low, which is evidence that there may be another source of the discrepancy between wind tunnel and field R_V values at these points. One possible

explanation for these discrepancies is that the bin size chosen for the field measurements is too large. In Figure 5.13, the low field R_V value for 245° (sector 25) would be appropriate for a wind direction of 255° (sector 26). The slope of R_V between the two points is fairly steep. The wind direction bin size used may have been too coarse; some values in the upper end of wind sector 25, closer to 255°, (for example, at 249°) were much more sheltered than values measured at the lower range of this bin, further from 255° (for example, at 241°). A smaller bin size was not used because it would reduce the number of samples in each bin, which increases uncertainty and the precision limits. In most cases, 10° was sufficiently small, and resulted in an absolute difference values that were independent of bin size.

There might also be an important genuine difference between the wind tunnel and the field tests. *Re* dependence may depend on the nature of the vortices formed in the wake. Hansen et al. [24] suggest that the *Re* dependence of vortex decay rate may be greater than the *Re* dependence of a flow field which is largely irrotational. At sensor 3, as shown in Figure 5.12 and Figure 5.16, at a wind direction of 305° (wind sector 31), measurements for both the large wall and the trailer show large discrepancies. This is also evident at the same point for the small wall (not shown). Checks indicate that although the uncertainty is relatively high at this point, it is not great enough to explain the discrepancy. The wind tunnel measurements are consistent and have been verified. The large velocity deficit measured at sensor 3 in the field may be caused by a flow feature that is not present in the wind tunnel. Further field investigation would be required to determine the nature and extent of this apparent dissimilarity between the two tests.

Table 5.4 - MAD of the wind tunnel compared to field results, for each sensor location

	R_V (% MAD)			R_I (% MAD)			
Sensor	Large Wall	Small Wall	Trailer	Large Wall	Small Wall	Trailer	
1	1.5%	2.6%	3.6%	13.3%	9.7%	14.5%	
2	5.6%	2.2%	6.3%	10.2%	5.0%	14.4%	
3	6.0%	4.1%	11.4%	13.4%	8.5%	22.3%	
4	13.9%	5.3%	5.2%	21.6%	16.4%	22.9%	
5	1.4%	1.6%	3.7%	5.9%	4.6%	9.1%	
6	4.6%	3.9%	4.9%	16.8%	7.4%	13.8%	
7	3.0%	1.9%	4.3%	5.4%	3.2%	6.7%	
8	1.3%	1.4%	3.3%	4.0%	2.7%	4.7%	
9	1.3%	1.7%	4.7%	8.0%	4.3%	9.2%	

Table 5.5 – MAD values for R_V and R_I for the large wall, small wall, and trailer

Obstacle	R_V (% MAD)	R_I (% MAD)	-
Large Wall	4.9%	11.6%	
Small Wall	2.9%	7.4%	•
Trailer	5.3%	13.1%	

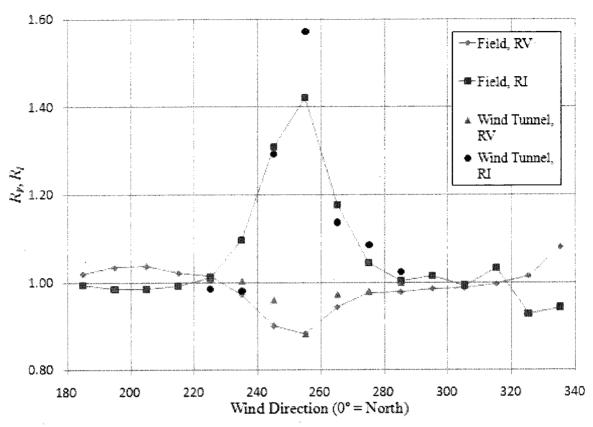


Figure 5.13 – Variation of R_V and R_I at an emometer 2, in the wake of the small wall

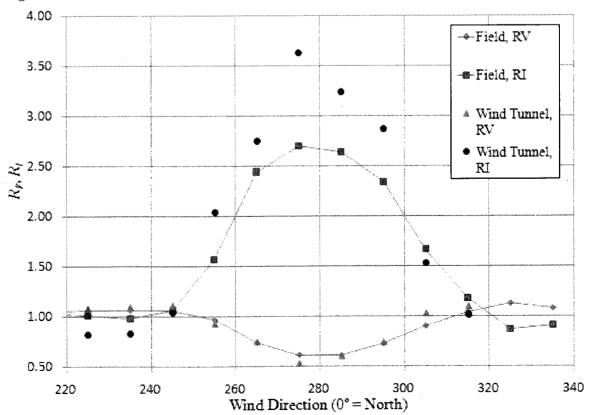


Figure 5.14 – Variation of R_V and R_I at an emometer 4, in the wake of the small wall

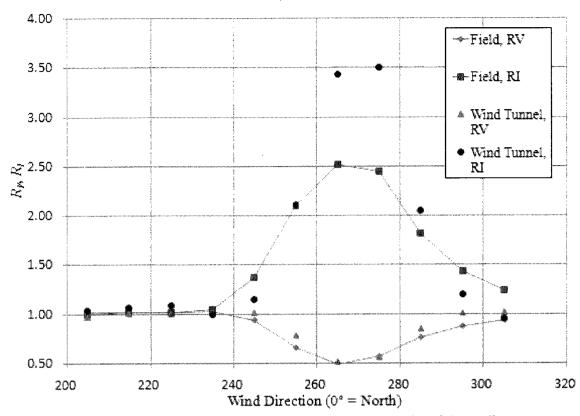


Figure 5.15 – Variation of R_V and R_I at an emometer 2, in the wake of the trailer

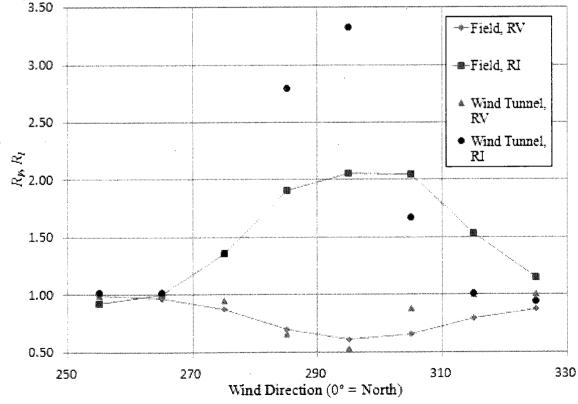


Figure 5.16 – Variation of R_V and R_I at an emometer 3, in the wake of the trailer

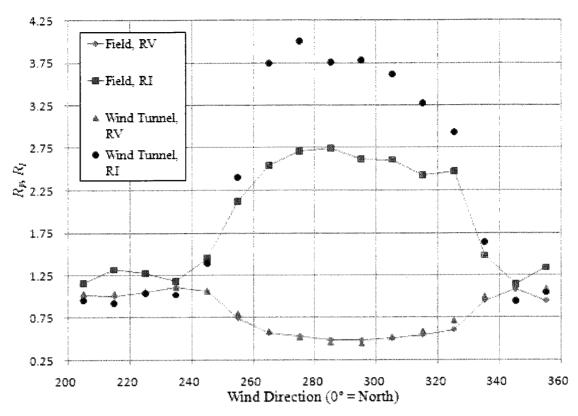


Figure 5.17 – Variation of R_V and R_I at an emometer 4, in the wake of the trailer

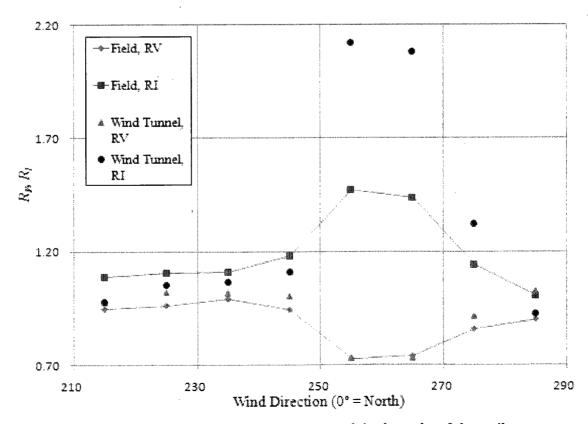


Figure 5.18 - Variation of R_V and R_I at an emometer 6, in the wake of the trailer

Typically, considering R_V , the trailer comparison showed the greatest discrepancy, followed closely by the large wall comparison. The small wall comparison showed much less difference between wind tunnel and field results. When the walls were used, sensors 1, 2, 3, 4, and 6 tended to show greater absolute difference than the other sensors. With the trailer in place, sensors 2, 3, and 4 showed greater absolute difference. Generalizing these results, it appears that absolute difference tends to be greater in locations with stronger wake effects. It is thought that in most cases, the absolute error is caused by the experimental uncertainties discussed in Chapter 5.2. When the obstacle does not have an effect on R_V , the same uncertainties may be present in both the sheltered and unsheltered measurements, causing much of the uncertainty to effectively cancel out. However, when an obstacle is in place, the magnitude of the experimental error may be different for the sheltered and unsheltered measurements, resulting in the observed disagreement. For example, assume that the height of the probe during a wind tunnel measurement was accidentally too great by 1 mm. This would be a source of experimental error. If the intended probe location experienced a stronger velocity deficit than the actual location, then the wind tunnel measurement would predict a higher R_F value than the field test. However, if the obstacle was not causing any velocity deficit at that point, then an R_V value of 1.00 would be found for both the wind tunnel and field tests, even though the probe in the wind tunnel was not in the correct location. This is only a simple example of how experimental error could cancel out; in reality, all probe locations in the wind tunnel were carefully controlled to be within 0.5 mm of the intended position, as discussed in Chapter 4.

It is also possible that sensors closer to the obstacles show greater discrepancies because of small geometric dissimilarities in the two tests. Snyder [28] reports that further away from a bluff body, small features will have less influence on the flow. This is intuitive as well; imperfections in the shape of these obstacles would have a larger effect on the flow closer to the obstacle, and a smaller effect further away. It is thought that this is part of the reason for the larger variation in absolute difference observed at closer anemometers, as seen in Table 5.4.

Based on Table 5.4, it appears that measurements made by the cup anemometers (sensors 5 to 9) were more closely reproduced in the wind tunnel than measurements made by sonic anemometers. However, it is thought that this is more due to distance and magnitude effects discussed above than any inherent bias in the sensor (recall the five cup anemometers in the wake were all located further away or at greater heights than the four sonic anemometers; see Table 5.1).

Virtually all of the above figures show a large discrepancy between turbulence intensity measurements made in the field and those made in the wind tunnel. When strong wake effects are present, R_I values in the wind tunnel are much greater than the corresponding field values. This is consistent with Lim et al. [29], who found that fluctuating quantities in the flow around a cube will depend on Re to a greater extent than non-fluctuating quantities. There are several other possible explanations for why this discrepancy is so large in some cases (such Figure 5.12, Figure 5.14, and Figure 5.17). It is expected that the field results would tend to underestimate the magnitude of any sheltering effects, because wind direction is more consistent in the wind tunnel than in the field. For some fraction of almost any sampling period, the wind will not be coming from the direction of the obstacle, and thus may not show the same constant decrease in velocity or increase in turbulence intensity. This directional effect should be minimal because the data was filtered by standard deviation of wind direction, but it may still play a role. A more probable reason for this large discrepancy is that 30 averaging sampling times were used in the field. Recall that the sampling time in the wind tunnel was roughly 32.8 seconds. In a more 'true' simulation, the sampling time would have been scaled as well (as discussed above, it was necessary to compromise between competing criteria). The use of an averaging time of 10 minutes or 1 hour would likely result in greater turbulence intensity values. If more field data were available, the use of a 10 minute averaging period and the same stringent filtering criteria might provide enough data samples to attain convergence for the wind directions of interest. It may be possible to empirically correlate turbulence intensity in the wind tunnel to turbulence

intensity in the field, but at this point there is not sufficient data to develop such a relationship, and in any case, it would likely only apply to this set of experiments.

Regarding far wake persistence, measurements from the field experiment were not taken nearly as far downwind as measurements made in the wind tunnel, so wake persistence cannot be directly confirmed for a full scale situation. Hansen et al. [24] suggest that dependence of vortex behaviour on Re may be different than Re dependence for a wake without vortices. Figure 5.18 shows R_V roughly 10 h downwind of the trailer, which has an AR of 4.73. In the field test, a large velocity deficit was measured for wind from 255° and 265°, which agreed extremely well with wind tunnel measurements. Figure 5.1 shows that the orientation of the field obstacle for these wind directions is roughly 30°. This field result is strong evidence that in the full scale case, vortex behaviour will in fact be similar to that seen in the wind tunnel.

To summarize, aside from the discrepancies discussed, the field data for R_V matches the wind tunnel data reasonably well. R_I values measured in the wind tunnel were typically greater than those measured in the field. This is evidence that Re independence is valid for mean quantities in the far wake, but not for fluctuating quantities, at least in some cases. In general, a model developed from BLWT data can potentially make R_V predictions of acceptable accuracy, but R_I will tend to be overestimated, in some cases by a large margin. This effectively makes the model conservative when making predictions regarding the turbulence wake of an obstacle. NN training with actual full scale data would be preferable but is not feasible, as discussed in Chapter 3.

5.6 Distribution of Wind Speed

To make accurate predictions of a turbine's energy output over a given period of time, the probability density function (PDF) of wind speed at the site must be considered. Energy output predictions based solely on the mean wind speed will not be accurate, since power density is proportional to velocity to the third power. The Weibull distribution is a commonly used PDF for

wind speed [14]. At a sheltered location, the Weibull distribution will be different from that at an unsheltered point. Figure 5.19 shows how the PDF at sensor 3 compares to the PDF at sensor 1, when the wind is coming from sector 24 (between 230° and 240°, chosen because it had the most available data, 4713 samples). In this case, sensor 1 is sheltered by the trailer, while sensor 3 is unsheltered. Data samples used to create this figure were not filtered for wind speed or standard deviation of wind direction. Also shown in Figure 5.19 are best fit Weibull distributions for both locations. It can be seen that at sensor 1, greater wind speeds have a much lower probability of occurrence, as expected, since the anemometer at that location is sheltered by the trailer.

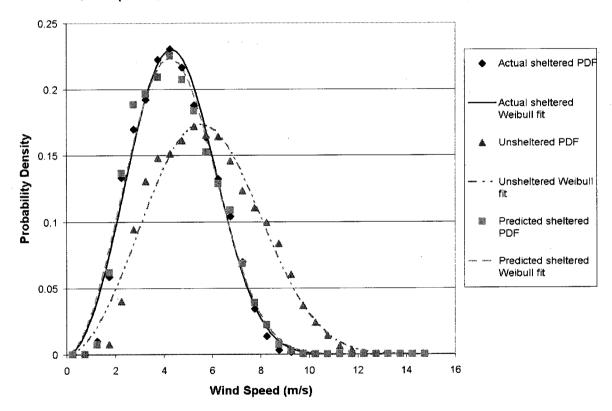


Figure 5.19 - PDFs and Weibull fits of unsheltered data, sheltered data, and predicted data

Using the methods described previously, an R_V value of 0.78 was determined for sensor 1, when the wind was coming from sector 24 and data was not filtered. Recall that R_V is essentially a correction factor. To try to predict the effect of sheltering on the PDF of wind speed, all wind speeds measured at the unsheltered sensor were multiplied by this correction factor, creating a

new set of 'sheltered' wind speeds. From this new data set, the PDF was calculated; this is also shown in Figure 5.19.

The predicted sheltered PDF is very close to the measured sheltered PDF. This result is very significant because it means that the wind speed probability distribution at a sheltered point can be predicted based on i) the unsheltered PDF, which is given in most wind maps, and ii) a single correction value for that point, R_V . This result is also strong evidence for Re independence of R_V , since it implies that the magnitude of the shelter factor is independent of wind speed. Similar calculations at other points confirm that this finding can be applied to obtain an accurate estimate of any sheltered PDF.

Recall that the overall R_V value at each sensor location was found simply by calculating the mean of all available samples, $\overline{R_V}$. It is thought that a method of determining the overall R_V value based on PDFs may result in better field values of mean wind speed when few samples are available. At both the sheltered and unsheltered sensor, the Weibull curve of best fit could be determined based on the (limited) number of samples available. From this curve, using methods described by Manwell [14], the mean wind speed can be predicted. R_V could then be calculated as the ratio of the two mean wind speeds.

6.0 wakeNET model

This chapter describes the creation of the new model, wakeNET, which was developed using NNs. The choice of this modeling approach is explained in Chapter 2. The development of the new model is first discussed, followed by an evaluation of its performance. It should be pointed out that the model consists of two distinct NNs; one which predicts R_V and one which predicts R_V . Both NNs are referred to throughout this Chapter.

6.1 Training Data

All NN training data was generated from wind tunnel experiments. The training data consists of a large set of known points. Each point consists of a value for each model input and output. Three example points are shown in Table 6.1.

Table 6.1 – Example data points

x	У	z	а	AR	PR	RA	R_V	R_I
15.00	1.71	-3	22.5	4	1	0	0.90	1.56
3	0.50	1	0	2	1	15	0.74	2.06
8.52	1.13	3.02	-27.5	4.73	0.83	0	0.73	2.08

Table 4.1 describes all model obstacles used in the wind tunnel. Table 6.2 gives the number of points that were measured to characterize the flow around each training obstacle. Also shown are the total number of NN training points obtained, directly or indirectly, for each obstacle.

The number of points measured with each obstacle is the same as was given in Table 4.2. Notice that no unique measurements were taken for the last seven obstacles listed. As explained below (see Figure 6.2), training data for these obstacles was adapted from training data for other obstacles.

Table 6.2 - Measurements made and NN training points used for each obstacle

Obstacle	Number of	Number of	Number of Training		
	Measured Points	Assumed Points	Data Points		
0.5-1 block	328	1912	2240		
Cube	632	5888	6520		
2-1 block	584	2920	3504		
2-1-15 block	330	1870	2200		
2-1-30 block	330	1870	2200		
2-1-45 block	330	3188	3518		
4-1 block	669	3205	3874		
4-2 block	. 306	306	612		
6-1 block	70	70	140		
9-1 block	268	1616	1884		
Two-dimensional wall	56	154	210		
Large Wall	. 60	60	120		
Small Wall	60	60	120		
Hansen block	44	44	88		
1-0.5 block	0	2240	2240		
1-2 block	0	5604	5604		
1-4 block	0	3874	3874		
1-9 block	0	1884	1884		
1-6 block	0	140	140		
2-4 block	0	612	612		
Reverse Hansen block	0	88	88		
Total	4067	37605	41672		

The third column of Table 6.2 shows how many points were assumed for each obstacle, which represents the majority of the training data. By making assumptions regarding the values of R_V and R_I at certain points in the wake, the training data set was greatly expanded. Three methods were used to make these assumptions. The first was the use of boundary conditions for extreme values in the wake. For example, according to the U.S. Department of Energy, effects from an obstacle will be evident at up to two heights upwind from the obstacle's position [47]. This corresponds to an x position of -2. For all obstacles, R_V and R_I were both specified to have a value of 1.00 at all points where x = -2. Similarly, very far laterally, R_V and R_I will both have a value of 1.00. The exact definition of 'very far laterally' varies with x, y, and each obstacle. It was not always determined directly in the wind tunnel. If necessary, the z position at which wake effects are not present would be extrapolated based on R_V and R_I values at the furthest known z positions. It is expected that these extrapolations are typically overestimates. Using this approach, boundary conditions were created for most obstacles. For some obstacles it was difficult to predict where boundary conditions should be; it was felt better not to make any predictions in these cases. A large number of the assumed points are boundary conditions.

Assumed points were also created using symmetry. An obstacle wake will be asymmetrical anytime the model is oriented at an angle where the geometry presented to the wind is asymmetrical (for blocks, this means that the wake will be asymmetrical for any wind angles except for the special cases of 0° and 90°). This is shown in Section 6.3. Symmetry can still be used here, however, by changing the sign of the model orientation a and the lateral position a, as shown in Figure 6.1. The case on the left is symmetric to the case on the right. All other things being equal, the velocity deficit measured at point A must be the same as the velocity deficit measured at point B. In terms of generating training data, the output values at A and B will be identical. The inputs will have the same magnitude a and a values, but of opposite sign.

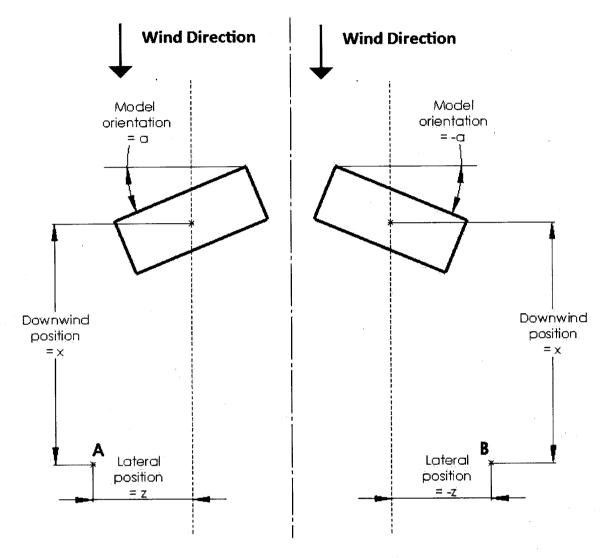


Figure 6.1 – Use of symmetry to create training data

The third way in which training points were generated came from the realization that a block with AR of 1 and PR of 4 is the same as a block with AR of 4 and PR of 1, when the latter is rotated 90°. It is emphasized that this is only true for roof angles of 0°, and as such it was only applied in appropriate cases. Any point in the wake of a flat block can be used to generate a duplicate point by swapping AR and PR, making the appropriate change to model angle, and using the same output values for R_V and R_I . Figure 6.2 illustrates this duplication. Phantom lines show the placement of the obstacle when the orientation angle is 0°. Symmetry was also applied to points duplicated in this manner, meaning that a typical single measured point in a wake could result in four unique NN training points.

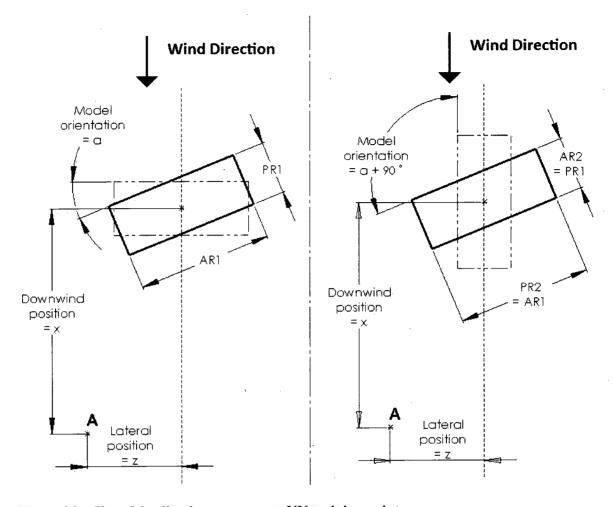


Figure 6.2 – Use of duplication to generate NN training points.

Using the three techniques described above, the number of NN training points was expanded from the measured number of points 4067, to 41672. Another approach was considered in which no assumed points were used to train the NN. The same assumed points would be generated, but they would be applied after NN predictions, during post-processing of the model outputs. However, it was decided that training the NN with all points, assumed or not, was a better approach. Conceptually, it was thought that the use of more points would allow the NN to learn a relationship between the inputs and outputs that more closely resembles the 'true' relationship, resulting in better predictions all around. As well, the use of the duplicate, rotated points eliminates (or at least reduces) the need to conduct a separate investigation into the effect of *PR*, since this is done as part of the investigation of effects of *AR*. Lastly, using all the points to

train the model simplifies pre- and post-processing of model inputs and outputs when the model is eventually implemented into a software tool.

6.2 Creation and Development

Using a NN to determine relationships between variables is a form of non-linear regression. For this project, a feedforward, backpropogation NN was used. Feedforward refers to the direction of information flow within the network; there are no feedback loops.

Backpropogation refers to the learning method used, where neuron weights and biases are updated based on the error of the NN outputs. This type of NN is well suited for function approximation; in this case, the function has 7 inputs and a single output. The MATLAB Neural Network Toolbox was used exclusively in this project; the reference manual [34] proved very useful. There are two main objectives for the NN; it must make accurate predictions when fed training data inputs, and it must make accurate predictions when it is fed inputs that were not part of the training data. This characteristic is referred to as generalization.

6.2.1 Overview of NN Development

Recall that the goal of the model is to predict the effects of an obstacle at points in the flow field relative to a base "open field" condition. As stated above, the two quantities which are directly predicted by wakeNET are R_V , defined in Equation 3.1, and R_I , defined in Equation 3.5. It was found that model performance is greatly improved if two distinct NNs are used; one to predict R_V , and one which predicts R_I . This is thought to be because the weights and biases in each neuron are better able to adapt to predicting one output rather than two.

wakeNET was developed over time by increasing the complexity of the network incrementally, as more wind tunnel data was collected. Each time the network was 'retrained', an entirely new network was created based on all the training data to date. This is known as batch training. During the initial stages of this project, a simple model was created in the form of a NN

that could predict the velocity ratio at any point (x, y, z) in the wake of a cube, with the front face of the cube normal to the dominant flow direction. This initial NN had three inputs, a single output, and a very limited scope, since it was only valid for a single obstacle (a cube) at a single orientation. Once this network was successfully trained, the orientation of the cube was added as an input parameter, and the appropriate training data was collected in the wind tunnel. At this point, the network was retrained. Once the NN was capable of accurately predicting the velocity ratio in the wake as a function of these four inputs, AR and then PR were added as inputs. Finally, once the NN was well trained for those six inputs, the last input, RA, was added. Extensive wind tunnel testing was conducted to obtain the training data points described in the previous section. Before new data was used for training, the generality of the network was evaluated by using the best existing NN to predict what the wind tunnel measurements would be before they were used as training data. This provided an idea of whether or not further wind tunnel measurements were needed for a particular obstacle. Once the NN was capable of accurately predicting the value of new measurements before they were used as training data, it was considered to be complete for that obstacle. Further training would improve the network slightly but is not essential to make accurate predictions for the obstacles used. This incremental approach was not strictly necessary; however, it proved very useful in learning how best to train a NN and what level of accuracy and generality can be expected.

6.2.2 NN Description

There are several key NN characteristics and features that must be specified when a network is created, before it can be trained. The choice of these characteristics and features determines how well the NN can reproduce training data, and how well it can generalize results to make accurate predictions for new cases. When creating a new NN, it is necessary to specify the number of layers of neurons as well as the number of neurons in each layer. As the relationship of interest becomes more complex, it is generally necessary to increase the number of neurons in

order to continue to make accurate predictions. This can be thought of as increasing the power of the network. The 'final' NN, as described above, contained the input layer, two hidden layers, and the output layer. Hidden refers to the fact that they are essentially 'inside' the NN. The first and second hidden layers had 40 and 20 hidden neurons, respectively. Within each neuron, it is necessary to specify the transfer function to use. Here, the tan-sigmoid transfer function was used in both hidden layers, while a purely linear transfer function was used in the output layer.

One of the most important aspects to consider when training a NN is the specific training algorithm to use. The MATLAB NN toolbox contains many preprogrammed training algorithms. Based on trial and error testing, the fastest and most accurate training algorithm for this application was found to be the Levenberg-Marquardt training function, which is often the fastest backpropogation algorithm in the NN Toolbox [34].

Network performance is evaluated based on a specific performance function (PF), which must be defined prior to training. From the perspective of the training function, the goal of training is to reduce the output of the PF. As the NN is trained, the weights and biases of each neuron are updated based on the negative of the gradient of the PF [34]. The choice of PF will strongly affect how neurons are modified. The use of different PFs can result in very different final NNs, even when the same training data is used.

Several quantities are defined to evaluate accuracy and generality. The error e_i at point i is defined in Equation 6.1 as the difference between the target t_i (here, R_V or R_l , as measured in the wind tunnel) and the NN prediction at that point, y_i . The mean squared error (MSE) is defined in Equation 6.2 as the average of the error squared. N is the total number of training data points.

$$e_i = t_i - y_i \tag{6.1}$$

$$MSE = \frac{1}{N} \sum_{i=1}^{N} (e_i)^2$$
 (6.2)

$$MAE = \frac{1}{N} \sum_{i=1}^{N} \left| e_i \right| \tag{6.3}$$

The mean absolute error (MAE) is defined in Equation 6.3 as the mean of the absolute value of the error. MSE was chosen over MAE to evaluate error during training because MSE will weight large errors more heavily. Another important quantity is the mean square weight (MSW), defined in Equation 6.4 as the mean of the network weights squared. n is the total number of weights in the network, and w_j is the value of weight j. Smaller weights and biases force the network response to be smoother and less likely to overfit [34]. A lower MSW typically means that network generalization is better.

$$MSW = \frac{1}{n} \sum_{j=1}^{n} \left(w_j \right)^2$$
 (6.4)

The PF F used in this project uses a technique called Bayesian regularization (BR). F is a combination of the MSE and the MSW, as defined in Equation 6.5. Recall that the purpose of training is to minimize the value of the PF. By considering both terms, the network will tend to become more accurate (by reducing the MSE) as well as more general (by reducing the MSW).

$$F = \gamma MSE + (1 - \gamma)MSW \tag{6.5}$$

 γ is the performance ratio, and defines the weighting of the two terms. The BR training function used employs the Levenberg-Marquardt algorithm and the BR PF, Equation 6.5. An optimal value for γ is determined automatically. Another advantage of the BR training function is that it provides a measure of how many network parameters (weights and biases) are being effectively used by the network [34]. This was used to make sure that the network is an appropriate size. The final network had 1401 parameters, 1390 of which were being effectively used. The number of model parameters is the sum of the number of weights and biases in the model. All NNs reported here were trained using the BR training function.

6.2.3 Pre-processing

It proved necessary to pre-process all data before training to improve the accuracy and generality of the network. For example, adding obstacle orientation as a model input was initially

done by simply adding another input to the NN, which was the angle of the obstacle relative to the wind direction. However, even with extensive training time and a large NN, the network was not able to learn the relationship between model orientation and R_{ν} to a high degree of accuracy. It was necessary to replace model orientation angle as an input with two new inputs; i) the sine and ii) the cosine of the model orientation angle. These inputs can be thought of as the lateral component of the orientation angle, and the longitudinal (or downwind) component of the orientation angle. This change greatly improved network performance and was essential to achieving the final NN.

Similarly, the AR of the obstacle was represented by three inputs. The use of three inputs improved NN performance compared to using just AR. The three inputs are i) the AR, ii) the lateral distance between the transverse position, z, and the close lateral edge of the obstacle, and iii) the lateral distance between the transverse position, z, and the far lateral edge of the obstacle. The latter two inputs were selected based on the idea that they have a very direct influence on R_V at the point of interest. The lateral distances from the point of interest to the edge of the wake greatly affect how much momentum is transported to the point from outside the wake. AR and z both indirectly affect this distance, and in fact they fully define it, but by using the distances themselves as NN inputs, it was found that the NN was generally better able to predict R_V (and R_I) at the point of interest. Use of these two supplementary inputs also adds an additional way in which information about the model orientation can affect predictions, since the lateral distances are a function of orientation angle.

PR was also represented as an input by three values, which are i) the PR, ii) the longitudinal distance between the downwind position, x, and the most upwind edge of the obstacle, and iii) the longitudinal distance between the downwind position, x, and the most rearward edge of the obstacle. This also improved model performance compared to just using PR as an input, for the same reasons described above for AR.

Similarly, RA was replaced by two values; the sine and cosine of RA, representing the vertical and longitudinal components of the top roof surface. To summarize, as a result of preprocessing, the final version of the NN has thirteen inputs, which are all derived from the seven model inputs.

6.2.4 Post-Processing

No post-processing was necessary, since the NN outputs are the quantities of interest, R_V and R_I . Once training is complete, the set of weights and biases can be exported and used to recreate the NN, if desired. All that is required to reproduce the NN are the network parameter values; there are 1401 for each NN.

6.2.5 Learning

The purpose of training is to reduce the value of the performance function. Typically, at the start of training, the MSE is very high, while the MSW is very low. The 41672 available training points were divided into two separate data sets. The training data set consisted of a random 90% of the available data. The NN is trained exclusively with this data. The validation data set consisted of the remaining 10%, which was not used to train the network. Validation of the NN will be based partly on the MSE of this data set. However, this validation data set is inherently limited in a way, because while it will present new input points to the network, it will not present any new values for AR, PR, RA, or a. To remedy this, an additional data set of 191 points was created by taking wind tunnel measurements in the wakes of three new obstacles, at new orientations. These obstacles are described in Table 4.1. This is referred to as the 'pure' validation data set, since no training data had these values of AR, PR, RA, or model orientation. Unique x, y, and z locations were used as well. This makes the pure validation data the most difficult set to predict. A subset of the pure validation data was created that consisted of the 88 points located in the far wake (here defined as $x \ge 5$), and above the height of the obstacle ($y \ge 1$), since this is the

main region of interest here. This subset is expected to be somewhat easier to predict than the entire pure validation set, since R_V and R_I in the far wake are expected to be easier to predict. Figure 6.3 shows how the MSE of these four data sets varied over a typical training run. Note that this does not show the MSE of the final NNs; this is only an example of the training process.

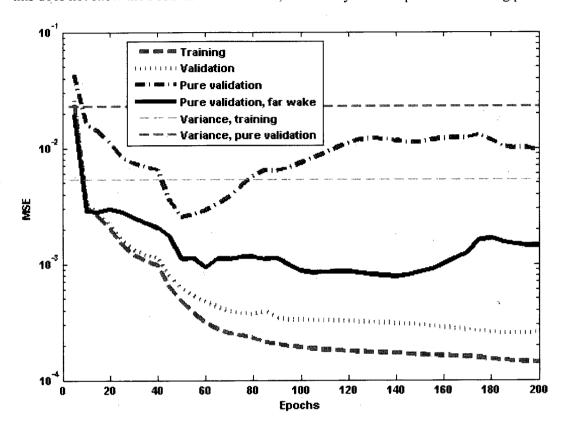


Figure 6.3 - Example MSE of four data sets during a training session, and their variances

Epoch refers to the number of times that the entire training data set has been fed through the NN (after each epoch, network parameters are adjusted, and the process starts again). Also shown are the variance of the combined training and validation data set, and the variance of the pure validation data set. These statistical quantities can also be thought of as the MSE that would be obtained if all points were predicted to be equal to the average value of the data set. The fact that the MSE curves are lower than the variance shows that learning has occurred.

As expected, the training data shows the lowest MSE. The validation data also has a very low MSE, on the same order of magnitude as the training data. The pure validation data set

showed the greatest error by far, but it appears to perform much better in the far wake than the near wake. The MSE of the far wake data set is on the order of 10⁻³, which will typically still result in good predictions, as explained below.

When a network is first created, all weight and bias values are initialized randomly. These random values will have an effect on the NN that will result from training. Some sets of random values will be much more suited than others to lead to the creation of a good NN. This means that it was necessary to train and compare many networks in order to obtain the best possible result. As well, it was not necessary to train each network to 200 epochs. As seen in Figure 6.3, the value of the MSE for the pure validation data set reached a minimum well before 200 epochs of training. Based on Figure 6.3, the best network might be obtained after just 60 epochs, depending on the importance assigned to each MSE. The final R_V and R_I NNs were trained to 200 and 95 epochs, respectively, to obtain the MSE values given in the next section.

6.3 Evaluation of Accuracy and Generality

Using the techniques described above, and the training data collected in the wind tunnel, two distinct NNs were created: one which predicted R_V , and another which predicted R_I . It was found that wakeNET predictions are greatly improved if the model consists of two totally separate NNs; one which predicts R_V and one which predicts R_I . A single network can be created that is capable of outputting both parameters, but it was found that error is reduced by using two networks instead of one. Two final NNs were selected from the many that were trained. The two selected NNs had an optimal combination of the four MSE values, shown in Table 6.3. MAE is also given in percentage form.

A series of plots was created to compare model predictions to wind tunnel data. In each of these plots, a single model input is varied, while all others are held constant. Figure 6.4 shows how model predictions of a) R_V and b) R_I compare to the wind tunnel data when x is varied, and all other values are held constant. Constant values are specified in the caption. Similarly, Figure

6.5, Figure 6.6, Figure 6.7, Figure 6.8, Figure 6.9, and Figure 6.10 show how the wind tunnel data compares to NN predictions for a) R_V and b) R_I ratios when y, z, a, AR, PR, and RA are varied, respectively. It should be noted that wind tunnel measurements shown in the plots are not always at exactly the same point as the NN predictions; rather, they are closest available measurements.

Table 6.3 – MSE and MAE of the final R_V and R_I NNs

	R_V		R_I		
Data Set	MSE	MAE	MSE	MAE	
Training	1.56·10 ⁻⁴	0.8%	2.85·10 ⁻³	2.6%	
Validation	2.99·10-4	0.9%	4.54·10 ⁻³	2.9%	
Pure Validation	1.42·10 ⁻³	3.1%	4.82·10 ⁻²	11.0%	
Pure Validation,					
far wake	2.98·10 ⁻⁴	1.3%	5.72·10 ⁻³	5.3%	

In the cases shown, the NNs appear to be best at predicting the effects of changing location in the wake, as seen in Figure 6.4a, Figure 6.5a, and Figure 6.6a. In Figure 6.4b, it is seen that near the obstacle, around x = 2, NN predictions of R_l are very disjointed and likely incorrect. These poor predictions are thought to be caused by the large amount of variation in the training data for this region, for this and other obstacles. The NN is trying to predict relatively large changes in output when input values change only slightly. It is thought that factors which have an insignificant effect on the far wake region are much more important closer to the obstacle; since these other factors are not taken into account by the model, the NNs are unable to learn an appropriate relationship. The magnitude of the peak observed at x = 14 appears to be too great. However, the location of this peak appears to be roughly correct.

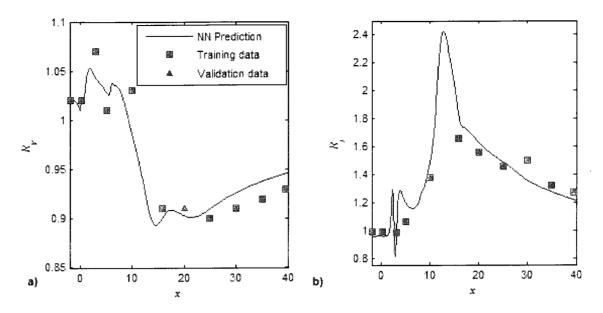


Figure 6.4 – Comparison of sample model predictions, training data, and validation data, with varying x. Other parameters are held constant at y = 3.2, z = 0, $a = 0^{\circ}$, AR = 9, PR = 1, RA = 0.

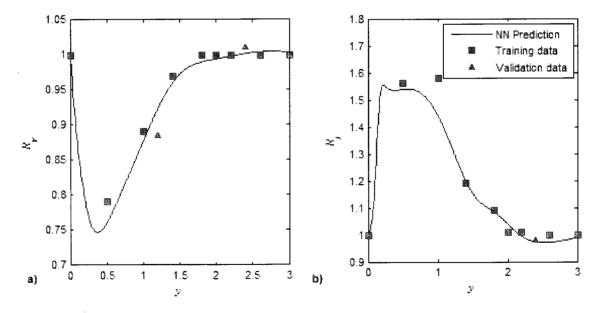


Figure 6.5 – Comparison of sample model predictions, training data, and validation data, with varying y. Other parameters are held constant at x = 5, z = 1.42, $a = -22.5^{\circ}$, AR = 2, PR = 1, RA = 0.

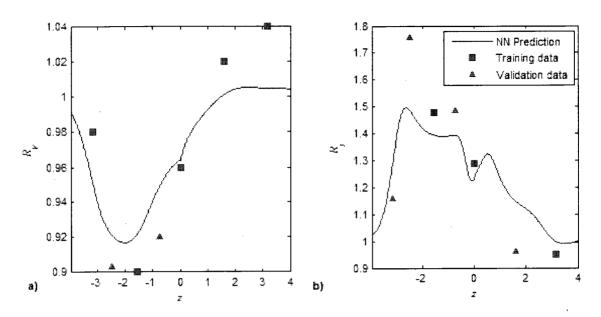


Figure 6.6 – Comparison of sample model predictions, training data, and validation data, with varying z. Other parameters are held constant at x = 10, y = 2, $a = 22.5^{\circ}$, AR = 4, PR = 1, RA = 0.

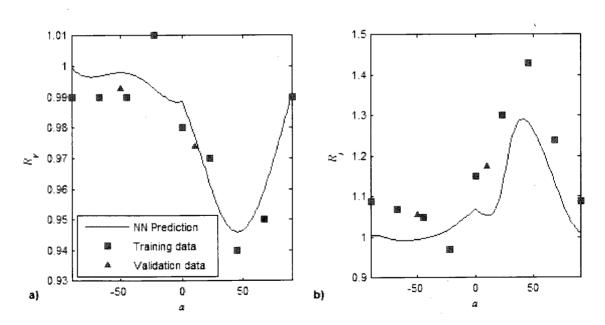


Figure 6.7 – Comparison of sample model predictions, training data, and validation data, with varying a. Other parameters are held constant at x = 10, y = 1.8, z = -1.94, AR = 2, PR = 1, RA = 0.

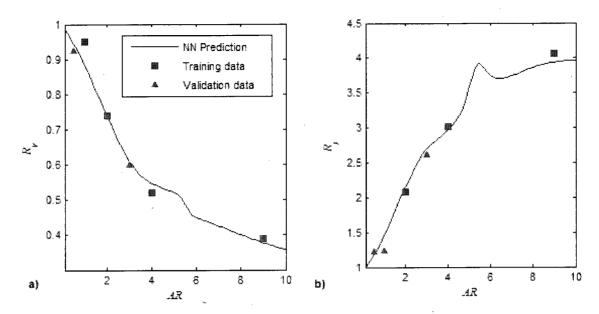


Figure 6.8 – Comparison of sample model predictions, training data, and validation data, with varying AR. Other parameters are held constant at x = 5, y = 1, z = 0, a = 0, PR = 1, RA = 0.

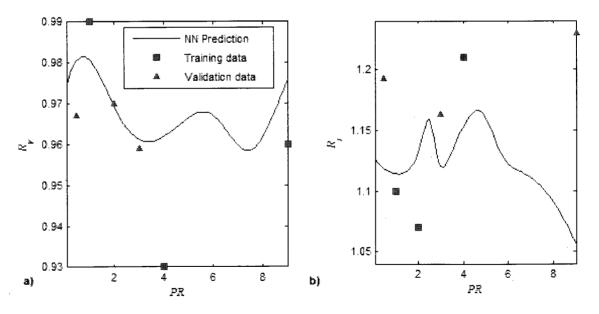


Figure 6.9 – Comparison of sample model predictions, training data, and validation data, with varying PR. Other parameters are held constant at x = 10, y = 1.4, z = 0, a = 0, AR = 1, RA = 0.

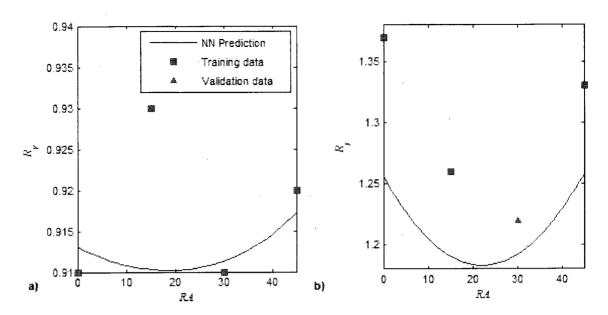


Figure 6.10 – Comparison of sample model predictions, training data, and validation data, with varying RA. Other parameters are held constant at x = 15.75, y = 1.4, z = -2.20, a = 45, AR = 2, PR = 1.

In general, wakeNET has some difficulty predicting correct peak R_l values, as seen in Figure 6.7b, where at 45°, the R_l prediction is off by nearly 12%. The effect of orientation angle on R_V is predicted much more accurately, as in Figure 6.7a, where the maximum error is less than 2%. The effects of AR on both R_V and R_l are well predicted, as evidenced in Figure 6.8. In Figure 6.6b, the NN appears to be trying to predict the R_l value at z = -3.17, which is a validation point. Of course, the validation points are not being used to train the model, by definition. It only appears so because some training points that were used are only slightly different than the validation point. These training points are not shown in the figures (since the figures only show the variation of a single input). Figure 6.9b shows that the model is not great at making predictions of R_l for some values of PR, such as 9, where it is off by nearly 20%. It is emphasized that this is not true for all points in the wake of the block with a PR of 9; this is only a single example point. Predictions of R_V in Figure 6.10a show little change in predicted values with RA, but all predictions are within 2% of measured values. RA does not appear to have a significant

effect on R_V at this region of the wake. Figure 6.10b shows that again, R_I predictions are not quite as good as R_V predictions, but accuracy is still satisfactory.

Several of the predicted curves (such as Figure 6.4a, Figure 6.6b, and Figure 6.9a and b) contain peaks and troughs that seem to be out of place. In some cases, the NN predictions even match the training data reasonably well, but it is thought unlikely that these peaks and troughs represent true wind conditions. This indicates that the NNs may be slightly over trained, even though the training function used, described previously, is intended to prevent overtraining. This also may simply be due to scatter in the data, since the magnitudes of the peaks and troughs are generally fairly small.

Overall, R_V is predicted more accurately than R_I , as seen in the difference in MSE and MAE of the two NNs. It is thought that this is because turbulence intensity measurements made in the wind tunnel showed greater scatter than mean velocity measurements; this supports the findings of the uncertainty analysis, which estimated that R_I has a greater uncertainty than R_V .

6.4 Validation

This section describes the validation carried out of the wakeNET model, which consists of comparing model predictions to experimental data from this study and others. Aside from a few exceptions, which are pointed out in the text, all of the experimental data shown in this section represents new sets of input that were not used to train wakeNET. To assess the performance of wakeNET compared to existing models, wakeNET predictions are compared to predictions from Taylor and Salmon's model [30] and Perera's model [27], as well as current and reference wind tunnel data. Then, to assess generality, predictions are compared to wind tunnel data for several new obstacles that were not used during training. To assess wakeNET performance in the above obstacle region, predictions are compared to wind tunnel and field results from literature. Lastly, model predictions are compared to field data from the current study; specifically, all

measurements made in the wake of the trailer. This is an important test of the applicability of wakeNET to a new, full scale case, which is the ultimate goal for the model.

6.4.1 Comparison to Existing Models

Figure 6.11 shows results for the lateral R_V profile in the wake of Hansen's block (described in Table 4.1) at x = 7.55, y = 0.94. It is pointed out that current wind tunnel results shown in Figure 6.11, Figure 6.12, Figure 6.13, and Figure 6.14 were used as training data for the NNs. Hansen et al.'s wind tunnel results [24] predict slightly greater velocity deficits than those measured as part of this study, especially in the center of the wake, but overall the agreement is reasonably good. wakeNET predictions are very similar to current wind tunnel data and predictions made by Taylor and Salmon's model [30]. Perera's model greatly underestimates R_V , as was seen in Chapter 4. Both sets of wind tunnel data show strong symmetry, which is expected, since the obstacle is symmetrical at this orientation.

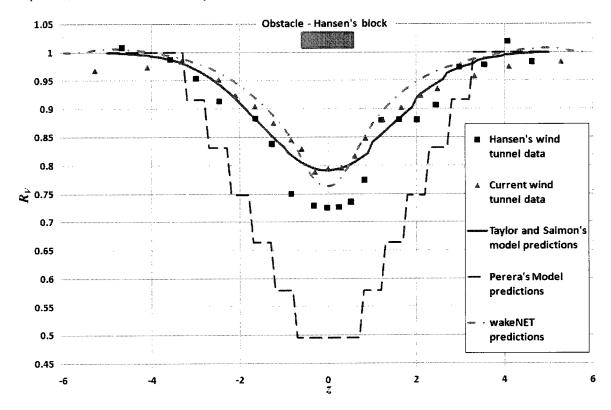


Figure 6.11 – Lateral R_V profiles in the wake of Hansen's block, at x = 7.55, y = 0.94, $a = 0^\circ$.

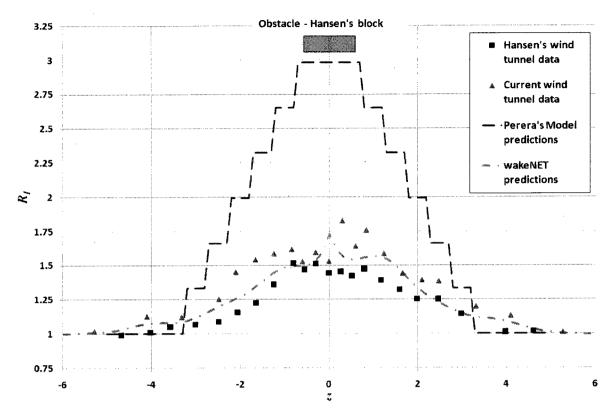


Figure 6.12 – Lateral R_I profiles in the wake of Hansen's block at x = 7.55, y = 0.94, $a = 0^{\circ}$.

Figure 6.12 contains lateral R_l profiles in the wake of Hansen's block at x = 7.55, y = 0.94. Again, wakeNET predictions are fairly similar to current wind tunnel data, although at some points, model predictions appear to be more similar to measurements made by Hansen et al. [24] than current wind tunnel results. R_l predictions are typically greater than that measured by Hansen et al., although there appears to be a great deal of scatter. Profiles are roughly symmetrical. Recall that Perera's model predictions are based on an empirical relationship for the normal stress excess in the wake of a two-dimensional fence, as described in Chapter 2. Using Perera's model in this way leads to large over predictions of turbulence intensity, compared to wind tunnel data from this study as well as data from Hansen et al [24].

The block used by Hansen et al. was rotated by 47° and lateral profiles were measured at x = 7.17, y = 0.94. Figure 6.13 and Figure 6.14 show the resulting R_V and R_I profiles, respectively. Both sets of wind tunnel data predict that the maximum velocity deficit occurs nearly 2 h from the obstacle centerline; this is a very important result. wakeNET is able to predict this feature

accurately, in terms of both the location and magnitude of the peak. Taylor and Salmon's model is unable to predict either the location or the magnitude of the maximum velocity deficit. Their assumed Gaussian lateral similarity profile is no longer valid; the wake is clearly not symmetrical about z = 0. Flow visualization by Hansen et al. showed strong vortex formation off the leading edge of the building, when the building is at an angle to the wind; Taylor and Salmon's model does not take effects from vortices into account. Current wind tunnel measurements at other orientation angles confirm that the form of the lateral R_V profile is highly dependent on the orientation of the obstacle, and that the wake is only symmetrical when the obstacle is symmetrical. Another example of an asymmetrical lateral profile can be seen in Figure 6.6. Although the block itself is symmetrical, at most orientations it is not presenting symmetrical geometry to the wind. More generally, it can be stated that the forms of (possibly self-similar) lateral R_V and R_I profiles are dependent on the obstacle's geometry, as presented to the wind direction. wakeNET is able to accurately predict these asymmetrical profiles, since it is based entirely on measured wind tunnel data. It is also observed that the mean wind speed on the centre line is nearly fully recovered, and in fact, Hansen et al. [24] showed an excess of nearly 5%. Both Perera's model and Taylor and Salmon's model predict that the mean wind speed will be at a minimum on the centerline, which is clearly not the case.

Figure 6.14 shows that the location of maximum turbulence intensity excess in the wake is also roughly 2 h from the centre line, near the same location as the maximum velocity deficit. wakeNET predictions follow current wind tunnel data. However, current results show greater turbulence intensity ratios than were measured by Hansen et al. [24]. Still, the trends are very similar.

The validity of wakeNET is strongly related to the validity of the current wind tunnel experiments. The same can be said about the scope of wakeNET; the range of cases to which the model can be successfully applied is inherently related to the range of cases that are represented by the BLWT simulation. Recall that all current wind tunnel tests used the same simulated ABL,

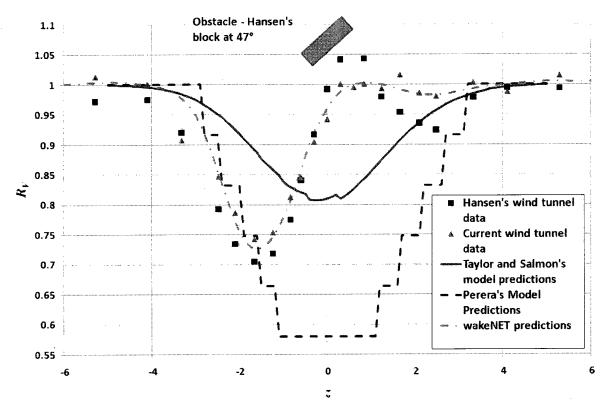


Figure 6.13 – Lateral R_V profiles in the wake of Hansen's block at x = 7.55, y = 0.94, $a = 47^\circ$.

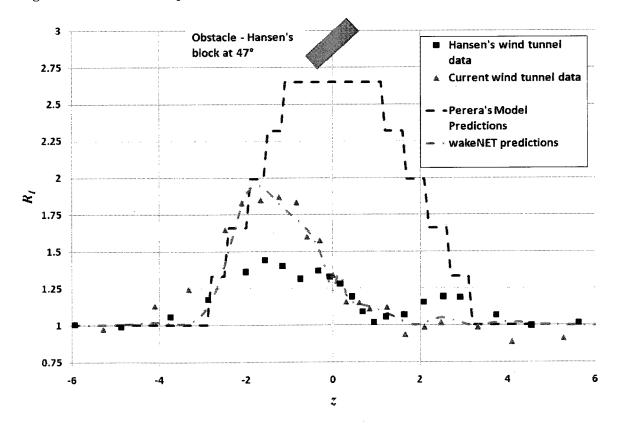


Figure 6.14 – Lateral R_I profiles in the wake of Hansen's block at x = 7.55, y = 0.94, $a = 47^\circ$.

described in Chapter 4. However, an obstacle in the actual ABL will experience a range of incoming flow characteristics. It is important to consider how changes in the ABL affect the wake of an obstacle, and by association, the accuracy of predictions made by wakeNET. It was previously assumed that changes in the ABL will not significantly affect the structure of the far wake, over the range of changes commonly seen in a rural area. Although the effects of changing the ABL were not directly investigated in this thesis, they can be investigated by considering that each of the reference results used a unique simulated ABL. While this investigation provides some insight, future work could include a more systematic study of the effects of changes in the ABL on the wake region.

Wind tunnel measurements shown in the four figures above were all obtained in the wakes of a flat block $(RA = 0^\circ)$ with the same AR and PR as that used by Hansen et al. [24]. However, as seen in Table 4.3, the tests used different simulated ABLs. Although there was some discrepancy in the results of the two tests, overall, R_V results agreed quite well, even with differences in Re, block height, the value of h/δ , free stream wind speed $U\infty$, upwind shear coefficient α , and upwind turbulence intensity. While it is possible that the observed discrepancies in the results are simply due to the experimental uncertainties described in Chapter 4, it is thought more likely that the differences present in Figure 6.11 to Figure 6.14 are associated with the differences in the ABLs. The shear coefficient used by Hansen et al. [24] is much greater than that used here, with values of 0.25 instead of 0.14. Stronger shear means that the wind closer to the ground is moving more slowly, relative to the free stream velocity. This may explain why the R_V values of Hansen et al. are smaller; the magnitudes of wake effects in the two tests might be more similar if the sheltered wind speed was normalized by the freestream wind speed, instead of the unsheltered wind speed at the same height. However, even with this large difference in shear, the two R_V profiles agree fairly well for the most part. In Figure 6.12 and Figure 6.14, R_I measurements showed similar trends but different magnitudes at the peaks. This may be due to the greater

upwind turbulence intensity used by Hansen et al. [24]. This is evidence that the differences in the two ABLs do have a significant effect of R_I .

Recall that a series of comparisons was also conducted in Chapter 4, in which current results were compared to reference wind tunnel results. It should be mentioned that although they were not included, wakeNET predictions for the profiles in Figure 4.4 through Figure 4.8 follow current wind tunnel results very closely. Each study used a unique simulated ABL, but the profiles were fairly similar. This is taken as further evidence that changes in the values of the quantities in Table 4.3 will not significantly affect the velocity wake of an obstacle, over the range of values of interest. R_V values from the current experiments matched those of the reference experiments to an acceptable degree without replicating all the details of the ABL. Turbulence intensity in the wake appears to be affected significantly by one or more of the parameters in Table 4.3, but the results are still satisfactory, since trends are predicted correctly.

6.4.2 Predictions for New Obstacles in the Wind Tunnel

Figure 6.15 shows how NN predictions of R_V compare to wind tunnel data for one of the pure validation tests. Recall that these obstacles were not used to generate training data; these predictions are all based on the relationship learned from measurements of the wakes of other obstacles. The validation obstacles were designed such that it would be difficult to make predictions in their wakes. A description of each obstacle is given in Table 4.1.

In general, the R_V predictions in Figure 6.15 are not as accurate as those in Figure 6.4 to Figure 6.10. Although the predicted profile for the 5-1-36 block overestimates the velocity deficit in the wake, overall, predictions for this obstacle are fairly good, especially above y = 1. The measured 3-1 block profile has also been predicted reasonably well. R_V Predictions for the 3-2-15 block are not accurate at lower heights; the velocity deficit is overestimated, especially at y = 0.9. Higher up, prediction accuracy improves. Wind tunnel measurements indicate that at this (x, z) location, for this a value, the 3-1 block creates a greater velocity deficit than the 3-2-15 block, which is

contrary to the effect of *PR* at other locations. It is possible that this is caused by the different *RA* values, but typically *RA* does not have a large effect at this distance from the obstacle. This finding illustrates the complexity of the problem; different obstacle characteristics will have a different effect at different points in the wake. For all three obstacles, predictions are better at heights greater than 1. This is important, since the main region of interest when siting small wind turbines is the far wake, at heights greater than that of the obstacle.

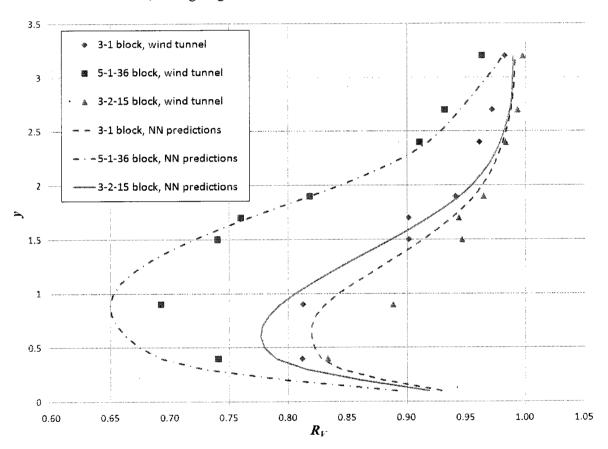


Figure 6.15 – Variation of R_V with height at x = 12, z = 3, a = -40 in the wakes of three obstacles used purely for validation

Figure 6.16 shows how predictions of R_l compare to wind tunnel results for the three obstacles used purely for model validation. Overall, the predictions are thought to be quite good, although they are not as accurate as predictions of R_l . The magnitudes of predicted and measured turbulence intensity excesses are often very similar, and the trends are predicted correctly. However, there are some large discrepancies present, such as at y = 1.7 for the 3-2-15 block. At y = 1.7

= 0.4, for the 5-1-36 block, it appears that the NN is trying to replicate the R_l value. However, recall that none of the measurements shown in Figure 6.16 were used for training; this 'peak' is thought to be the result of a training point for a similar obstacle, such as the 4-1 block.

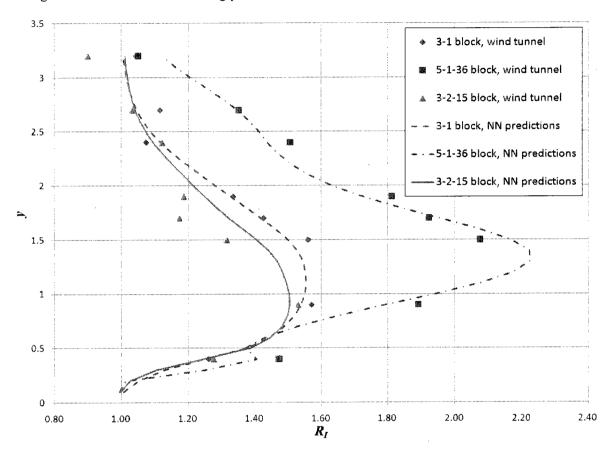


Figure 6.16 – Variation of R_I with height at x = 12, z = 3, a = -40 in the wakes of three obstacles used purely for validation

6.4.3 Above Obstacle Performance

Figure 6.17 and Figure 6.18 compare wakeNET predictions to an experimental study performed by Lubitz and Hakimi [48]. Their study included a BLWT test which measured the flow over a model barn with a peaked roof, performed at the same facility as the current project. Field measurements were taken using an upwind tower mounted sonic anemometer, and a sonic anemometer mounted above the roof peak of a barn. Figure 6.17 and Figure 6.18 show how model predictions compare to their experimental results for R_V and R_I , respectively. The barn's

AR, PR, and RA were 3.34, 2.51, and 30°, respectively. Since all wakeNET inputs were found in the study, predictions could be made and compared to their results. Also shown in Figure 6.17 and Figure 6.18 are results for a similar obstacle from current wind tunnel tests, the 2-1-30 block.

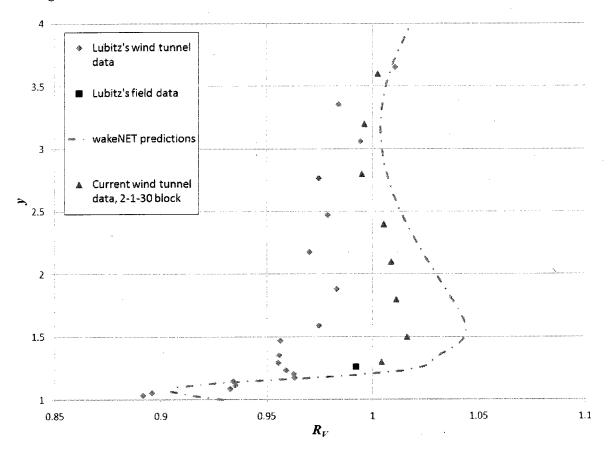


Figure 6.17 – wakeNET predictions of R_V compared to reference data

Very close to the roof, wakeNET predicts that the wind will slow down (since $R_V < 1$). Wind tunnel results from Lubitz's study also show a velocity deficit immediately above the obstacle. The single data point available from Lubitz's full scale experiment shows a very slight velocity deficit; wakeNET overestimates R_V at this point by 2%. This prediction is thought to be quite good, for two main reasons: i) no training data was used for this obstacle, and ii) wakeNET was mainly developed and intended for far field applications. Of course, this is only a single data point; further near obstacle validation is needed to obtain more meaningful results. Higher up, above y = 1.2, wakeNET predicts a region of speed up. This is not supported by Lubitz's wind

tunnel results, which show a velocity deficit until y = 3.6. However, current wind tunnel results for a very similar obstacle do show speed up between y = 1.5 and y = 2.4.

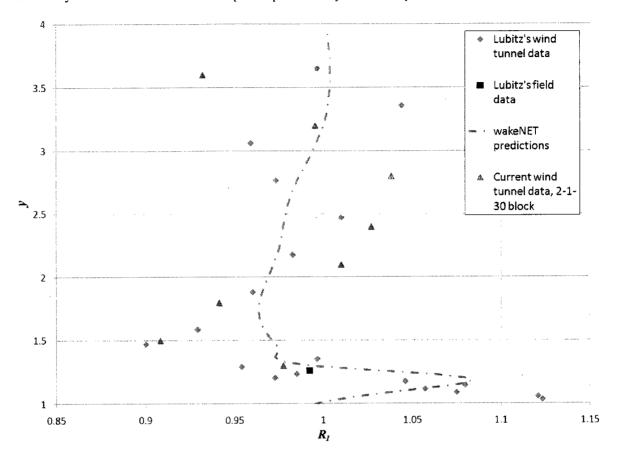


Figure 6.18 – wake NET predictions of R_I compared to reference data

As seen in Figure 6.18, reference wind tunnel and field R_I measurements agree fairly well with wakeNET predictions, near the roof anemometer location (y = 1.26). Higher above, there appears to be a great deal of variation in both sets of wind tunnel data. Model predictions appear to be roughly in the middle of the group of measured values. Overall, it is thought that wakeNET is suitable for making flow predictions higher above an obstacle, but closer to the obstacle, it is inadequate. This is similar to results seen in Figure 6.4, as previously discussed. As usual, R_I predictions are less confident than those for R_I .

6.4.4 Predictions for a New Full Scale Obstacle

Of main interest in this study is how wakeNET predictions compare to full scale conditions. So far, this thesis has mainly taken the approach of comparing full scale conditions to the wind tunnel, and then comparing wind tunnel measurements to model predictions. While this approach is useful, a more direct approach in which wakeNET predictions are directly compared to field results provides a better indication of model performance. Figure 6.19 and Figure 6.20 compare wakeNET predictions, wind tunnel results, and all converged mean values taken in the wake of the trailer. Figure 6.19 shows results for R_F , while Figure 6.20 shows results for R_F .

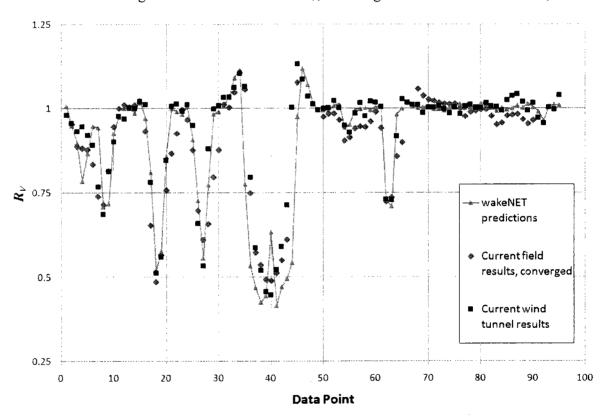


Figure 6.19 – R_V values from converged trailer field data, wakeNET predictions, and BLWT results

Neither the wind tunnel data nor the field data was used for training; the trailer is a new obstacle, for which wakeNET was not trained. Model predictions of R_V are reasonably good. The mean absolute difference between wakeNET predictions of R_V and values measured in the field is

6.9%. The locations of the peaks and troughs are predicted well. The greatest discrepancy between predictions and field data tends to occur at data points that were measured at anemometer 4, which was closest to the obstacle, as seen in Figure 5.1. When this anemometer is not considered, the mean absolute difference is reduced to 5.3%. This value is thought to be a more accurate estimate for values in the far field.

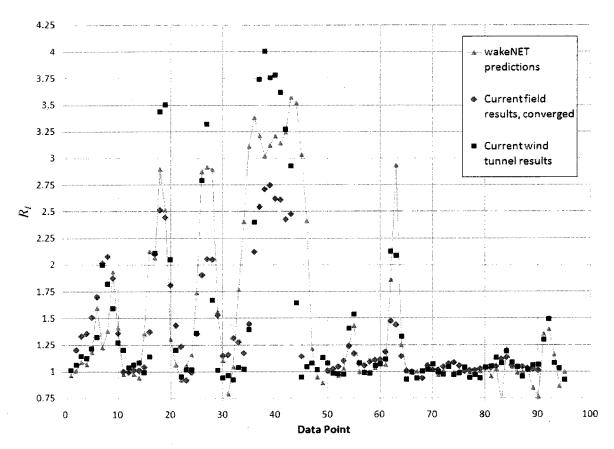


Figure $6.20 - R_I$ values from converged trailer field data, wakeNET predictions, and BLWT results

In Figure 6.20, it can be seen that R_l tends to be over predicted, as often seen in Figure 5.11 through Figure 5.18. This means that the model will be conservative when making predictions of turbulence intensity, which is not ideal, but acceptable. The mean absolute difference between wakeNET predictions and field measurements of R_l is 20.0%, which is actually quite high. When data from sensor 4 is not considered, the mean absolute difference decreases to 13.6%. Most of this discrepancy stems from the disagreement between field and wind tunnel R_l values, as

discussed in Chapter 5. Recall that the turbulence intensity value itself is not actually used when making an estimate of turbine power output. Rather, R_l is meant to be an indication of whether or not turbulence levels in the wake region are affected by the obstacle. In this context, wakeNET predictions are much more satisfactory, since the model appears to be reasonably good at predicting whether or not the obstacle will increase turbulence intensity at a point, rather than the specific magnitude of the increase.

6.5 Multiple Wake Interactions

In rural areas, obstacles such as buildings and trees are most commonly located in small groups or clusters. The interaction of individual wakes greatly complicates the local flow field. As described in Section 2.3, even a relatively 'simple case' of bluff body flow is very complex. The process of making wake predictions becomes even more complex when multiple obstacles are considered.

A NN-based approach could be used to predict R_V and R_I in the wake of an obstacle group, similar to the model development for the SIS. New inputs would include each obstacle's spacing in the downwind direction S_x and the lateral direction S_z . In addition, the four inputs that define the obstacle in the SIS model would also be needed (a, AR, PR, and RA). The point of interest in the wake is defined by an (x, y, z) position. Using this approach, the total number of inputs required for a three obstacle group is estimated to be 21. It is thought that this is unfeasible using current methods due to the enormous quantity of data that would be required to adequately train the model. By removing PR and RA, the number of inputs is reduced to 15. If the centre of one of the three obstacles is always defined as being located at (x, z) = (0, 0), then S_x and S_z of one obstacle are no longer required, further reducing the number of inputs to 13. This is much more manageable than 21, but even still, an extremely large amount of training data would be required.

A simple estimate can be made of the number of points that would be necessary to train such a NN using an approach similar to that taken here. Recall that in this study, 41762 potential

training data points were obtained, of which roughly 90% were used to train the network (the remainder was validation data). About 37586 points were used as training data, wakeNET has seven inputs. In terms of quantity of training data, this is equivalent to each input having an average of 4.5 unique values, and the training data consisting of all possible permutations of these values. Using a value of 4.5 exactly, the total number of permutations of input values in this case would be $4.5^7 = 37367$, close to the amount of training data used here. If the NN had 13 inputs instead of 7, the number of training points needed would be $4.5^{13} = 310.3 \cdot 10^6$. This is the estimated number of training points required to achieve accuracy and generality comparable to that of wakeNET, but with a much greater scope. A NN-based model trained with fewer points may still provide useful but perhaps less reliable estimates.

The neglection of RA and PR would reduce the accuracy of the model, although it is expected that the predictions would still be useful, since the most important inputs (AR and a) are still considered. A NN-based approach is not pursued here because of the unfeasibility of obtaining the required training data using current methods.

In Appendix G, several approaches to predicting R_V in the wake of a cluster of obstacles are proposed. These methods are based largely on how R_V is predicted for SIS. The proposed methods are compared to a limited set of wind tunnel data, which consists of measurements made in the wake of two unique structure groups, for a range of wind directions. Although it is difficult to generalize these results, it was found that in most cases, the best method of predicting R_V in the wake of an obstacle cluster depended on the spacing of obstacles in the cluster, and the position of interest. When the spacing was large, and when the point of interest is close to an obstacle, R_V was best predicted by the linear superposition of individual wake effects. Conversely, when the spacing was small, and the point of interest was further away, R_V was best predicting by replacing the cluster with a single large obstacle, and modifying the prediction based on Musselman's empirical model for centerline velocity deficit, which was discussed in Chapter 2. See Appendix G for details.

6.6 Sources of Error

Several sources of error were present in both the wind tunnel and the field experiments that will affect the validity of the model. Quantitative estimates of the uncertainties in measured and calculated values are given in Chapter 4 for the wind tunnel tests and Chapter 5 for the field tests; these are also explained in detail in Appendix F. Sources of error are summarized here; most are mentioned elsewhere in this thesis. As discussed in Chapter 4, the wind tunnel is not a true simulation of field conditions. All wind characteristics cannot be matched; compromises must be made [29]. For example, atmospheric stability conditions could not be simulated in the BLWT. The simulated ABL is inherently isothermal. The power spectra in the field (Figure 5.4) and the wind tunnel (Figure 4.3) are also inherently different [42]. The simulated ABL in the wind tunnel should depend on the scale of the simulation [28]. In this research, it has been assumed that wake characteristics are independent of scale, and a standard simulated boundary layer has always been used.

During testing, there was a slow vibration of the probe in the lateral direction. The vibration was stronger when the traverser arm was fully extended (so at lower heights), and when the arm was in a region of higher turbulence. The greatest vibration frequency was estimated to be roughly 4 Hz. When the probe arm was not fully extended, which was the case when measuring at greater heights, vibrations were much slower, or not evident.

Although the probe was positioned carefully in the wind tunnel, it is inevitable that there will be some probe positioning error. During wind tunnel testing, the lateral velocity component was not measured, possibly resulting in a small under prediction of the true velocity. To test this, the probe was rotated 90° to directly measure the lateral component of the unsheltered flow; it was found to be insignificant. However, at positions very close to the models, there are likely stronger lateral velocities. Because of this, and because a hot film probe cannot distinguish

between forward and reverse flow, measurements were not made at or near the recirculation zones of the obstacles.

Since wakeNET is based directly on wind tunnel measurements, the model can only ever be as good as the wind tunnel simulation. Based on the validation performed in Chapter 5, this should not be a source of major error when predicting R_V , but it will be a significant factor when predicting R_I , and should not be neglected when applying wakeNET to real situations.

In the field, it was somewhat difficult to determine the sensor direction to a high degree of accuracy. Recall that 10° wind direction bins were used for the field experiment. If a sonic anemometer was oriented even a few degrees off from where it was thought to be oriented, this could have an effect on several of the figures shown in Chapter 5. Values that should fall inside one bin may fall into another, resulting in inaccurate mean R_V and R_I values. Great care was taken to measure the orientation of each sonic anemometer.

Another assumption was that at any given moment, the wind direction was the same at all anemometers. Since the obstacle would affect all wind velocity components at any sheltered sonic anemometer, the unsheltered anemometer was always used to determine the direction. However, it is possible that the wind approaching a tower is coming from a slightly different direction than the wind approaching an adjacent tower. Lastly, based on the precision limits and convergence checks described in Chapter 5, several of the wind sectors of interest did not appear to have converged. More wind data would be useful in minimizing the uncertainty of mean R_{ℓ} and R_{ℓ} values.

6.7 Model Performance Summary

The main purpose of wakeNET is to assist in the micrositing of small wind turbines. Of main concern is the model's ability to predict lower magnitude effects in the far wake. For example, the viability of a specific location may depend on whether $R_V = 1.00$ or 0.95 at that point. It is thought unlikely that the viability of a location depends on whether $R_V = 0.7$ or 0.8,

since in both cases, severe sheltering effects are present. In general, neither point is suitable for a small wind turbine.

The accuracy of the model is inherently tied to its ability to replicate wind tunnel data, and the ability of the wind tunnel simulation to replicate field data. From these uncertainties, the overall uncertainty in predictions of R_V , R_I , and R_P in the wind field can be estimated.

In Section 6.4.4, it was shown that predictions of R_V will had a mean average difference of 5.3% for positions in the wake of a new full scale obstacle. It should be noted that this is based on the limited number of points available. The applicability of this result to other obstacles can be investigated by combining the mean absolute differences between the field and wind tunnel, described in Table 5.4 and Table 5.5, and wakeNET's accuracy when making predicting for new obstacles in the wind tunnel, described in Table 6.3. Considering all three field obstacles, there was an average of 4.4% difference in the R_V values of the two sets of experiments. For new obstacles in the wind tunnel, in the far wake, the mean difference was 1.3%. Combining the differences associated with going from the field to the wind tunnel, and then the wind tunnel to the model, the total error is 4.6% [41]. The average of the two total uncertainty estimates (5.3% and 4.6%) is roughly 5.0%, which is used going forward. This is the estimate of the mean error of wakeNET predictions of R_V in the far wake of an obstacle.

Similarly, predictions of R_l had a mean average difference of 13.6% for a new obstacle in the field. Combining the uncertainties associated with going from the model to the wind tunnel for new obstacles, 5.3%, and the wind tunnel to the field, 10.7%, a total mean uncertainty of 11.9% is obtained. The mean error of wakeNET predictions of R_l is estimated to be 12.8%.

To estimate the power output of a sheltered turbine, it is necessary to specify the turbine's power curve as well as the wind rose at the site. An example of this calculation is included as Appendix A. More generally, it can be assumed that sheltering effects on a turbine are the same as sheltering effects on the power density. This is quantified by R_P , which is defined in Equation 3.3. Using an uncertainty of 5.0% for R_V , derived above, the mean uncertainty of R_P is 15%.

Assuming that local unsheltered wind data is accurate, and neglecting effects from increased turbulence, wakeNET predictions of mean power output are estimated to have an average error of 15%.

wakeNET predictions will be most accurate in the far wake ($x \ge 5$) and at heights greater than that of the obstacle ($y \ge 1$). Predictions can be made for locations closer to the obstacle, and even for locations above the obstacle, but in general, accuracy will be reduced at these points. Since trees and terrain are not considered here, their presence at a site will reduce the accuracy of wakeNET predictions. At the test site, the grade was estimated to be ~1%, and no trees were present. The model is expected to perform well in similar conditions. Future research into the effects of trees and hills would be useful. Although it is considered unlikely that a simple model will be able to make accurate quantitative predictions for complicated sites, it is thought that more specific qualitative knowledge of wind fields near hills and trees would greatly assist the siting process when these features are present.

7.0 Conclusions and Recommendations

The magnitude and extents of an obstacle's wake in a turbulent boundary layer depend greatly on the obstacle's orientation and AR, and to a lesser extent on its PR and RA.

An obstacle with a large AR will cause a much greater disturbance in the boundary layer than an obstacle with a small AR. A significant velocity deficit (>5%) can be measured more than 40 heights downwind of a wide obstacle. Even at great downwind distances, a wide obstacle could reduce the power output of a small wind turbine. In the centre region of an obstacle with a very large AR, wake properties will be similar to that of the two-dimensional case. This is true up to a downwind position that is dependent on the obstacle's AR.

Vortex formation within the wake is dependent on the orientation of the obstacle relative to the wind direction, and can strongly affect mean velocity and turbulence levels in the wake.

Wakes are only symmetrical for special cases of model orientation; specifically, when the obstacle geometry is symmetrical about the wind direction.

Increased PR can often be associated with an increase in the magnitudes of wake effects, although there are exceptions. The effects of PR and RA strongly depend on obstacle orientation and the position of interest in the wake.

Existing small wind turbine siting guidelines are generally inadequate for wide obstacles (AR > 4). Existing simple sheltering models are only suitable for predicting wind characteristics in "simple" wakes.

While useful, existing siting guidelines are too simple. Recommendations made using existing guidelines do not depend on the width, depth, or roof shape of the obstacle, all of which can have an effect on the local wind climate. Depending on the characteristics of the obstacle, guidelines will overestimate or underestimate the distance at which velocity and turbulence intensity wake effects have mostly dissipated.

Existing anemometer sheltering models can accurately predict wind characteristics in the wake when a face of the obstacle is normal to the wind direction. However, as the wind direction changes from these special cases, predictions made by existing models vary significantly from wind tunnel data and full scale field measurements.

The velocity wake of a full scale obstacle can be successfully simulated in the BLWT. The turbulence wake is more difficult to simulate accurately.

The mean wind speed and turbulence intensity in obstacle wakes have been measured in a full scale field experiment, using three distinct obstacles. A BLWT simulation of each field experiment has also been conducted. A comparison of the two tests indicates that the velocity wake measured in the BLWT is a reasonably accurate simulation of the wake of a full scale obstacle. Discrepancies between the full scale and simulated velocity wakes are small or rare; it is difficult to discern whether these differences are the result of experimental error or genuine differences in the two flows. There is some evidence that locations in the wake strongly influenced by standing vortices may be more dependent on *Re* than locations where effects from vortices are insignificant. Turbulence intensity measurements made in the BLWT experiment were generally greater than those made in the field. Over the range studied, mean wind speed effects appear to be independent of *Re*, while turbulence intensity effects appear to depend on *Re* to some extent. Wind tunnel simulations were more accurate for flow properties in the far wake than in the near wake.

A new NN-based model has been developed that can make accurate predictions of the velocity wakes of simple, solid obstacles exposed to a rural ABL.

Two NNs have been trained using wind tunnel data to predict the effect of an obstacle on mean wind speed and turbulence intensity. These models have been validated through a comparison with new field data. It is estimated that predictions of R_V , R_I , and R_P for points in the

far wake of a full scale obstacle, at heights greater than that of the obstacle, will have a mean error of 5.0%, 12.8%, and 15%, respectively. These estimates are valid for sites where the ABL is similar to that of the test site used in this thesis. The main source of uncertainty is the wind tunnel simulation; while valid, it is inherently different from an actual ABL. Predictions will be most accurate for obstacles similar to those used to train the model; however, predictions made using new obstacles still tend to show fairly good accuracy, especially in the far wake region. The new model has only been validated for an ABL that would be found in open, rural areas. The model should not be used in an urban setting. In the future, model predictions in the near wake and above obstacle regions could be improved through the creation of a separate NN for each region.

Initial trials suggest that the velocity deficit in the wake of an obstacle cluster can be predicted, with a varying degree of accuracy.

The flow through and around a group of obstacles is very complex and difficult to predict. Five methods of predicting the velocity deficit at any point in the wake of an obstacle cluster were developed and evaluated against wind tunnel measurements. These methods are based largely on the SIS model developed in this thesis. The most accurate method depends on the obstacle spacing and downwind distance of interest. When spacing between obstacles in the cluster is large, model predictions will be most accurate. Further research on how wake effects combine may prove useful, although it is expected that no 'simple' model will be able to make predictions much more accurate than the current methods due to the complex nature of the flow.

Further model validation should be conducted for both single isolated structures and groups of obstacles.

While additional field experiments would provide invaluable results, some model validation can be conducted by comparing predictions to existing results from other sources.

Databases of wind measurements already exist from which validation data could be extracted. For

example, results from a field experiment conducted in early 2009 are available, but have not been used in this thesis. They have not yet been analyzed to the point where a comparison could be made to a wind tunnel simulation. These results (and others, if available) should be analyzed to obtain estimates of velocity deficit and turbulence intensity excess in the wake, and compared to wind tunnel simulations and model predictions.

WakeNET should be incorporated into a software tool that can make wind speed and turbulence intensity predictions for entire flow fields, for any site.

The motivation for this project was to develop a software tool that can assist in the micrositing of small wind turbines. Wind speed and turbulence intensity predictions made by wakeNET would be immensely useful when estimating the power output of a turbine at a potential site. The software should incorporate existing models for effects from trees and changing terrain. Future work could include the creation of new NNs to predict wake effects from trees, silos, hangars, or other types of buildings. These additional models could then be incorporated into the overall wakeNET model.

References

- Riso DTU National Laboratory for Sustainable Energy. WAsP 9 Help Facility & On-line
 Documentation. 2010. Available online at
 http://www.wasp.dk/Support/FAQ/WebHelp/Wasp9.htm#Shelterbehindobstacles.htm.
 Accessed January 2009.
- 2. Marbek Resource Consultants Ltd. Survey of Small (300 W to 300 kW) Wind Turbine Systems in Canada. CANMET Energy Technology Centre-Ottawa, DNR, Gov. of Canada. 2005.
- 3. American Wind Energy Association. AWEA Small Wind Turbine Global Market Study. 2009.
- Ontario Power Authority. microFIT Program Overview. 2009. Available online at http://microfit.powerauthority.on.ca/pdf/microFIT-Program-Overview.pdf. Accessed March 2009.
- 5. Tominaga, Y., Mochida, A., Yoshie, R., Kataoka, H., Nozu, T., Yoshikawa, M, Shirasawa, T. AlJ guidelines for practical applications of CFD to pedestrian wind environment around buildings. 2008. J. Wind Engin. Industr. Aerodyn, Vol. 96, Issues 10-11, pp. 1749 1761.
- 6. **Heath, M. A.** Estimating the Potential Yield of Small Building-mounted Wind Turbines. 2007. pp. 271-287. Wind Energy, 3, pp. 271-287.
- 7. Versteeg, H. K., Malalasekera, W. An Introduction to Computational Fluid Dynamics. 2007.

 Longman.
- 8. Lubitz, W. D., White, B. R. Wind-tunnel and field investigation of the effect of local wind direction on speed-up over hills. 2007. J. Wind. Engin, Industr. Aerodyn., Vol. 95, pp.639 661.
- 9. Rathmann, O., Mortensen, N. G., Landberg, L., Bowen, A. Assessing the Accuracy of WAsP in Non-simple Terrain. 1996. BWEA 18.

- 10. Gipe, P. Wind Energy: How to Use It. Harrisburg: Stackpole Books, 1983.
- 11. **U.S. Department of Energy.** *Small Wind Electric Systems.* 2005. Available online at http://www.windpoweringamerica.gov/pdfs/small_wind/small_wind_guide.pdf Accessed: Sept-2008..
- Brunskill, A. Improved Siting Guidelines for Small Wind Turbines. 2008. Poster Presentation. Vancouver, BC, CA. 2008.
- 13. **Lemberg, R.** On the wakes behind bluff bodies in a turbulent boundary-layer. Boundary

 Layer Wind Tunnel Laboratory, University of Western Ontario. 1973. London, Ontario,

 Canada. Ph.D. Dissertation.
- 14. Manwell, J.F., McGowan, J.G., Rogers, A.L. Wind Energy Explained. West Sussex: John Wiley & Sons Ltd., 2002.
- 15. Kaiser, K., Langreder, W., Hohlen, H., Hojstrup, J. Turbulence Correction for Power Curves. Berlin, Heidelberg: Springer, 2007.
- 16. Sicot, C., Devinant, P., Laverne, T., Loyer, S., Hureau, J. Experimental Study of the Effect of Turbulence on Horizontal Axis Wind Turbine Aerodynamics. 2006. pp. 361-370. Wind Energy 9, pp.361-370.
- 17. **Sheinmann, Y., Rosen, A.** A dynamic model of the influence of turbulence on the power output of a wind turbine. 1992. J. Wind Engin. Industr. Aerodyn., 39, pp. 329-341...
- 18. **Zhou, Y., Kareem, A.** Definition of Wind Profiles in ASCE 7. 2002. Technical Note, J. Structural Engineering, ASCE, Vol.128, No.8, pp.1082-1086.
- Peterka, J. A., Meroney, R.N., Kothari, K.M. Wind Flow Patterns About Buildings. 1985.
 J. Wind Engin. Industr. Aerodyn. 21, pp. 21 -38.
- 20. **Hosker, R.P.** Empirical Estimation of Wake Cavity Size behind Block-type structures. 1979. Fourth Symp. on Turbulent Diffusion and Air Pollution, Reno, NV, USA.

- 21. Frost, W., Fichtl, G., Connell, J. R., Hutto, M. L. Mean Horizontal Wind Profiles

 Measured in the Atmospheric Boundary layer about a Simulated Block Building. 1977.

 Boundary-Layer Meteorology, 11, pp.135-145.
- 22. Yakhot, A., Liu, H., Nikitin, N. Turbulent flow around a wall-mounted cube: A direct numerical simulation. 2006. International Journal of Heat and Fluid Flow, 27, pp.994-1009.
- 23. Musselman, D. D. Turbulent Wake Interactions of Multiples Structures in and Atmospheric Boundary Layer. Boundary Layer Wind Tunnel Laboratory, University of Western Ontario, London, Ontario, Canada: s.n., 1996. Ph.D. Thesis.
- 24. Hansen, A., C., Peterka, J. A., Cermak, J. E. Wind-Tunnel Measurements in the wake of a simple structure in a simulated atmospheric flow. NASA STI. 1975. Recon Technical Report CR2540.
- 25. Martinuzzi, R., Tropea, C. The Flow Around Surface-Mounted, Prismatic Obstacles Placed in a Fully Developed Channel Flow. 1993. Journal of Fluids Engineering, Vol. 115, pp.85-92.
- 26. Counihan, J., Hunt, J.C.R., Jackson, P.S. Wakes behind two-dimensional obstacles in turbulent boundary layers. 1974. J. Fluid Mech., Vol.64, Issue 3, pp.529-563.
- 27. Perera, M.D. Shelter behind two-dimensional solid and porous fences. 1981. J. Wind Engin. Industr. Aerodyn., 8, pp.93-104.
- 28. Snyder, William H. Guideline for Fluid Modeling of Atmospheric Dispersion.
 Environmental Sciences Research Laboratory, U.S. Environmental Protection Agency,
 1981.
- 29. Lim, H. C., Castro, I. P., Hoxey, R. P. Bluff bodies in deep turbulent boundary layers:

 Reynolds-number issues. 2007. J. Fluid Mech., Vol. 571, pp.97-118.
- 30. **Taylor, P.A., Salmon, J.R.** A Model for the Correction of Surface Wind Data for Sheltering by Upwind Obstacles. 1993. J. Appl. Meteor. Vol.32, pp.1683-1694.

- 31. Pope, Stephen B. Turbulent Flows. Cambridge: Cambridge University Press, 2008.
- 32. **Hunt.** The Effect of Single Buildings and Structures. 1971. Philosophical Transactions of the Royal Society of London. Series A, Mathematical and Physical Sciences. May 13. pp.457-467.
- 33. Troen, I., Petersen, E. L. European Wind Atlas. 1989. Riso National Laboratory.
- 34. **Demuth, H., Beale, M.** Neural Network Toolbox User's Guide, Version 4. Natick, MA: The MathWorks.
- 35. **Graupe, D.** *Principles of Artificial Neural Networks, 2nd Ed.* Singapore : World Scientific Publishing, 2007.
- 36. **Bitsuamlak.** Effects of upstream two-dimensional hills on design wind loads: A computational approach. 2006. Wind and Structures, Vol.9, Issue 1, pp.37-58.
- 37. Kariniotakis, G.N., Stavrakakis, G.S., Nogaret, E. F. Wind Power Forecasting Using

 Advanced Neural Networks Models. 1996. IEEE Transactions on Energy Conversion,

 Vol. 11, Issue 4, pp.762-767.
- 38. **Zhang, A., Zhang, L.** RBF neural networks for the prediction of building interference effects. 2004. Computers and Structures, Issue 82, pp.2333-2339.
- 39. Ontario Ministry of Natural Resources. Ontario Wind Atlas. Available Online at http://www.ontariowindatlas.ca. Accessed March 2010.
- 40. TSI Incorporated. TSI Thermal Anemometry Probes Catalog. 2008. Available online at http://www.tsi.com/uploadedFiles/Product_Information/Literature/Catalogs/Hotwire_Cat alog 2980465.pdf. Accessed Sept. 2009.
- 41. Coleman, H. W., Steele, W. G. Experimentation and Uncertainty Analysis for Engineers.

 John Wiley & Sons, Inc., 1989.
- 42. Burton, T., Sharpe, D., Jenkins, N., Bossanyi, E. Wind Energy Handbook. West Sussex, England: John Wiley & Sons Ltd., 2001.

- 43. **Ziter, B.** Characterization of University of Guelph's Wind Tunnel for Atmospheric Boundary

 Layer Simulation. 2009. School of Engineering, University of Guelph. Report prepared

 for course ME664 Turbulent Flow, at the University of Waterloo.
- 44. Campbell Scientific, Inc. CSAT3 Three Dimensional Sonic Anemometer Instruction Manual. 2007.
- 45. R.M. Young Company. Model 81000 Ultrasonic Anemometer Manual. REV C031405. 2008
- 46. NRG Systems. NRG #40c Anemometer Specifications. 2007. Rev. 2.0.
- 47. U.S. Department of Energy. Small Wind Electric Systems. A U.S. Consumer's Guide. 2005.

 Available online at

 http://www.windpoweringamerica.gov/pdfs/small_wind/small_wind_guide.pdf. Accessed

 Sept. 2008.
- 48. Lubitz, D., Hakimi, R. Effect of Roof Slope on a Building-Mounted Wind Turbine. 2008.

 Proceedings of the 46th AIAA Aerospace Sciences Meeting and Exhibit, Reno, NV,

 USA. Jan.7-10. pp.1325.

Appendices

A. Case Study

This appendix presents an example of how to use wakeNET to predict the power output of a small wind turbine at a sheltered location. Required information includes:

- Local unsheltered wind conditions, from a wind map or a nearby meteorological tower
- ii) The wind turbine's power curve, provided by the manufacturer.

 In addition, it is necessary to specify:
 - i) The latitude and longitude of the site
 - ii) The position of interest
 - iii) The size, shape, and location of all nearby obstacles

Once the above information has been obtained or determined, the general procedure to predict the power output consists of the following three steps:

- i) The velocity ratio R_{ν} and turbulence intensity ratio R_{l} are calculated at the point of interest for a range of wind directions.
- Based on the distribution of wind speed at the site, the turbine's power curve, and R_{ν} , the average power output of the turbine is predicted for wind from each direction.
- iii) The overall mean power output of the turbine is predicted based on the wind rose and the average power output of the turbine for each wind direction.

Required Information

In this example, the potential turbine site is near the eastern shore of Lake Huron, at 43.9° N, -81.7° W, as shown in Figure A.1. The surrounding area is flat. There are two buildings nearby, as shown in Figure A.2. The size and shape of each building are defined in Table A.1.



Figure A.1 – Location of turbine site, north of Goderich, Ontario (image courtesy of Google Earth)

Table A.1 – Obstacle characteristics

Obstacle	Height h	Aspect	Plan ratio	Roof angle	Centre distance
		ratio (AR)	(PR)	(RA)	to turbine
1	7 m	7.1	2.9	30°	124.2 m
2	8 m	5.6	2.8	15°	80.1 m

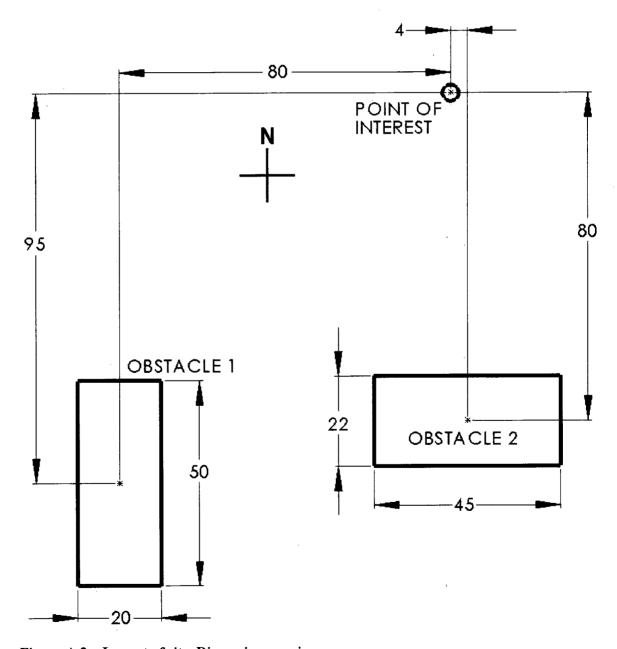


Figure A.2 - Layout of site. Dimensions are in m

Since there is a large distance between the obstacles (51.5 m, or 6.4 h_2), it is best to treat them separately, and combine their effects on the wind linearly using superposition. Predictions of R_V and R_I at the point of interest will be made for each obstacle and then combined. The turbine in this case study is the Bergey Excel-S, which is a grid-intertie model with a rated power output of 10 kW.

Step 1 – Calculating R_V and R_I for each Wind Direction

 R_V and R_I at a point will depend on the wind direction. Recall that wakeNET requires seven inputs. Aspect ratio AR, plan ratio PR, and roof angle RA will be constant, and are specified in Table A.1 for both obstacles. The hub height y of the turbine is also constant, and specified to be 16 m. The remaining three inputs (downwind distance x, lateral position z, and model orientation angle a, relative to the flow) will vary with wind direction, as illustrated in Figure A.3.

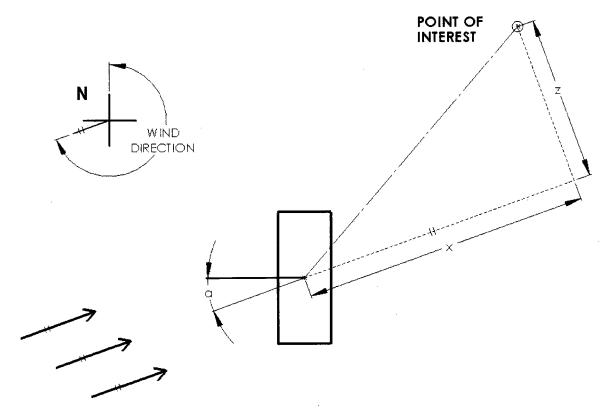


Figure A.3 – Definitions of x, z, and a, for any wind direction, for obstacle 1

A positive x value indicates that the point of interest is downwind of the obstacle. Positive z is defined as to the right, when facing upwind. a values are always adjusted to be between -90° and 90°.

It is necessary to specify the wind directions for which wakeNET will make predictions. Predictions should be made covering the entire range of possible wind directions, from 0° to 360° on the wind rose. The angular resolution at which to make predictions is important; in general, a greater resolution will result in more accurate final results. A resolution of 10° is used here. At the point of interest, 36 unique R_{V} and R_{I} values are obtained, based on wind directions of 0° to 350° at 10° increments. Figure A.4 shows how R_{V} , R_{I} , and R_{P} vary with wind direction at the point of interest. The effects of the two buildings can clearly be seen. The angular axis displays the wind sector, where sector 1 is centered at 0° , sector 2 is centered at 10° , continuing in this way until sector 36, which is centered at 350° . The radial axis is the value of the ratio. R_{V} and R_{I} were predicted by wakeNET. The process used to estimate R_{P} is described below.

Step 2 - Predicting Turbine Power Output for each Wind Direction

 R_P is defined as the ratio of sheltered to unsheltered turbine power output. In Figure A.4, it can be seen that R_P varies with wind direction, similar to R_V . R_P was previously defined as the change in power density of the wind. Since in this case study, the specific turbine has been identified, a more accurate prediction of R_P for each wind direction can be made based on R_V , the velocity distribution at the site, and the turbine's power curve. R_P values shown in Figure A.4 are based on this new definition.

The Ontario Wind Atlas provides an estimate of the local wind speed distribution in the form of the Weibull distribution. This is the probability density function of unsheltered wind speed at the site. At 16 m, the Ontario Wind Atlas predicts the Weibull shape parameter k and scale parameter c to be 1.91 and 5.534, respectively. The probability density P of a wind speed V is given by Equation A.1, as defined by the Weibull distribution.

$$P(V) = \left(\frac{k}{c}\right) \left(\frac{V}{c}\right)^{k-1} exp\left(-\left(\frac{V}{c}\right)^{k}\right)$$
(A.1)

Similarly, the sheltered wind speed probability density can also be defined by a Weibull distribution. The sheltered function can be obtained by modifying the scale parameter c, while keeping the shape parameter k constant. The relationship between the sheltered and unsheltered scale parameters, c_S and c_U , is shown in Equation A.2.



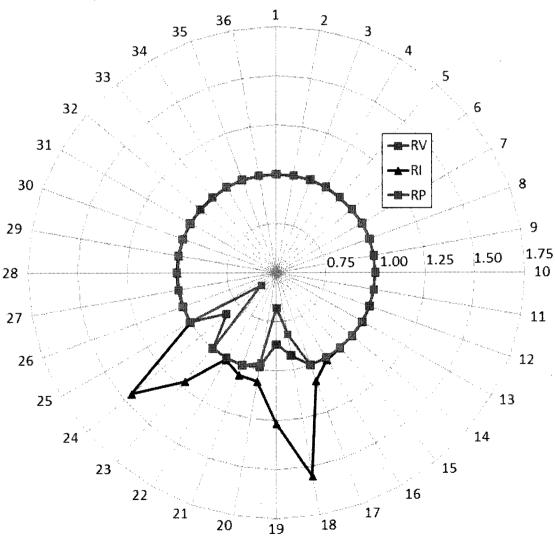


Figure A.4 – Variation of R_V , R_I , and R_P with wind sector

The unsheltered velocity distribution is shown in Figure A.5. Also shown is the sheltered velocity distribution for wind from sector 19, where $R_V = 0.86$. The turbine's power curve is included as well.

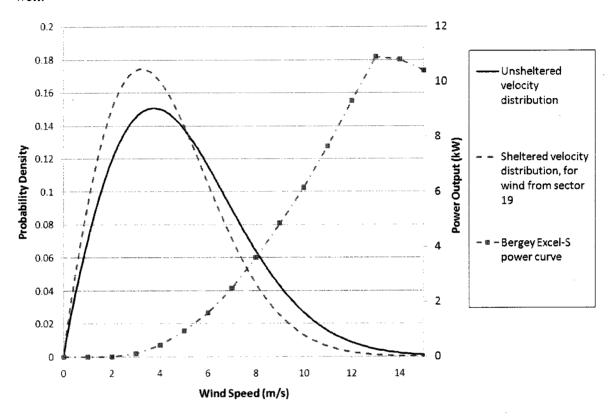


Figure A.5 – Unsheltered velocity distribution, and sheltered for wind sector 19, where R_V = 0.86. Also shown is the turbine power curve

Each wind direction has a unique sheltered velocity distribution, defined by the unsheltered distribution and the R_{ν} value, for that direction. The wind map only provides a single velocity distribution; it is assumed that this applies equally to all wind directions. Data from a meteorological tower could be used to obtain a unique velocity distribution for each wind direction, which may result in better prediction of turbine power output, depending on the site. For example, as will be seen in Figure A.6, the wind frequently comes from the bin centered at 240° (as predicted by the Ontario Wind Atlas). In Figure A.4, it is evident that sheltering effects are greatest for this wind direction. If in reality, winds from this direction are consistently stronger than winds from other directions, the process described here will underestimate the

degree of sheltering at the point of interest. However, for simplicity, the unsheltered velocity distribution from the wind map is used exclusively here.

For each wind direction, the turbine's mean power output is calculated for the sheltered and unsheltered cases. Mean power output is the mean of the power curve, weighted by the velocity distribution of wind. R_P is then defined as the ratio of the sheltered to unsheltered mean power output. The predicted R_P value for each wind direction is shown in Figure A.4.

Predictions made using the above approach will generally be very similar to those based purely on the changing power density in the wind. The difference lies in the fact that using this approach, changes in the turbine's power coefficient are taken into account as well, resulting in better predictions. For example, if the wind speed is reduced from 8 m/s to 7 m/s, both the power density of the wind and the power coefficient will change.

Step 3 - Estimating Overall Mean Power Output

Once the mean power output is known for each wind direction, the overall mean power output at the point can be estimated based on the distribution of wind direction at the site. This is given by the wind rose, which can be found either from measurements taken at a nearby meteorological tower, or from a wind map. Although only one wind rose is needed to calculate turbine power output, three unique wind roses are used here to investigate how the choice of wind rose affects final results. Sources are:

- i) The Ontario Wind Atlas, which uses 30° direction bins, and has a spatial resolution of 200 m, covering the entire province. Wind roses are available at heights of 30 m and 80 m.
- ii) the Canadian Wind Energy Atlas, which also uses 30° direction bins, and has a spatial resolution of 5 km, covering the entire country. Wind roses are available at 30 m, 50 m, and 80 m.
- iii) A nearby meteorological tower, with measurements reported using 10° bins. The tower is located roughly 16 km away, at the Goderich Airport. Hourly wind data

for a full year was used to create the wind rose. Measurements were taken at 10 m.

Predictions from the Ontario Wind Atlas are based on mesoscale and microscale models. Actual data should be a much better indication of local wind conditions. The main drawback of using data from the meteorological tower is that it is located 16 km away; wind conditions at the tower may differ from those at the site. Figure A.6 shows the three wind roses considered, using 30° bins. Data from the two wind atlases is for the closest height available, 30 m. There is a fairly large discrepancy between all three wind roses.

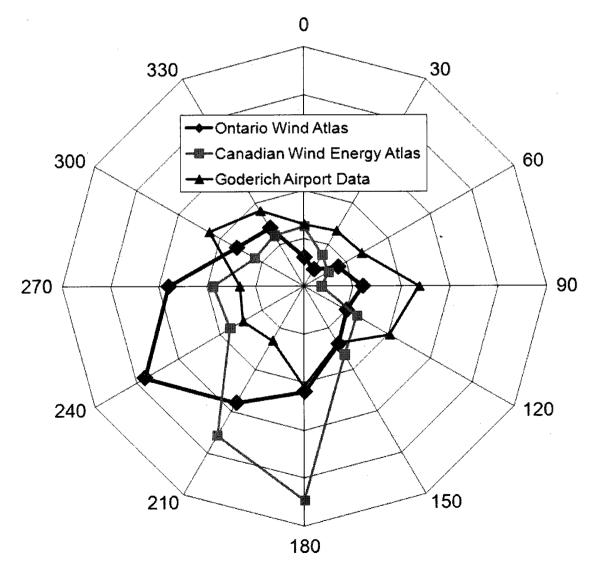


Figure A.6 – Wind roses for the site, using 30° bins

Figure A.7 shows the same three wind roses using 10° bins. For the wind atlas data, a 10° resolution was obtained by assuming that within each sector, the probability of each wind speed is equal. In reality, this is unlikely to be true but it is a necessary assumption if the wind atlases are to be used (recall that a 10° angular resolution was specified).

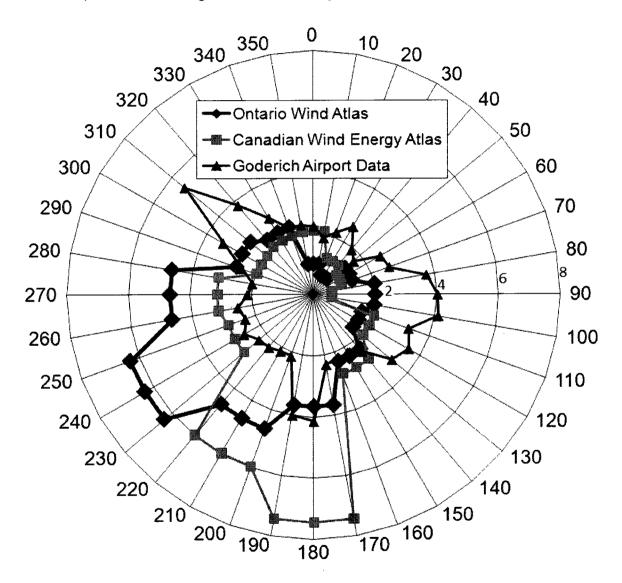


Figure A.7 - Wind roses for the site, using 10° bins

The overall mean power output at the point of interest is the average of the power output from each wind direction, weighted by the frequency of wind from that direction. A final R_P value can be obtained by finding the ratio of sheltered to unsheltered overall mean power output. Similarly, overall R_V and R_I values can be obtained by finding the average of the value at each

wind direction, weighted by the frequency of wind from that direction. Results of this calculation are summarized in Table A.2, for each wind rose.

Table A.2 – Case study final results

	Unsheltered	Ontario	Canadian Wind	Goderich Airport
		Wind Atlas	Energy Atlas	
R_V	1.00	0.98	0.98	0.99
R_P	1.00	0.95	0.95	0.97
R_I	1.00	1.08	1.10	1.05
Mean power	1.524 kW	1.455 kW	1.445 kW	1.481 kW
output			·	
Turbine capacity	15.2%	14.6%	14.5%	14.8%
factor				

It is difficult to say which wind rose is best in this case; each data source has drawbacks. The wind atlases are based on models, and are not in particularly good agreement with each other. Also, predicted wind direction frequencies are for nearly twice the height of the turbine. It is thought that data from the meteorological tower is the best indication of local wind conditions, even though reported values are for a lower height, 16 km away from the site. Although not pursued here, mean wind speed measurements from the tower could have been used to create a velocity distribution for each wind direction. It would be necessary to assume a value for wind shear to obtain predicted velocities at the height of interest.

Obstacle effects are predicted to reduce the mean power output of the turbine by between 3% and 5%. This estimate is based only on the decrease in power density of the wind, and does not consider effects from increased turbulence. Turbulence intensity at the point of interest is predicted to be between 5 and 10% greater than that in the unsheltered flow, at the same height.

Recall that wakeNET tends to over predict turbulence intensity, so this is likely an overestimate.

These predictions are highly dependent on the wind rose.

This case study has only examined a single point. A software tool has been developed which can quickly perform the above calculations at a wide range of locations at the site. This creates a map of the area, which shows how the degree of sheltering varies throughout the site. Such a map would be very useful when determining the optimal location for a turbine.

B. Calibration of Hot Film Probes

Three hot film probes were used in this project, as summarized in Table B.1. Probe 70919021 was always used as the upwind probe. Probe 70919027 was initially used in the test section, but failed during experimentation, and was replaced by probe 70919026. The MSE of each calibration curves is roughly an order of magnitude lower than the MSE of wakeNET. Calibration curves are shown for probes 70919021, 70919026, and 70919027 in Figure B.1, Figure B.2, and Figure B.3, respectively. Each calibration curve is a unique fourth order polynomial. Calibration was done using a TSI Model 1129 Automated Calibrator. Pressure measurements were obtained using an MKS Baratron type 220D pressure transducer.

Table B.1 - Summary of hot film probes

Probe Number	Location	MSE of calibration curve		
70919021	Upwind	1.96·10 ⁻⁵		
70919026	Test section	6.38·10 ⁻⁵		
70919027	Test section	2.89·10 ⁻⁵		

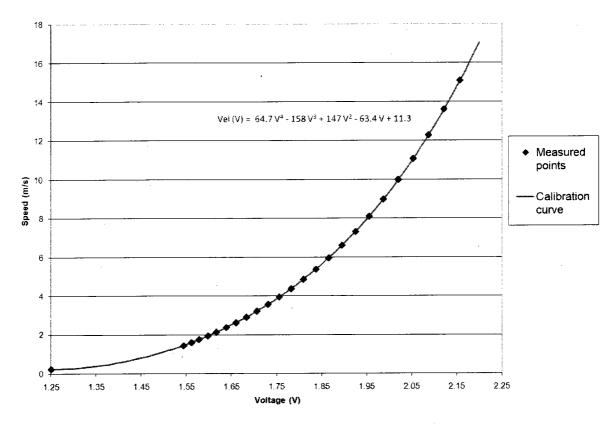


Figure B.1 – Calibration curve for probe 70919021

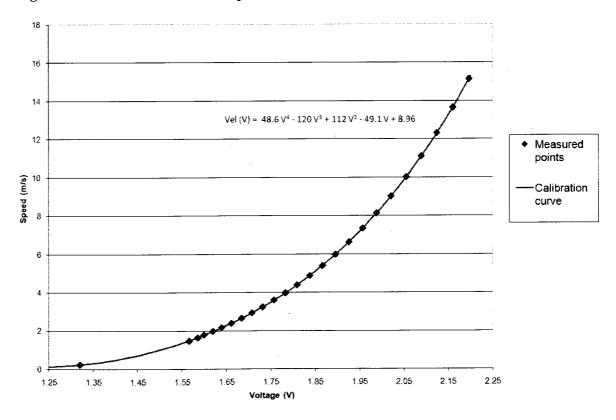


Figure B.2 – Calibration curve for probe 70919026

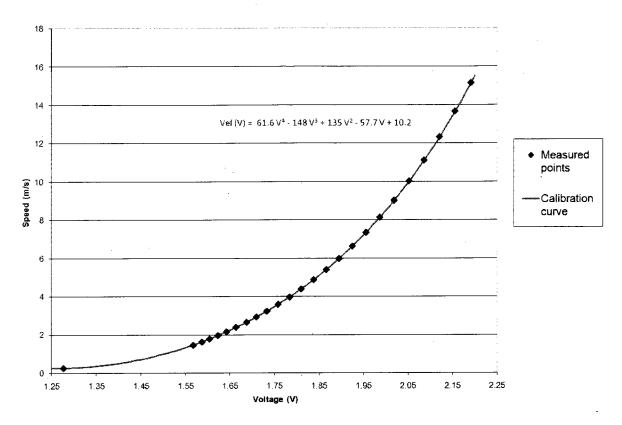


Figure B.3 – Calibration curve for probe 70919027

C. Development and Uniformity of Simulated Boundary Layer

The simulated atmospheric boundary layer (ABL) would ideally be uniform and fully developed. Here, the degree of 'uniformity' refers to the dependence of the mean velocity and turbulence intensity profiles on the lateral coordinate, z. A totally uniform ABL would be independent of z. Similarly, the degree of development refers to the dependence of the mean velocity and turbulence intensity profiles on the longitudinal coordinate, x. An ideal simulated ABL would be fully developed, that is, independent of x.

Figure C.1 shows the degree of uniformity in the flow at x=0 for seven configurations of spires. All configurations used small blocks spaced at 0.3 m as surface roughness elements. Uniformity U is defined in Equation C.1 as the ratio of mean flow speed V at z=306 mm to V at z=-306 mm (recall that z=0 is along the tunnel centerline, with positive to the right, facing upwind). 306 mm was chosen because it roughly represents the extents of the portion of the wind tunnel where measurements are made (further from the centerline, wall effects may become significant). All measurements were taken at the front of the test section, x=0.

$$U = \frac{V(z = 306 \text{ mm})}{V(z = -306 \text{ mm})}$$
(C.1)

To improve uniformity, a set of flow straighteners was added at the rear of the test section. Tests were performed with and without these flow straighteners for the 3 and 4 spire configurations. As well, a test was performed in which four spires were arranged with their triangular face on the ground, and their bases exposed to the wind. This was to investigate if changing from a triangular to a rectangular obstruction would improve uniformity; it did not. Flow tended to be faster at 306 mm than at -306 mm. Increasing the number of spires reduced uniformity. The addition of flow straighteners improved uniformity in both cases examined. The optimal configuration was determined to be with 3 spires and flow straighteners. The specific degree of uniformity with this configuration depends on x, y and z.

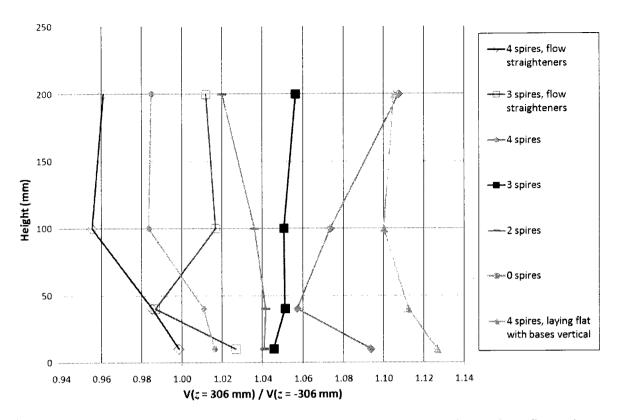


Figure C.1 – Uniformity of the simulated ABL at x = 0 for a variety of tunnel configurations

Figure C.2 shows mean velocity profiles at four points in the test section, using the configuration with three spires and flow straighteners. At both z locations, the velocity profile consistently shows greater shear at the upwind point (x = 0). This is evidence that the flow in the test section is not fully developed. All configurations showed similar results; even when no spires were present, the flow was still developing by the test section. The difference between the forward and rear profiles is considered acceptably small. It is generally around a few percent, and greatest at lower heights.

To summarize, the configuration with 3 spires and flow straighteners resulted in the greatest uniformity, and an acceptable level of development. This arrangement also produced satisfactory agreement with reference velocity profiles, turbulence intensity profiles, and energy spectra. This configuration was ultimately used for all wind tunnel tests. However, profiles do change slightly with x and z. To reduce experimental error, when calculating R_V and R_I as discussed in Chapter 3, an unsheltered measurement was taken at every point. (Alternatively, a

single unsheltered profile could be taken and used to normalize all sheltered values, but this would be less accurate, since some of the change in velocity would be due to changing location and not the obstacle.)

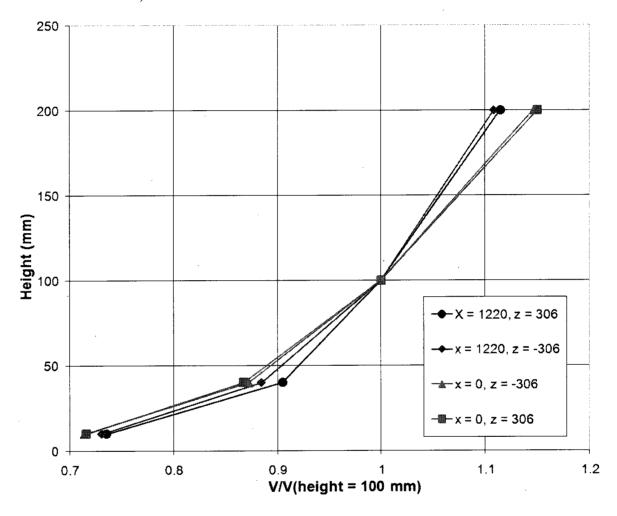


Figure C.2 - Development of flow in the longitudinal direction

D. Flow Unsteadiness in the Wind Tunnel

In the wind tunnel, the speed of the flow at any point will vary continuously. The magnitude of this variation is quantified by the turbulence intensity. To simulate the turbulence intensity of the atmospheric boundary layer, roughness generating elements (spires, blocks, and a grid) are used in the wind tunnel to cause a variation in the flow speed at all points.

Figure D.1 shows how the mean wind speed varies in the tunnel over a 1024 second time period, at a single point, when calculated using seven different averaging (or sampling) periods. No obstacle was present for this test. Roughness configuration was the same as for all tests, with a grid, 3 spires, and small blocks spaced at 0.3 m.

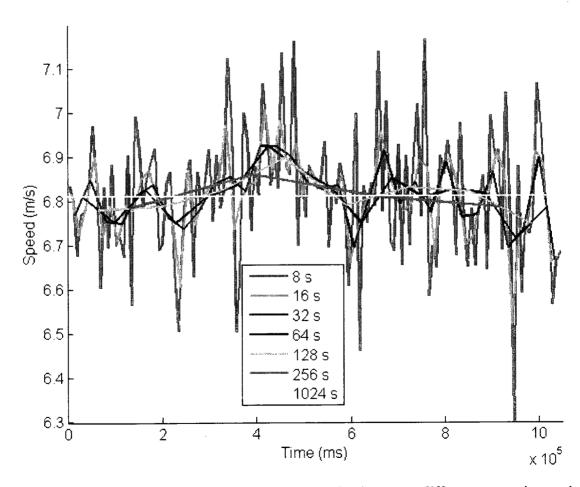


Figure D.1 - Mean wind speed over time, calculated using seven different averaging periods

Because the velocity at a point varies continuously, the mean velocity will depend on the period of time over which the flow is measured. Recall that two measurements are required to calculate each R_V and R_I value. Ideally, any difference between the sheltered and unsheltered wind speeds that are measured will be entirely due to the presence of the obstacle. However, as seen in Figure D.1, the mean wind speed at a point will vary with time, keeping all other factors constant. Part of the difference between the sheltered and unsheltered speeds will be due to this natural variation. This is one of the main sources of error in the wind tunnel experiments. It can be minimized by choosing an appropriate sampling time (or averaging period).

The sampling time used in this project was determined based on two competing criteria. The use of a longer sampling time will result in mean wind speeds that are closer to the true average value (defined as the mean over the entire 1024 second period). This can clearly be seen in Figure D.1. On the other hand, a shorter sampling time is preferable because it would allow the collection of more wind tunnel measurements, and therefore more training data, over the same time period.

The shortest averaging period in Figure D.1, 8 seconds, shows a fairly large variation in mean wind speed. It can be seen that some of the variation in wind speed occurs at periods as great as 256 seconds. Variations in wind speed at this low frequency are not expected to be generated from the spires. Rather, it is thought that there is a small variation in the power output of the motor powering the fan that drives the wind tunnel. Alternatively, it is possible that these larger scale variations have another explanation, such as changes in the flow inside the building, caused by activation of fans in the air circulation system, or external doors opening and closing. Regardless of their source, these large turbulence scales appears to be acting over time periods much greater than the variation in wind speed caused by the roughness generating elements.

With this in mind, an approach was developed in which each measurement in the test section was normalized by an upwind measurement obtained during the same time period. The intention was to "remove" or at least minimize variations in flow speed at larger timescales, such

that a shorter sampling time would provide an accurate measurement of the true mean wind speed at a point. The specific procedure followed is discussed in detail in Chapter 4. Figure D.2 shows the variation in mean normalized wind speed over the same time period as Figure D.1, using the same averaging periods. The normalized wind speed is defined as the ratio of the speed measured in the test section to the speed measured at the upwind sensor.

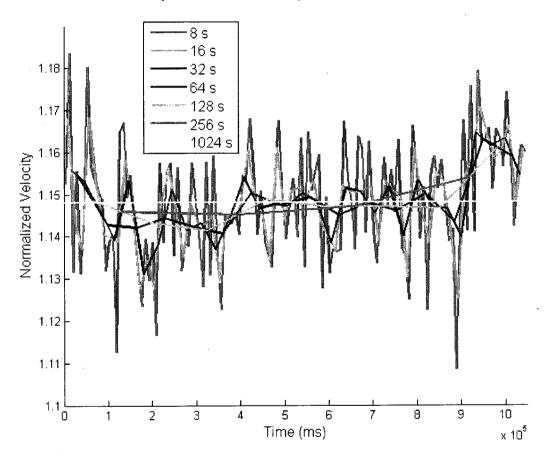


Figure D.2 – Mean normalized wind speed over time, no obstacle

Both Figure D.1 and Figure D.2 were measured in unsheltered flow. Similar plots for sheltered data show the same trends; as averaging period increases, variability in reported mean decreases. The mean percent difference seen with each sampling period is shown in Figure D.3, for both the normalized and non-normalized mean velocities, for sheltered and unsheltered measurements. Sheltered measurements were taken at a very sheltered position (x = 5, y = 2, z = 0, a = 0, AR = 9, PR = 1, RA = 0). Mean percent difference refers to the difference in mean value during the sampling period and the mean value during the entire period. It should be emphasized

that although the mean as calculated over the 8 second sample time is the true mean for that 8 seconds, it does not adequately represent the actual mean flow speed at that point.

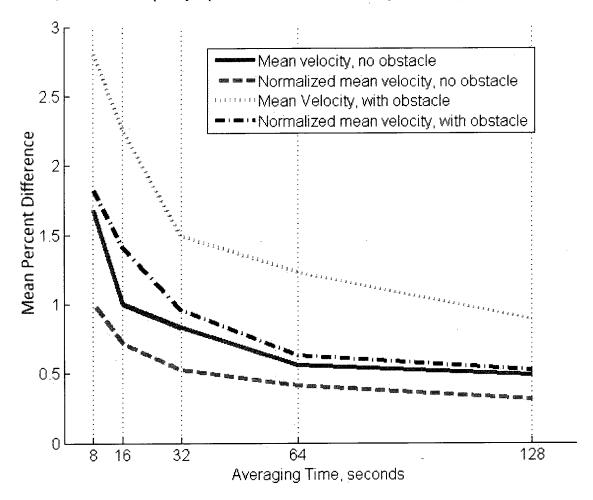


Figure D.3 - Variation of mean percent difference using 5 different averaging periods

The sheltered measurements show greater difference than the unsheltered measurements, as expected, since the sheltered turbulence intensity (velocity variation) is much greater than the unsheltered. Again, the measurements with the obstacle in place were taken at an extremely sheltered position. The magnitude of this difference is expected to decrease as sheltering effects diminish.

Since two measurements are required for each R_V and R_I value, one sheltered and one unsheltered, the mean difference for each value is expected to be the sum of the two differences. For a sampling period of 32 seconds, the mean difference is expected to be roughly 1.5%,

although it will be smaller at locations that experience less sheltering. For 64 seconds, this is reduced to roughly 1.0%.

Averaging times of 8 seconds and 16 seconds are not satisfactory, since they show too great of a natural variation. Averaging periods of 128 seconds and 256 seconds are too long, and would not allow obtainment of a satisfactory amount of training data. 64 seconds clearly shows less difference than 32 seconds, but it was decided that the improvement was not justified, since the cost would be reducing the amount of training data by roughly 50%. 32 seconds was ultimately used as the sampling time in all reported wind tunnel tests.

To summarize, the mean percent difference in each R_V and R_I value is expected to be roughly 1.5%. This can be thought of as the amount by which R_V and R_I will vary from their true values, on average, as a result of the variation in wind speed present in the tunnel. This value will be closer to 1.0% when sheltering effects are of low magnitude.

E. Reynolds Number Dependence of Flow in the Wind

Tunnel

The dependence of the flow on Reynolds number Re will vary with each unique case [28]. The critical value above which non-dimensional flow parameters can be considered to be independent of Re depends on the geometry of the bluff body, as defined by the shape and orientation of the obstacle. Typically, bluff body flows in a wind tunnel are assumed to be independent of Re above a value of around 2 to $3 \cdot 10^4$. Prior to the generation of training data, a wind tunnel study was carried out to investigate the critical range of Re, above which the results would be largely independent of Re. As stated, this specific range depends on the obstacle to some extent. Because all obstacles used here are similar in nature (all are prismatic bluff bodies), it is thought reasonable to assume that if the flow around one obstacle is independent of Re, then the flow around all obstacles is independent of Re.

All results reported here are velocity ratio R_V and turbulence intensity (*I*) values measured in the wake of a cube. Since cube orientation will have a large effect on the wake, Re dependence of the flow was investigated for azimuth angles of 0° (a face normal to the flow) and 45° (obstacle centre plane passing through two corners of the cube). Variation in Re was achieved by modifying the wind speed. Re is calculated based on the height of the cube and the upwind speed at cube height. Re dependence was investigated at x = 5, 7.5, 10, and 12.5, always with z = 0. Sample results are shown here. Figure E.1 shows how R_V varies with y at x = 5, z = 0, when $a = 0^\circ$.

The profile for case A, the lowest *Re* investigated, is clearly significantly different from the profiles measured at higher *Re*. Case B, C, and D measurements agreed fairly well, with C and D matching most closely. There is still some discrepancy between C and D but this is thought to be due to experimental error and not *Re* dependence. Measurements made at other points in the wake show similar results.

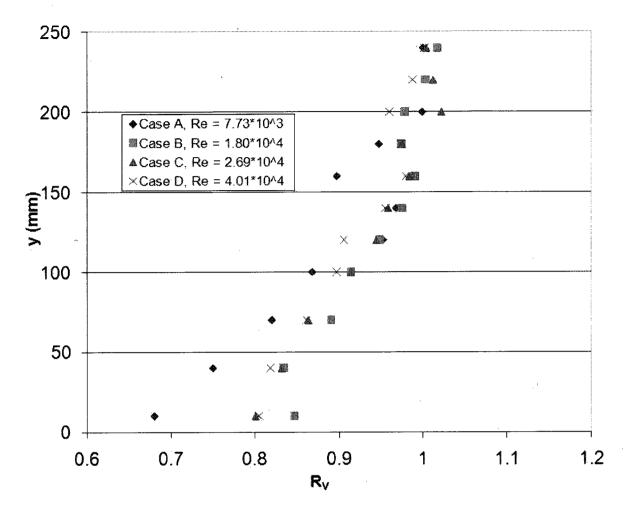


Figure E.1 – Vertical R_V profiles at a x = 5, z = 0, a = 0°, for four values of Re

Figure E.2 contains profiles of *I* in the wake of the cube, at the same four *Re* as Figure E.1.

Again, the case A profile shows variation from the other cases. Measurements from cases C and D agree very well.

Figure E.3 shows profiles of R_V in the wake of the cube with $a = 45^\circ$, at x = 7.5. This plot shows a greater discrepancy between the measurements for cases C and D than was seen in Figure E.1, although they are still generally within 2%. Because there is no apparent trend with Re, it is thought that this discrepancy is due to scatter in the data, caused largely by natural variation of speed in the wind tunnel (see Appendix D). If differences between the data sets were

due to Re effects, it is expected that there would be a trend with Re, which does not appear to be the case here.

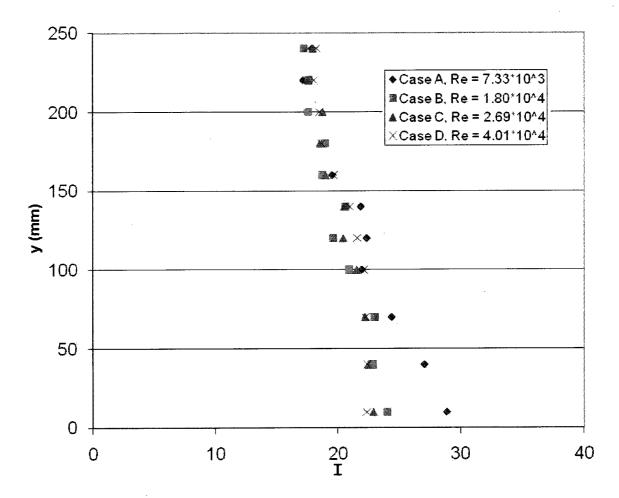


Figure E.2 – Vertical I profiles at a x = 7.5, z = 0, $a = 0^{\circ}$, for four values of Re

The variation of I with height is shown in Figure E.4, at x = 12.5, z = 0, with $a = 45^{\circ}$. Cases C and D show similar measurements. Aside from a few outlying points seen for cases A and B, all four cases appear to be in fairly good agreement.

 R_V and I profiles in the wake appear to collapse together as Re is increased. Re independence appears to be valid at higher Re investigated. The critical Re value at which R_V and I profiles are independent of Re varies depending on the cube orientation and quantity being looked at.

Typically this critical value is in the range of cases C and B, $1.80 \cdot 10^4$ to $2.69 \cdot 10^4$. In general, I profiles collapse together at higher Re than R_V profiles, and profiles in the wake of the cube at 45°

collapse at higher Re than profiles in the wake of the cube normal to the flow. Above the critical Re range, R_V and I profiles in the far wake are independent of Re. Any variation with Re is expected to be most evident at lower ranges of Re, so the assumption of Re independence likely holds for flow around full size buildings. This agrees with findings from the field experiment.

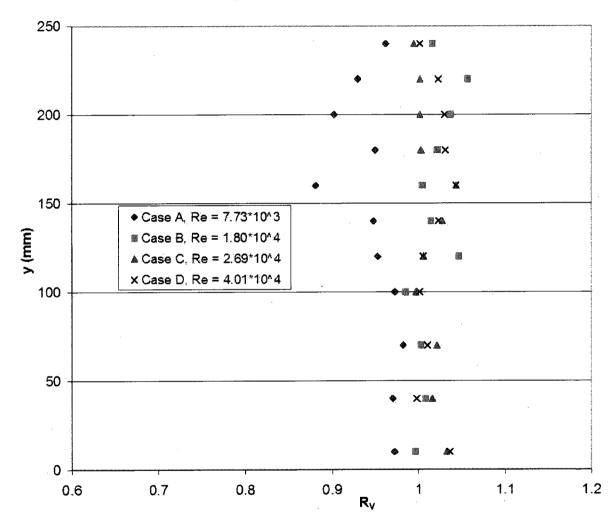


Figure E.3 – Vertical R_V profiles a x = 7.5, z = 0, $a = 45^\circ$, for four values of Re

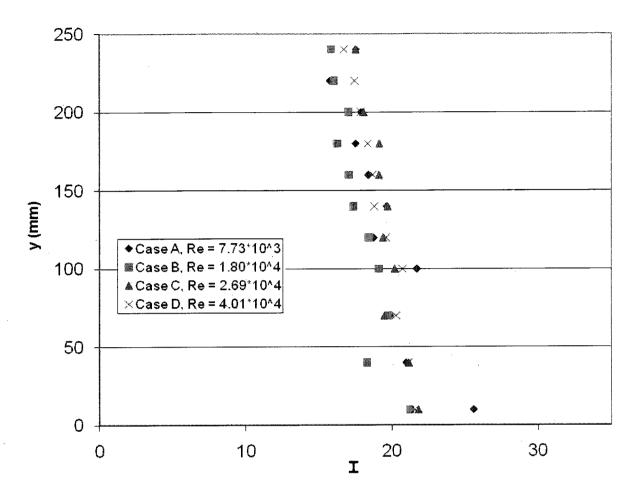


Figure E.4 – Vertical I profiles at a x = 12.5, z = 0, $a = 45^{\circ}$, for four values of Re

F. Uncertainty Analysis

This appendix investigates how uncertainty in velocity measurements propagates though the calculation of R_V and R_I . Wind tunnel and field experiments are treated separately. Methods of Coleman and Steele [41] are followed. Uncertainties values discussed are calculated or assumed for 95% confidence intervals, unless otherwise specified.

Wind Tunnel Experiments

The measured quantity in the wind tunnel is the bridge voltage in the sensor circuit, which is directly related to the flow velocity at the probe location; see [40] for details. The bridge voltage is automatically corrected for ambient temperature, which is measured by a thermocouple. The relationship between wind speed at the probe location and the measured bridge voltage is expressed by the calibration equation. Each sensor has a unique calibration equation in the form of a fourth order polynomial (see Appendix B), obtained using a TSI Model 1129 Automated Air Velocity Calibrator. During the calibration, velocity is calculated based on the stagnation pressure, measured using an MKS Baratron type 220D pressure transducer. Main sources of uncertainty in the measurement of instantaneous velocity are expected to be:

- i) The fit (or accuracy) of the calibration equation
- ii) Uncertainty in the pressure transducer measurements used to generate the calibration equation
- iii) Misalignment of the probe sensing area not in intended position
- iv) Voltage measurement error
- v) Temperature measurement error, or other changes in conditions not taken into account
- vi) Unsteadiness in the flow, as discussed in Appendix D. Applies only to mean flow measurements

It is assumed that the voltage and temperature measurement errors are negligible compared to other sources of uncertainty. For instantaneous readings, this leaves three main sources of error, which are pressure transducer uncertainty, the fit of the calibration equation, and misalignment of the probe. The magnitudes of these uncertainties are discussed below.

The calibration equations for each of the three probes are shown in Appendix D. There is an error associated with each measurement point. Each calibration curve was created based on 25 measured voltages, and the corresponding velocity. Based on the 25 error values available, the uncertainty in the calibration curve can be estimated, assuming that the accuracy calibration curve is consistent at all velocities. In general, calibration curves fit the data very well. Using a 95% confidence interval, the amount by which any measurement varies from the calibration curve is estimated to be 0.15%, 0.18%, and 0.15% for probes 70919021, 70919026, and 70919027, respectively. An uncertainty of 0.2% will be used for the fit of the calibration equation for all probes.

Without detailed knowledge of the flow field, it is difficult to quantify how alignment errors will affect the uncertainty of the velocity. All probe locations were measured using rulers. Assuming that one half the least division is a reasonable estimate of the positioning uncertainty, actual probe positions will be within \pm 0.5 mm of the intended position. A rough estimate of how a vertical positioning error will affect the velocity reading can be made by assuming a value for local α . For example, the greatest α value obtained for the 9-1 block was 1.74, at x = 3, z = 0, a = 0, between y = 1.4 and 1.8. This is the average shear between these two points. Assuming that this value is valid at y = 1.4, and that the probe is 0.5 mm (or 0.01 h) from its intended position (so at y = 1.39), the ratio of velocity at the actual to intended position is 0.988, for an error of 1.2%. Although the shear is large, the error is mostly negated by the small ratio of actual height to intended height. At lower heights, where this ratio is larger, the shear is generally much lower. 1.2% is a worst case scenario in several respects: the position was assumed to be off by the maximum expected, 0.5 mm, and the maximum shear observed was assumed. Assuming $\alpha = 0.41$

(observed between y = 1.4 and y = 1.6 at x = 20, z = 0, a = 0 for the same block as above), the ratio of velocity at the actual to intended position is 0.997, for an error of 0.3%. This is still a high level of error, although not the worst case.

To summarize, the uncertainty due to alignment error is very difficult to relate to uncertainty in a velocity measurement. The magnitude of the effect will depend greatly on structure of the local flow field. It should be pointed out that misalignment only affects values in the test section, since the upwind probe is never moved, and its height is not used in any calculation. Going forward, an uncertainty value of 0.3% is used for the effect of misalignment error on velocity. It is emphasized that this is at best an educated guess, and is thought to be an overestimate for the majority of measurements, which is appropriate for a 95% confidence interval.

Before calibration, the pressure transducer was zeroed to reduce bias. In the manual, the accuracy of the instrument is estimated as a function of temperature. At a temperature of 20°, the uncertainty in the measurement is estimated to be 0.4%. This contributes to the error in the velocity measurement.

The overall uncertainty of an instantaneous flow measurement is estimated to be 0.5%, considering the uncertainty values determined for each source of error. Although the uncertainty at the upwind location should be lower, since alignment is not a factor, 0.5% is used for both probes, as a conservative estimate. As mentioned, there is also uncertainty associated with unsteadiness in the flow. This is not accounted for in the calibration, since calibration was (necessarily) done in a much less turbulent flow (I < 1%). Uncertainty resulting from unsteadiness is not an error, but it is still an uncertainty which should be taken into account, since it shows how the measured mean can vary from the true mean at a point. Table 5.1 summarizes the uncertainties present for each hot film reading.

Table F.1 - Summary of sources of uncertainty for each hot film reading

Source of Error / Uncertainty	Value of uncertainty		
Fit of calibration	0.2%		
Pressure transducer	0.4%		
Misalignment	0.3%		
Voltage measurement	0 (assumed)		
Temperature measurement	0 (assumed)		
Total, for each velocity reading	0.5%		

Uncertainty in R_V

The calculation of R_V is described in Chapter 4. R_{VI} is calculated using Equation 4.1. Neglecting effects from unsteadiness, for now, the uncertainty in both $\overline{V_1}$ and $\overline{V_0}$ is assumed to be 0.5%., which is the same as that for an instantaneous measurement in the test section. If the flow was entirely steady, then the uncertainty in the mean flow would be almost entirely due to bias; since each mean speed consists of 32768 (or $32 \cdot 2^{10}$) velocity measurements, the precision error of the mean would be negligible. However, this approach is not applicable here, since the wind speed actually varies over time.

Using the method described by Coleman and Steele [41], as shown in Equation F.1, the uncertainty in R_{VI} is 0.7%.

$$\left(\frac{U_{RV1}}{R_{V1}}\right)^2 = \left(\frac{U_{\overline{V1}}}{\overline{V_1}}\right)^2 + \left(\frac{U_{\overline{V0}}}{\overline{V_0}}\right)^2 \tag{F.1}$$

Since upwind and test section mean velocities are measured at the same time, effects from unsteadiness should be considered for the ratio $\overline{V_1}/\overline{V_0}$, instead of for each separate mean velocity. Appendix D investigates how the normalized mean velocity in sheltered and unsheltered flow varies with sample time. Based on mean velocities obtained with a sample time of 32 seconds,

which was used in this project, the variation of $\overline{V_1}/\overline{V_0}$ is 1.4% and 2.3% for unsheltered and sheltered flow, respectively, using a 95% confidence interval (recall that at a sheltered location, the flow speed will vary to a greater extent). The sheltered value of 2.3% is for a very sheltered position; as sheltering effects are reduced, the uncertainty will become closer to 1.4%. Combining the uncertainties in R_{VI} of 0.7% and 1.4%, the overall uncertainty in R_{VI} becomes 1.6%. Similarly, for R_{V2} , the overall uncertainty becomes 2.4%. In both cases, the uncertainty in the measurement is dominated by the unsteadiness of the flow, rather than the uncertainties regarding each individual velocity measurement. The uncertainty in R_V can then be estimated based on the uncertainties of R_{VI} and R_{V2} , as shown in Equation F.2.

$$\left(\frac{U_{RV}}{R_{V}}\right)^{2} = \left(\frac{U_{RV1}}{R_{V1}}\right)^{2} + \left(\frac{U_{RV2}}{R_{V2}}\right)^{2} \tag{F.2}$$

The resulting uncertainty in R_{ν} is 2.9%. Table F.2 summarizes the uncertainty of each quantity used to calculate R_{ν} .

Table F.2 – Uncertainties of quantities used to calculate R_V

Uncertainty	
0.5%	
1.6%	
2.4%	
2.9%	
	0.5% 1.6% 2.4%

A simpler method of calculating R_V is to simply take the ratio $\overline{V_2}$ / $\overline{V_1}$, ignoring the upwind probe. Compared to the method in which mean velocities are normalized, the uncertainty associated with instantaneous velocity measurements is identical. However, unsteadiness in the flow is a larger factor, with values of 2.1% and 4.1% for unsheltered and sheltered means,

respectively. Resulting uncertainty in R_{ν} is 4.7%, which is significantly greater than the uncertainty when measurements are normalized by the upwind flow speed.

Uncertainty in R_I

The calculation of R_l is described in Chapter 4. I is calculated using Equation 2.7. Musselman (REF) provides an estimate of the precision error P in V_{rms} , shown in Equation F.3.

$$\frac{P_{Vrms}}{V_{rms}} = \frac{z_{\alpha}/2}{(2N)^{1/2}}$$
 (F.3)

 $z_{cl}/2$ is the standard normal variate of 1.96 for a 95% confidence interval. N is the number of samples, which again is 32768. The precision error is then 0.8%. Musselman [23] also states that there will be bias error in V_{rms} due to a small percentage of the flow being in the reverse direction. Based on Musselman's estimate of bias error in the measurement of V_{rms} , 1.5% is used here at the 95% confidence interval for bias. The total uncertainty in V_{rms} is then 1.7%. Following the approach of Coleman and Steele [41], uncertainties in I will propagate according to Equation F.4.

$$\left(\frac{U_I}{I}\right)^2 = \left(\frac{U_{Vrms}}{V_{rms}}\right)^2 + \left(\frac{U_{\overline{V}}}{\overline{V}}\right)^2 \tag{F.4}$$

The uncertainty of I is 1.8%, which is applicable to all measurements of I. This does not consider effects related to unsteadiness, which are taken into account below. For now, neglecting unsteadiness, the uncertainty of R_{II} is given by Equation F.5. Uncertainty related to R_{I2} is found the same way.

$$\left(\frac{U_{RI1}}{R_{I1}}\right)^2 = \left(\frac{U_{I0}}{I_0}\right)^2 + \left(\frac{U_{I1}}{I_1}\right)^2 \tag{F.5}$$

The uncertainty of both R_{II} and R_{I2} is 2.5%, in addition to any uncertainty associated with unsteadiness. The unsteadiness of R_{II} and R_{I2} was investigated in the same manner as it was for R_{VI} and R_{V2} . It was found that for a 95% confidence interval, the uncertainties associated with unsteadiness for I_{I}/I_0 and I_{2}/I_0 are 5.1% and 7.0%, respectively, resulting in total uncertainties of 5.7% and 7.4% for R_{II} and R_{I2} . The total uncertainty in R_{I} is 9.3%, as calculated using Equation

F.6. Note that this value is significantly greater than the uncertainty calculated for R_V . Table F.3 summarizes the uncertainties for each quantity, as discussed above.

$$\left(\frac{U_{R1}}{R_{I}}\right)^{2} = \left(\frac{U_{RI1}}{R_{I1}}\right)^{2} + \left(\frac{U_{RI2}}{R_{I2}}\right)^{2} \tag{F.6}$$

Table F.3 – Uncertainties of quantities used to calculate R_I

Quantity	Uncertainty			
V_{rms}	1.7%			
I, neglecting unsteadiness	1.8%			
R_{II} , I_I / I_0	5.7%			
R_{12} , I_2 / I_0	7.0%			
R_{I}	9.3%			

An alternatively approach to calculating R_l is to take the ratio I_2/I_l , which does not involve the upwind probe. In this case, the unsteadiness values associated with I_l and I_2 were experimentally determined to be 6.9% and 7.3%, respectively, resulting in total uncertainty values of 7.1% and 7.5%. The uncertainty in R_l is then of 10.3%. Note that normalizing measurements by the upwind probe only results in a slightly smaller uncertainty when calculating R_l . For R_l , the improvement was much more significant. This difference is mainly due to the relatively large uncertainty associated with I, when compared to that associated with \overline{V} . Estimates made here are consistent with measurements; much more scatter was evident in R_l values than in R_l values.

Field Experiments

Three unique sensor models were used in the field experiments: the CSAT3 sonic anemometer, the RM Young sonic anemometer, and the NRG#40c cup anemometer. As in the wind tunnel, a large part of the uncertainty in each field measurement will be due to variation in

the flow, as opposed to any error with the sensor. A field measurement may not be a good representation of the true mean at that point, even if the sensor could measure the flow with perfect accuracy. An important difference between the wind tunnel experiment and the field experiment lies in the fact that in the wind tunnel, only one data point was measured at each measurement point, while in the field, many data points were obtained for each measurement point. An analysis of how well mean velocities measured in the field converge to the true mean is included in Chapter 5. Another important difference is that in the field experiment, sheltered and unsheltered velocity values are measured over the same time period, which will tend to greatly reduce effects associated with unsteadiness. Here, uncertainty associated with unsteadiness in the flow is not considered. The extent to which the field measurements represent the true mean at a point should be determined based on this appendix as well as the convergence analysis in Chapter 5.

CSAT3

The CSAT3 was set to measure at 60 Hz. The datalogger collects at 20 Hz. This means that each value collected by the datalogger is actually an average of three values. The 30 second averaging period used is the average of 1800 values. From the CSAT3 manual, the precision error is given as < 2% of the reading. Equation F.7 relates the precision error of a single measurement to the precision error of the mean of many measurements.

$$P_{\overline{V}} = \frac{P_{V}}{\sqrt{N}} \tag{F.7}$$

For N=1800, $P_{\overline{V}}=0.05\%$, essentially negligible. The total uncertainty in the CSAT3 measurements is almost entirely due to bias. The bias error is specified as < 0.04 m/s. Assuming a wind speed of 4 m/s, which was the minimum wind speed used, the bias error is 1%. This means that $U_{\overline{V}}=1\%$.

RM Young

The RM Young sonic anemometer measures wind speed at 20 Hz, resulting in 600 velocity measurements per averaging period. From the manual, the precision error is specified as 1%. Using Equation F.7, the precision error of the mean velocity over the averaging period is 0.04%, again, it is essentially zero because of the large number of measurements made. The bias error is specified as 0.05 m/s. Assuming a wind speed of 4 m/s, $U_{\overline{\nu}} = 1.3\%$.

NRG #40c

The datalogger is set to measure the wind speed from each NRG cup anemometer at 2 Hz. Velocity measurements are obtained by relating the wind speed to the rotational speed of the cups using a calibration curve, which is supplied by the manufacturer. From the manual, the accuracy is specified to be 0.1 m/s. It is assumed that this value takes into account both precision and bias error. The magnitude of the bias error will depend on the calibration curve. The bias error is assumed to be 0.1 m/s, which is a worst case scenario. At 4 m/s, the uncertainty in velocity measurements from the cup anemometer is 2.5%.

Calculation of R_V

 R_V is the ratio $\overline{V_{SH}}$ / $\overline{V_{UNSH}}$, where both mean velocities are measured over the same 30 second time period. To estimate the uncertainty of R_V , it is necessary to consider which anemometers the sheltered and unsheltered velocities are taken from. All R_V values reported for a height of 3 m use a CSAT3 for the unsheltered value. All R_V values reported for a height of 6 m use an NRG for the unsheltered value. Table F.4 summarizes the uncertainty in the $\overline{V_{SH}}$, $\overline{V_{UNSH}}$, and R_V at each anemometer location. The position of each anemometer relative to each obstacle is described in Chapter 5.

Table F.4 – Summary of uncertainties in R_V at each sensor location

Uncertainty in $\overline{V_{SH}}$	Uncertainty in $\overline{V_{UNSH}}$	Uncertainty in R_V		
1%	1%	1.4%		
1%	1%	1.4%		
1%	1%	1.4%		
1.3%	1%	1.6%		
2.5%	2.5%	3.5%		
2.5%	1%	2.7%		
2.5%	2.5%	3.5%		
2.5%	2.5%	3.5%		
2.5%	2.5%	3.5%		
2.5%	1%	2.7%		
	1% 1% 1% 1% 1.3% 2.5% 2.5% 2.5% 2.5%	1% 1% 1% 1% 1% 1% 1.3% 1% 2.5% 2.5% 2.5% 2.5% 2.5% 2.5% 2.5% 2.5% 2.5% 2.5% 2.5% 2.5%		

The uncertainty in R_V values measured in the field experiment ranges from 1.4% to 3.5%, depending on the location of interest. This is not considering uncertainty associated with variation in the flow between the sheltered and unsheltered towers.

Calculation of R_I

 R_l is the ratio I_{SH}/I_{UNSH} , where both turbulence intensities are measured over the same 30 second time period. The uncertainty in V_{rms} is determined using Equation F.3, and is assumed to apply to both the sheltered and unsheltered cases. For the CSAT3, the RM Young, and the NRG, the precision error in V_{rms} is estimated to be 3.3%, 5.6%, and 17.9%. Regarding the NRG anemometer, this assumes that the instrument can accurately respond to wind at a frequency of 2 Hz. The validity of this assumption depends on the wind speed; at greater wind speeds, such as those above the cut off, 2 Hz is a valid sampling frequency. Bias error is assumed to be 1%, 1.3%, and 2.5%, for the CSAT3, the RM Young, and the NRG. These are the same values used for bias

in mean velocity measurements. The total uncertainties in V_{rms} for the CSAT3, the RM Young, and the NRG are 3.4%, 5.7%, and 18.1%. Table F.5 summarizes the uncertainty of I_S , I_U , and R_I values at each sensor location.

Table F.5 – Summary of uncertainties in R_I at each sensor location

Uncertainty in I_S	Uncertainty in I_U	Uncertainty in R _I 4.8%	
3.4%	3.4%		
3.4%	3.4%	4.8%	
3.4%	3.4%	4.8%	
5.7%	3.4%	6.6%	
18.1%	18.1%	25.6%	
18.1%	3.4%	18.4%	
18.1%	18.1%	25.6%	
18.1%	18.1%	25.6%	
18.1%	18.1%	25.6%	
18.1%	3.4%	18.4%	
	3.4% 3.4% 3.4% 5.7% 18.1% 18.1% 18.1% 18.1%	3.4% 3.4% 3.4% 3.4% 3.4% 3.4% 5.7% 3.4% 18.1% 18.1% 18.1% 18.1% 18.1% 18.1% 18.1% 18.1% 18.1% 18.1%	

These are high values, especially when R_l is based entirely on I values taken from cup anemometers. However, recall that these are the 95% confidence interval for each new mean value collected. When multiple measurements are obtained, the uncertainty will decrease with $N^{l/2}$. Another source of error in R_l is the distance between the sheltered and unsheltered sensors. This is discussed in more detail above. Essentially, R_l values are corrected by baseline values, obtained when no obstacle was in place, to reduce the magnitude of this error.

G. Multiple Wake Interactions

Approaches Considered

Five approaches to predicting R_{k} in the wake of an obstacle group are proposed, based on Musselman's work, Taylor and Salmon's method, and the single isolated structure (SIS) model developed in Chapter 6. For simplicity, R_{l} is not considered here. Predictions are made using each method and compared to wind tunnel data. All approaches rely on wakeNET to make accurate predictions for single obstacles. This has the disadvantage that some error in the prediction may be associated with the SIS model and not the prediction method itself. On the other hand, this can be thought of as further validation, and is a good test of wakeNET's capabilities. Based on wakeNET's high degree of accuracy in making predictions for obstacles similar to those previously seen, and the validation for new obstacles in Chapter 6, confidence in wakeNET's predictions is fairly high.

The first method is to predict the wake effects of each obstacle in the group separately, and use superposition to obtain the predicted R_{ν} . This is referred to here as linear combination (LC), and follows the process used by Taylor and Salmon. Predictions are made using wakeNET for each SIS.

The second approach is to replace the obstacle group with a single larger obstacle (SLO). An envelope is created around the obstacle group such that all obstacles lie inside, as seen in Figure G.1 and Figure G.2 (this is similar to the concept of a virtual source). a, AR and PR are defined accordingly. RA is defined as the average roof angle of each obstacle. WakeNET is used to make R_V predictions for the SLO; these are the assumed wake characteristics of the group. The origin, where (x, z) = (0, 0), halfway between the limits of the SLO.

The next two approaches are based on the prediction for a SLO, as described above. In both methods, R_V is predicted using the SLO approach, and then corrected to account for the physical differences between the obstacle cluster and the SLO.

The third method uses a correction factor based on Musselman's work. Recall that Musselman created an empirical model that can predict the velocity deficit in the wake of an obstacle group, but only on the centerline (z = 0), at y = 1, and only when the group is a single row of obstacles with constant AR and S. This makes the model fairly limited. However, by comparing the velocity deficit predicted for the SLO along the centerline to that predicted by Musselman, a correction factor can be obtained, which should incorporate effects associated with the spacing. This correction factor is referred to as the Musselman correction factor (MF), which is defined in Equation G.1.

$$MF(x) = \frac{D_{V,M}(x)}{D_{V,W}(x)} \tag{G.1}$$

MF is calculated as a function of x. $D_{V,m}$ and $D_{V,W}$ are the centerline velocity deficits predicted by Musselman's model and wakeNET, respectively, at y = 1.0 h. For Musselman's predictions, the average AR and S of the group are used. This approach assumes that the difference between a group of obstacles and a SLO the size of the envelope of the group does not depend on y, z, or a. As well, it assumes that Musselman's model is valid for groups with nonconstant S and AR. If these assumptions are fair as a rough approximation, then the prediction method should be reasonably accurate. At all locations in the wake, the velocity deficit predicted by wakeNET for the SLO is corrected by MF. Typically, MF is much less than 1, meaning that the predicted velocity deficit in the wake of the group will be less than that predicted for a SLO.

The fourth approach is again based on predictions for a SLO. The width of the group W is calculated, normal to the wind direction. The width of each gap in the group S is also calculated, again, normal to the wind direction. The porosity p is defined in Equation G.2 as the sum of the gap widths divided by the total width of the obstacle group. The porosity is used to directly correct the velocity deficit predicted for a SLO.

$$p = \frac{\sum S}{W} \tag{G.2}$$

The fifth and final approach considered is to simply take the average of the LC prediction and the SLO prediction. While somewhat arbitrary, this approach is based on the expected relative magnitudes of the two predictions. Based on Musselman's wind tunnel results, it is clear that in the far wake, the LC method will greatly underestimate the velocity deficit. This is mainly because the effect of changing AR is non-linear; doubling the AR much more than doubles the extents and magnitude of the wake. Intuitively, it is expected that the SLO approach will overestimate wake effects, since essentially, the source of the wake is becoming larger. However, as seen in the wind tunnel results, there are exceptions to this due to the complex nature of bluff body flows and interacting wakes.

Wind Tunnel Testing

BLWT tests were carried out to measure R_V and R_I in the wakes of several obstacle clusters. The ABL was simulated using the same method as in Chapter 4. As well, the testing procedure was identical to that described in that Chapter. Two main obstacle groups were investigated. The layout of cluster 1 is shown in Figure G.1.

Cluster 1 consisted of the 1-2 block, the 3-1 block, and the 1-0.5 block. All three obstacles were of the same height. To investigate the effects of spacing, S_X and S_Z were varied. Details of the tests conducted using cluster 1 are included in Table G.1. Experiments were designed such that x, z, and a were varied. Wind directions simulated are shown in Figure G.1.

For each test in Table 6.1, vertical profiles of R_V were measured at y = 0.5, 1.0, 1.5, 2.0, 2.5, and 3.0 h. Where multiple a or S values are indicated, a profile was measured for each value. In tests 1 to 4, the 1-0.5 block was not present. Tests 5 and 6 were carried out with and without the 1-0.5 block to investigate how a smaller downwind obstacle affects the wake.

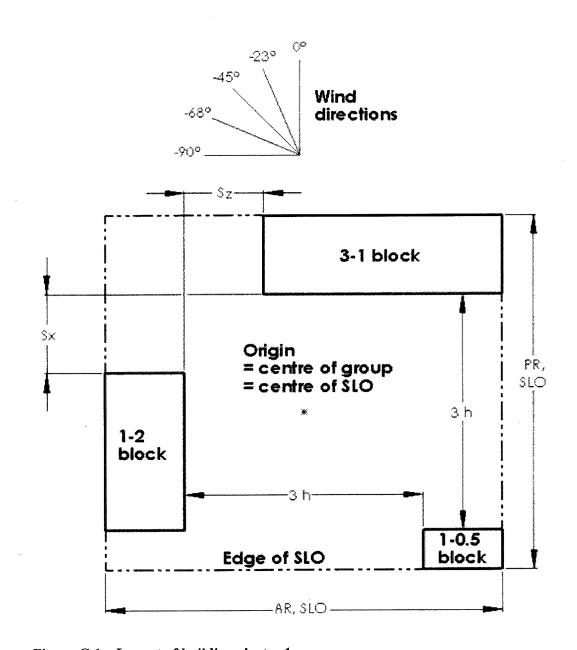


Figure G.1 – Layout of building cluster 1

Table G.1 - Details of tests conducted using cluster 1 to generate the wake

Test	X	z	а	S_Z, S_X	Number of points
1	10	0	0	(0.6, 0), (1.5, 0), (3.0, 0),	30
				(0.6, 1.0), (0.6, 2.0)	
2	18.2	0	0	(0.6, 0), (1.5, 0), (3.0, 0),	30
				(0.6, 1.0), (0.6, 2.0)	
3	10	0	45°	(0.6, 0), (1.5, 0), (3.0, 0),	30
				(0.6, 1.0), (0.6, 2.0)	
4	15	-2	0°, -23°, -45°,	(0.6, 0)	30
			-68°, -90°		
5	12	-2	0°, -23°, -45°,	(2.0, 0)	60
			-68°, -90°		
6	12	-2	0°, -23°, -45°	(1.0, 0)	36

The layout of the second cluster of buildings investigated is shown in Figure G.2. All three buildings have the same AR and PR. S_Z was varied during each test to examine its effect on the wake. The orientation of the cluster was also varied. Table G.2 contains the details of all tests performed to measure the wake of cluster 2. For each test in Table G.2, R_V was measured at y = 0.5, 1.0, 1.5, 2.0, 2.5, 3.0, 3.5, and 4.0.

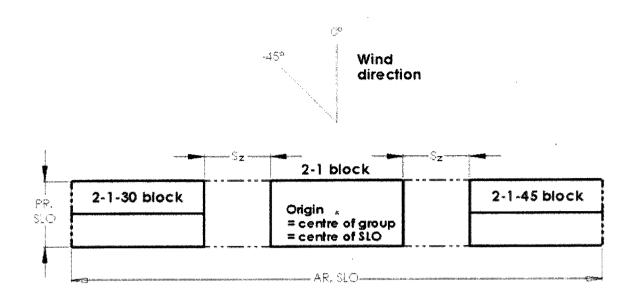


Figure G.2 - Layout of building cluster 2

Table G.2 - Details of tests conducted using cluster 2 to generate the wake

Test	x	Z	a	S_Z	Number of points
7	20	0	0°	0.5, 1.0, 2.0	24
8	20	0	45°	0.5, 1.0, 2.0	24
9	20	-3	45°	0.5, 1.0, 2.0	24

In total, 216 points were measured in the wake of cluster 1 and 72 points were measured in the wake of cluster 2. It is recognized that since only two distinct building clusters are investigated, any findings here may not be applicable to clusters that are significantly different. However, by determining how best to predict R_V with varying S_X , S_Z , and a, it is hoped that results for other clusters will be comparable to those obtained here.

Results

The mean absolute error and mean error of the five prediction methods are shown in Table G.3.MAE is the mean absolute error, as defined in Equation 6.3. ME is the mean error, which is simply the average of the error. Both are reported as percentage error in predicting R_{ν} . MAE

indicates the accuracy of the prediction method. ME is useful because it enables comparison of the relatively magnitude of errors using each prediction method.

Table G.3 - MAE and ME of each prediction method

Method description	LC	SLO	SLO, MF	SLO, Porosity	Average, LC and SLO
Method number	1	2	3	4	5
MAE	3.8%	5.2%	3.5%	3.9%	3.6%
ME	1.8%	-2.6%	1.6%	-0.9%	-0.4%

Overall, method 3 was found to be the most accurate, followed closely by method 5. On average, superposition overestimates R_V , as indicated by its ME. This is supported by evidence from Musselman, which indicates that the wake of an interacting group of cubes is much greater in extents and magnitude than the superposition of each cube's individual wake.

Predictions made by replacing the group with a SLO tend to under predict R_{ν} . The ME of method 5 is closest to zero, meaning that out of the five methods examined, it has the least bias. Errors made using this method tend to slightly under predict R_{ν} , which is thought to be preferable to over predicting its value.

The choice of best prediction method appears to depend on details of the specific case, mainly, spacing and downwind distance. Figure G.3 and Figure G.4 show how predicted velocity deficit (D_V) profiles compare to those measured in the wind tunnel, during tests 1 and 2, respectively. In both figures, z = 0, a = 0, and S = 1.5 h. In Figure G.3, x = 10, while in Figure G.4, x = 18.2.

At x = 10, method 5 appears to be the best at lower heights, although no method works particularly well. At greater heights, method 3 makes the most accurate predictions. Method 1 (LC) appears to follow the same trend as the wind tunnel data, but it consistently underestimates the velocity deficit.

Again at x = 18.2, Figure G.4, no method is able to reproduce the full profile accurately. Above a height of y = 1.5 h, method 1 appears to produce the most accurate results, although the wake has mostly dissipated by this point. At y = 0.5 h, the velocity deficit is actually much greater for the group than for the single obstacle. This surprising result was confirmed through wind tunnel testing of a single obstacle of appropriate size. Recall that all methods rely on wakeNET predictions; it was first considered, and later disproved, that this excess was a bad prediction. Further testing indicates that this type of result occurs semi-regularly, and most often at lower heights. A group can generate a greater velocity deficit than a SLO that envelopes all obstacles in the group.

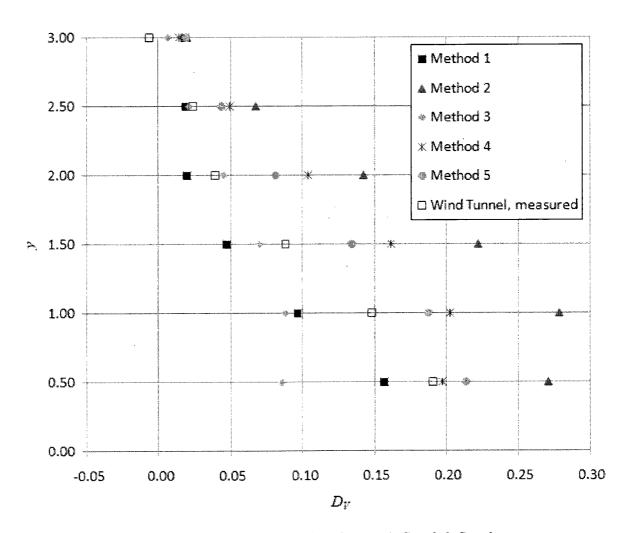


Figure G.3 – Predicted and measured D_V profiles for test 1, $S_Z = 0.6$, $S_X = 0$

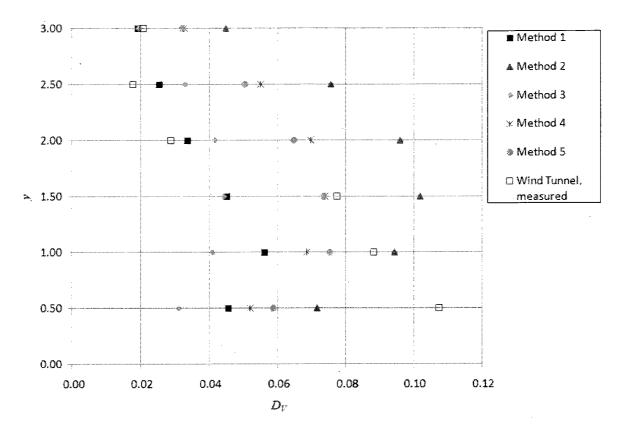


Figure G.4 – Predicted and measured D_V profiles for test 2, $S_Z = 0.6$, $S_X = 0$

Figure G.5 shows D_V predictions for test 9, with a spacing of 1.0 h. The obstacle group created a greater wake than that predicted for a SLO, but only slightly. This test was performed at x = 20, with a = -45. At this orientation, there are no gaps normal to the flow direction, as can be seen in Figure G.2. This means that both the p and MF are 0, which is why predictions made using methods 3, 4, and 5 are identical. Predictions made for the SLO are quite good, aside from at y = 0.5 h. Method 1 greatly underestimates D_V , which is consistent with virtually all comparisons performed at x = 20, when the spacing was such that the wakes would interact.

Figure G.6 shows DV profiles for test 7, with a spacing of 2.0 h. All methods over predict the velocity deficit. A small speed up effect was consistently measured, but never predicted. At this spacing, interaction between the obstacle wakes is minimal, which contrasts with Figure G.5, where significant interaction can be seen. This is fairly consistent in nearly all tests conducted: at greater spacings, methods based on replacing the group with a SLO perform worse, while

superposition becomes slightly better. Musselman's findings support this. At greater spacings, obstacle wakes interact much less, meaning that superposition becomes better at predicting wake effects. Musselman's model, and therefore method 3, is only recommended for use when spacing is less than 1.5 h.

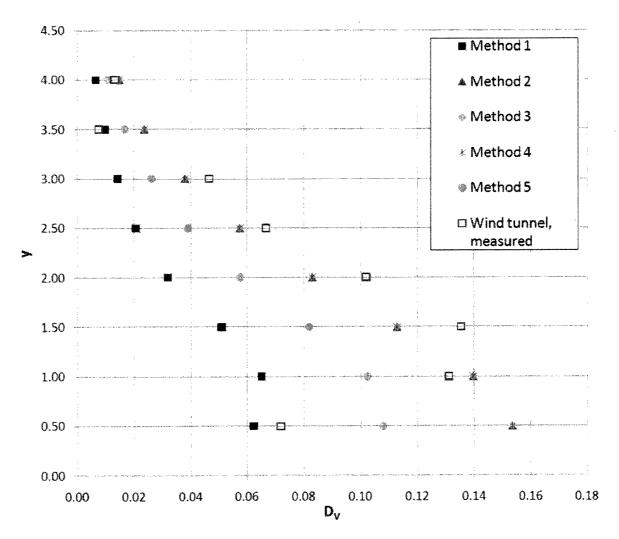


Figure G.5 – Predicted and measured D_V profiles for test 9, $S_Z = 1.0$ h

The validity of neglecting smaller upwind obstacles is important, since potentially, this can simplify the obstacle group. Figure G.7 shows D_V predictions and measured profiles for test 6, at a wind angle of 0° . This test was performed with and without the 1-0.5 block present, at the location shown in Figure G.1. Clearly, the 1-0.5 block has an effect on the wake. Effects are greater at lower heights. Higher up, the presence of the block appears to slightly increase the

speed of the flow. Alternatively, for some wind angles and spacings, the presence of the 1-0.5 block had no noticeable effect on the wake. In general, it is probably safe to neglect smaller downwind obstacles when predicting R_{ν} at greater heights.

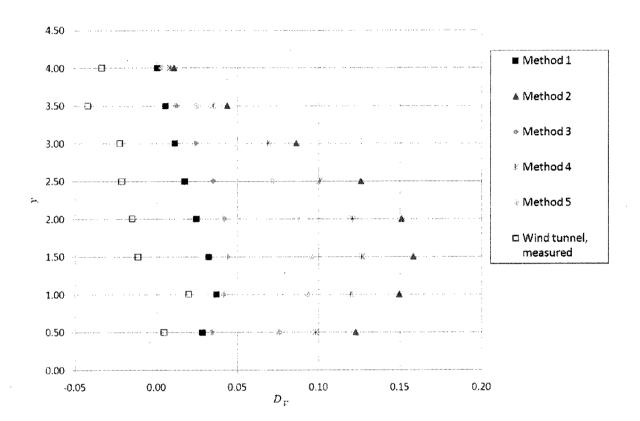


Figure G.6 – Predicted and measured D_V profiles for test 7, $S_Z = 2.0$ h

In Figure G.7, it is observed that both D_V profiles measured in the wind tunnel exceeded predictions for the SLO (method 2). At heights over y = 1.5 h, the profiles are much closer to method 2 predictions, but still slightly greater. This is an atypical result; however, it illustrates how flow in the wake of an obstacle group can be the complex, and difficult to predict.

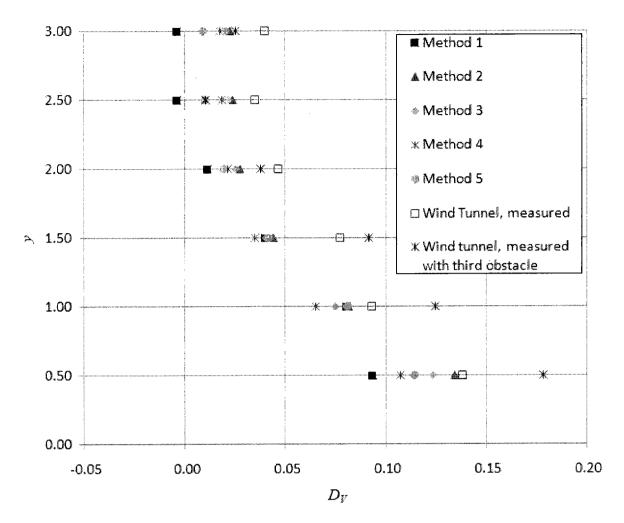


Figure G.7 – Predicted and measured D_V profiles for test 6, $a = 0^{\circ}$

It is evident in the results that it can be difficult to predict R_V in the wake of an obstacle cluster. Trends are not always readily apparent, and when discovered, seem to always have exceptions. Findings are summarized below, based mainly on this study and Musselman's.

- Near the obstacle group, superposition (method 1) appears to provide reasonably good estimates of R_V in the wake.
- Far from the obstacle group, superposition underestimates the velocity deficit. R_V predictions made for a SLO and corrected based on Musselman's model typically result in the best predictions.

- For closely spaced obstacles, the SLO method appears to work best. Spacing is a greater factor than downwind distance in determining which approach to use.
- iv) For very large spacings, superposition is typically most suitable.
- v) Smaller obstacles can have a significant effect on the wake at lower heights, but it may be safe to neglect them at greater heights.

The exact meanings of near, far, closely spaced, and large spacings depend on details of the obstacle group, and merit further study. As a rough estimate, based on results for clusters 1 and 2, and Musselman's results for a row of cubes, near means roughly less than 10 h downwind, and closely spaced means less than about 1.5 h.